

CENTRO BRASILEIRO DE PESQUISAS FÍSICAS

MASTER'S THESIS

---

***CP*-asymmetry measurements in  
charmless three-body  $B^\pm$  decays in the  
LHCb experiment**

---

*Author:*  
Gabriel GOMES  
da Silva

*Supervisor:*  
Dr. Ignacio Alfonso de  
BEDIAGA e Hickman

*A thesis submitted in fulfilment of the requirements  
for the degree of Master of Science  
in the Brazilian Centre For Physics Research (CBPF)*



Rio de Janeiro  
September, 2020



*“And this two-pronged investigation into the nature of the world and the nature of our selves is, to a very major degree, I believe, what the human enterprise is about.”*

Carl Edward Sagan [1]



CENTRO BRASILEIRO DE PESQUISAS FÍSICAS

## *Abstract*

Coordenação de Física de Altas Energias (COHEP)

Master of Science

***CP*-asymmetry measurements in  
charmless three-body  $B^\pm$  decays in the LHCb experiment**

by Gabriel GOMES  
da Silva

In this thesis, new results and studies are presented on the charge asymmetry of  $B$ -meson decays, which constitute a rich laboratory to investigate  $CP$ -violation mechanisms. The work focused on charmless three-body  $B^\pm$  decays:  $B^\pm \rightarrow K^\pm \pi^+ \pi^-$ ,  $B^\pm \rightarrow K^\pm K^+ K^-$ ,  $B^\pm \rightarrow \pi^\pm \pi^+ \pi^-$  and  $B^\pm \rightarrow \pi^\pm K^+ K^-$ . The LHCb experiment provided a data set corresponding to an integrated luminosity of  $5.9 \text{ fb}^{-1}$  acquired during Run 2 (2015-2018) of LHC when proton-proton collisions were produced at a centre-of-mass energy of 13 TeV. The  $B^\pm \rightarrow h^\pm h^+ h^-$  data samples were subjected to two analyses.

First, a simultaneous fit to  $B^+$  and  $B^-$  invariant-mass distributions was performed in each decay channel in order to determine the number of  $B$  candidates and the raw charge asymmetry. The inclusive  $CP$  asymmetry was finally obtained by correcting the raw asymmetry from acceptance effects and experimentally-introduced asymmetries. In a second analysis, a simple, model-independent method was employed to extract  $CP$  asymmetries from  $B \rightarrow PV$  decays, meaning processes resulting in a pseudoscalar and a vector resonance, without the expense of standard approaches such as amplitude analyses. The method proved to be satisfactory and reliable.

**Keywords:**  $CP$  asymmetry, charmless three-body  $B^\pm$  decays, vector meson, LHCb



## Resumo

Nesta dissertação, novos resultados e estudos são apresentados sobre a assimetria de carga de decaimentos envolvendo o méson  $B$ , que constituem um rico laboratório para a investigação de mecanismos de violação  $CP$ . O trabalho se concentrou em decaimentos sem charme de  $B^\pm$  em três corpos:  $B^\pm \rightarrow K^\pm \pi^+ \pi^-$ ,  $B^\pm \rightarrow K^\pm K^+ K^-$ ,  $B^\pm \rightarrow \pi^\pm \pi^+ \pi^-$  e  $B^\pm \rightarrow \pi^\pm K^+ K^-$ . A fábrica de mésons  $B$  responsável pelos dados utilizados foi o experimento LHCb, que forneceu um conjunto de dados correspondendo a uma luminosidade integrada de  $5.9 \text{ fb}^{-1}$  adquirida durante o Run 2 (2015-2018) do LHC, quando colisões próton-próton foram produzidas com uma energia de centro de massa de 13 TeV. As amostras de dado de  $B^\pm \rightarrow h^\pm h^+ h^-$  foram submetidas a duas análises.

Primeiro, um ajuste simultâneo às distribuições de massa invariante de  $B^+$  e  $B^-$  foi executado em cada canal de decaimento com o objetivo de determinar o número de mésons  $B$  candidatos e a assimetria de carga bruta. A assimetria  $CP$  inclusiva foi finalmente obtida corrigindo a assimetria bruta de efeitos de eficiência do sinal e de assimetrias experimentalmente introduzidas. Segundo, um método simples, independente de modelo, foi empregado para extrair assimetrias  $CP$  de decaimentos  $B \rightarrow PV$  sem o custo de abordagens padrão como análises de amplitude. O método se provou satisfatório e confiável.

**Palavras-chave:** assimetria  $CP$ , decaimentos sem charme de  $B^\pm$  em três corpos, méson vetorial, LHCb



## *Acknowledgements*

The research work presented in this thesis would not have been conceived without the assistance and support of several people. I want to acknowledge and express my deepest gratitude:

To my supervisor, Professor Ignácio Bediaga, who encouraged me to work hard and whose expertise continually serves as inspiration.

To Professors Jussara Miranda and Alberto Reis, for the availability, patience and generosity in sharing their experience.

To Professor André Massafferri, for welcoming me to the work group in my CBPF early days.

To my fellow student Laís Lavra, whose guidance and reassurance were fundamental since the start of my work.

To my colleague Diego Torres, a confidant, for the constant cooperation.

To Patrícia Magalhães, for gladly offering me help and coming to rescue.

To the remainder of the work group, Professors Fernando, Melissa, Juan, Álvaro, Irina and Helder, for the instructive scientific collaboration.

To the CBPF staff, who accomplished to create such a delightful workplace.

To my friends, for the never-ending incentive. Especially, to Raineri Ramalho, for cheering me on and assisting in the writing process.

To Márcia Ribeiro, who helped me evolve a healthier psyche and be more effortless.

To my mother, Lourdes, inexhaustible source of devotion, support and joie de vivre.

Finally, to CAPES, for their financial support.



# Contents

<b>Abstract</b>	<b>v</b>
<b>Resumo</b>	<b>vii</b>
<b>Acknowledgements</b>	<b>ix</b>
<b>List of Figures</b>	<b>xiii</b>
<b>List of Tables</b>	<b>xv</b>
<b>List of Abbreviations</b>	<b>xvii</b>
<b>Introduction</b>	<b>1</b>
<b>1 Theoretical and Experimental Overview</b>	<b>5</b>
1.1 The Standard Model . . . . .	5
1.1.1 <i>CPT</i> Symmetries . . . . .	7
1.1.2 The CKM Matrix . . . . .	7
1.2 Three-Body Kinematics . . . . .	9
1.3 <i>CP</i> Violation in $B^\pm$ Decays . . . . .	13
1.3.1 Direct <i>CP</i> Violation . . . . .	13
1.3.2 <i>CPT</i> Constraint . . . . .	15
1.3.3 Theoretical and Experimental Approaches . . . . .	15
1.4 Charmless Three-Body $B^\pm$ Decays . . . . .	17
<b>2 The LHCb Experiment</b>	<b>21</b>
2.1 The Large Hadron Collider . . . . .	21
2.2 The LHCb Detector . . . . .	24
2.3 Tracking . . . . .	25
2.3.1 Vertex Locator . . . . .	26
2.3.2 Trackers . . . . .	27
2.3.3 Magnet . . . . .	29
2.4 Particle Identification . . . . .	30
2.4.1 Ring Imaging Cherenkov Detectors . . . . .	30
2.4.2 Calorimeters . . . . .	31
2.4.3 Muon System . . . . .	33
2.5 Trigger . . . . .	34
<b>3 <math>B^\pm</math> Candidate Selection</b>	<b>37</b>
3.1 Introduction . . . . .	37
3.1.1 Selection Variables . . . . .	37
3.1.2 Selection Stages . . . . .	39
3.2 Data and Simulation . . . . .	39
3.3 Background Sources . . . . .	40

3.3.1	Combinatorial background	41
3.3.2	Peaking background	41
3.3.3	Partially-reconstructed background	42
3.4	Pre-Selection	44
3.4.1	Trigger Selection	44
3.4.2	Stripping Requirements	45
3.4.3	Loose PID Requirements	46
3.5	Final Selection	46
3.5.1	Multivariate Analysis Selection	46
3.5.2	Final PID Selection	48
3.5.3	Mass Vetoes	49
3.6	Summary	49
<b>4</b>	<b><i>CP</i>-asymmetry measurements in <math>B^\pm \rightarrow h^\pm h^+ h^-</math> decays</b>	<b>51</b>
4.1	Measurement Strategy	51
4.2	$B^\pm$ Candidate Invariant-Mass Fit	53
4.2.1	Background Studies	53
4.2.2	Fit Model	53
4.2.3	Fit Results	58
4.3	Phase-Space Acceptance	60
4.3.1	Acceptance Correction	61
4.3.2	PID Efficiency	62
4.3.3	Detection-Asymmetry Correction	62
4.3.4	Combining Acceptance Maps	63
4.3.5	Average Efficiency	65
4.4	Results and Prospects	65
<b>5</b>	<b><i>CP</i>-asymmetry measurements in <math>B \rightarrow PV</math> decays</b>	<b>67</b>
5.1	Introduction	67
5.2	The Model-Independent Method	68
5.2.1	Case Studies	69
5.2.2	Method Viability	71
5.3	Results	73
5.3.1	$B^\pm \rightarrow \pi^\pm \pi^+ \pi^-$ decay	73
5.3.2	$B^\pm \rightarrow K^\pm \pi^+ \pi^-$ decay	76
	$\rho(770)^0$ sector	76
	$K^*(892)^0$ sector	78
5.3.3	$B^\pm \rightarrow \pi^\pm K^+ K^-$ decay	80
5.3.4	$B^\pm \rightarrow K^\pm K^+ K^-$ decay	82
5.4	Summary and Considerations	83
	<b>Conclusion</b>	<b>85</b>
	<b>A Invariant-Mass Fit</b>	<b>87</b>
	A.1 Signal Fit-Model Study	87
	A.2 Complementary Mass-Fit Results	92
	<b>B Complementary <math>B \rightarrow PV</math> Plots</b>	<b>99</b>
	<b>Bibliography</b>	<b>105</b>

# List of Figures

1.1	Diagram of the elementary particles of the Standard Model and their physical properties . . . . .	6
1.3	Dalitz plot kinematic boundaries. . . . .	11
1.4	Illustration of a resonant and a non-resonant three-body decays. . . . .	12
1.5	Illustration of the $B_s^0 \rightarrow \bar{D}^0 K^- \pi^+$ decay Dalitz plot. . . . .	12
1.6	Tree and Penguin diagrams. . . . .	18
1.7	$CP$ -asymmetry distributions with the Miranda technique for $B^\pm \rightarrow h^\pm h^+ h^-$ decays. . . . .	19
2.1	CERN accelerator complex and experiments. . . . .	22
2.2	Recorded integrated luminosities in the LHCb for each year of operation. . . . .	23
2.3	Schematic side view of the LHCb detector. . . . .	24
2.4	Pseudorapidity distribution of $b\bar{b}$ pairs produced in simulated $pp$ collisions. . . . .	25
2.5	Arrangement of VELO modules along the beamline. . . . .	26
2.6	Layout of the TT. . . . .	27
2.7	Layout of an $x$ detection layer in the second IT station. . . . .	28
2.8	OT module cross section and arrangement in layers and stations . . . . .	28
2.9	Arrangement and scale of the tracking stations. . . . .	29
2.10	Schematic view of the dipole magnet. . . . .	29
2.11	Reconstructed Cherenkov angle for isolated tracks, as a function of track momentum in the RICH 1 $C_4F_{10}$ radiator. . . . .	30
2.12	Schematic layouts of RICH 1 and RICH 2 detectors. . . . .	31
2.13	Lateral segmentation of the SPD/PS, ECAL and HCAL. . . . .	32
2.14	Side view of the muon system and front view of a quadrant of a muon station. . . . .	33
2.15	Overview of the LHCb trigger in Run 1 and Run 2. . . . .	34
3.1	Schematic view of the topology of a three-body decay. . . . .	37
3.2	Simulated distributions of cross-feed background for each $B^\pm \rightarrow h^\pm h^+ h^-$ channel. . . . .	41
3.3	The figure of merit and the signal efficiency for the self BDT optimisations. . . . .	48
4.1	Fitted invariant-mass distributions of $B^\pm \rightarrow K^\pm \pi^+ \pi^-$ separated by charge. . . . .	58
4.2	Fitted invariant-mass distributions of $B^\pm \rightarrow K^\pm K^+ K^-$ separated by charge. . . . .	59
4.3	Fitted invariant-mass distributions of $B^\pm \rightarrow \pi^\pm \pi^+ \pi^-$ separated by charge. . . . .	59
4.4	Fitted invariant-mass distributions of $B^\pm \rightarrow \pi^\pm K^+ K^-$ separated by charge. . . . .	60

4.5	Simulated data projections in the standard Dalitz plot and Square Dalitz plot. . . . .	61
4.6	Flux diagram presenting all the stages needed for the acceptance construction by each charge and channel. . . . .	63
4.7	Overall acceptance maps for $B^+ \rightarrow h^+h^+h^-$ decays. . . . .	64
4.8	Overall acceptance maps for $B^- \rightarrow h^-h^+h^-$ decays. . . . .	64
5.1	Method viability studies by $\mathcal{A}_{\text{CP}}^{\rho(770)^0}$ measurements. . . . .	72
5.2	Yield distributions over $m(\pi^+\pi^-)_{\text{low}}$ for $\rho(770)^0$ in $B^\pm \rightarrow \pi^\pm\pi^+\pi^-$ . . . . .	74
5.3	Measurement plots for $\rho(770)^0$ in $B^\pm \rightarrow \pi^\pm\pi^+\pi^-$ . . . . .	75
5.4	Yield distributions over $m(\pi^+\pi^-)$ for $\rho(770)^0$ in $B^\pm \rightarrow K^\pm\pi^+\pi^-$ . . . . .	76
5.5	Measurement plots for $\rho(770)^0$ in $B^\pm \rightarrow K^\pm\pi^+\pi^-$ . . . . .	77
5.6	Yield distributions over $m(K^\pm\pi^\mp)$ for $K^*(892)^0$ in $B^\pm \rightarrow K^\pm\pi^+\pi^-$ . . . . .	78
5.7	Plots for $K^*(892)^0$ in $B^\pm \rightarrow K^\pm\pi^+\pi^-$ . . . . .	79
5.8	Yield distributions over $m(K^\pm\pi^\mp)$ for $K^*(892)^0$ in $B^\pm \rightarrow \pi^\pm K^+K^-$ . . . . .	80
5.9	Measurements plots for $K^*(892)^0$ in $B^\pm \rightarrow \pi^\pm K^+K^-$ . . . . .	81
5.10	Yield distributions over $m(K^+K^-)_{\text{low}}$ for $\phi(1020)$ in $B^\pm \rightarrow K^\pm K^+K^-$ . . . . .	82
5.11	Measurement plots for $\phi(1020)$ in $B^\pm \rightarrow K^\pm K^+K^-$ . . . . .	83
A.1	$B^\pm \rightarrow K^\pm\pi^+\pi^-$ comparison invariant-mass fit plots between signal fit models. . . . .	88
A.2	$B^\pm \rightarrow K^\pm K^+K^-$ comparison invariant-mass fit plots between signal fit models. . . . .	89
A.3	$B^\pm \rightarrow \pi^\pm\pi^+\pi^-$ comparison invariant-mass fit plots between signal fit models. . . . .	90
A.4	$B^\pm \rightarrow \pi^\pm K^+K^-$ comparison invariant-mass fit plots between signal fit models. . . . .	91
A.5	Complementary invariant-mass fit plots for $B^\pm \rightarrow K^\pm\pi^+\pi^-$ . . . . .	95
A.6	Complementary invariant-mass fit plots for $B^\pm \rightarrow \pi^\pm\pi^+\pi^-$ . . . . .	96
A.7	Complementary invariant-mass fit plots for $B^\pm \rightarrow \pi^\pm\pi^+\pi^-$ . . . . .	97
A.8	Complementary invariant-mass fit plots for $B^\pm \rightarrow \pi^\pm\pi^+\pi^-$ . . . . .	98
B.1	Complementary plots for $\rho(770)^0$ in $B^\pm \rightarrow \pi^\pm\pi^+\pi^-$ . . . . .	100
B.2	Complementary plots for $\rho(770)^0$ in $B^\pm \rightarrow K^\pm\pi^+\pi^-$ . . . . .	101
B.3	Complementary plots for $K^*(892)^0$ in $B^\pm \rightarrow K^\pm\pi^+\pi^-$ . . . . .	102
B.4	Complementary plots for $K^*(892)^0$ in $B^\pm \rightarrow \pi^\pm K^+K^-$ . . . . .	103
B.5	Complementary plots for $\phi(1020)$ in $B^\pm \rightarrow K^\pm K^+K^-$ . . . . .	104

# List of Tables

1.1	Summary of relevant pseudoscalar mesons for this work and their physical properties. . . . .	9
1.2	Branching fractions for the $B^\pm \rightarrow h^\pm h^+ h^-$ decay channels. . . . .	18
3.1	Signal statistics for the small MC samples. . . . .	40
3.2	Partially-reconstructed background contributions to the $B^\pm \rightarrow K^\pm \pi^+ \pi^-$ decay. . . . .	43
3.3	Partially-reconstructed background contributions to the $B^\pm \rightarrow K^\pm K^+ K^-$ decay. . . . .	43
3.4	Partially-reconstructed background contributions to the $B^\pm \rightarrow \pi^\pm \pi^+ \pi^-$ decay. . . . .	43
3.5	Partially-reconstructed background contributions to the $B^\pm \rightarrow \pi^\pm K^+ K^-$ decay. . . . .	44
3.6	Inclusive stripping line selection criteria for charmless $B^\pm \rightarrow h^\pm h^+ h^-$ decays. . . . .	45
3.7	Cuts on the BDT output variable calculated by the specific optimisation (self) training for each $B^\pm \rightarrow h^\pm h^+ h^-$ channel. . . . .	47
3.8	PID selection criteria for $B^\pm \rightarrow h^\pm h^+ h^-$ decays. . . . .	49
4.1	Fractions obtained from MC studies of the relevant background modes for each of the $B^\pm \rightarrow h^\pm h^+ h^-$ decays. . . . .	54
4.2	$B^\pm$ signal yield and raw asymmetry of the four charmless three-body decays $B^\pm \rightarrow h^\pm h^+ h^-$ for the combined Run 2 data set. . . . .	60
4.3	Average efficiency for $B^+$ and $B^-$ and the $R$ ratio for the binned acceptance for $B^\pm \rightarrow h^\pm h^+ h^-$ decay channels with 2015-2016 data. . . . .	65
5.1	Summary of relevant neutral vector resonances and their physical properties. . . . .	67
5.2	Summary of relevant neutral vector resonances and their main decay channels. . . . .	68
5.3	Branching fractions of the relevant vector resonant states . . . . .	68
5.4	Quadratic fit parameters over $B^+$ and $B^-$ yield distributions for $\rho(770)^0$ in $B^\pm \rightarrow \pi^\pm \pi^+ \pi^-$ . . . . .	74
5.5	Quadratic fit parameters of $\rho(770)^0$ in $B^\pm \rightarrow K^\pm \pi^+ \pi^-$ for $B^+$ and $B^-$ yield distributions. . . . .	76
5.6	Quadratic fit parameters over $B^+$ and $B^-$ yield distributions for $K^*(892)^0$ in $B^\pm \rightarrow K^\pm \pi^+ \pi^-$ . . . . .	78
5.7	Quadratic fit parameters over $B^+$ and $B^-$ yield distributions for $K^*(892)^0$ in $B^\pm \rightarrow \pi^\pm K^+ K^-$ . . . . .	80
5.8	Quadratic fit parameters over $B^+$ and $B^-$ yield distributions for $\phi(1020)$ in $B^\pm \rightarrow K^\pm K^+ K^-$ . . . . .	82
5.9	Summary of $CP$ -asymmetry measurements for the vector resonance channels and their associated final-state $B^\pm \rightarrow h^\pm h^+ h^-$ decays. . . . .	84

5.10 Selected event statistics for the quadratic fit histograms. . . . .	84
A.1 Parameters extracted from the invariant-mass fit distributions of data samples. The numbers tagged by a '(C)' were fixed in the corresponding fit. . . . .	92
A.2 Correspondent reflection component to each channel as presented in Table A.1. . . . .	94

# List of Abbreviations

<b>ALICE</b>	<b>A</b> Large Ion Collider Experiment
<b>ATLAS</b>	<b>A</b> Large Toroidal LHC Apparatu <b>S</b>
<b>BF</b>	<b>B</b> ranching <b>F</b> raction
<b>CERN</b>	<b>E</b> uropean <b>O</b> rganization for Nuclear Research
<b>CMS</b>	<b>C</b> ompact <b>M</b> uon <b>S</b> olenoid
<i>CP</i>	<b>C</b> harge and <b>P</b> arity
<i>CPT</i>	<b>C</b> harge, <b>P</b> arity and <b>T</b> ime
<b>DP</b>	<b>D</b> alitz <b>P</b> lot
<b>ECAL</b>	<b>E</b> lectromagnetic <b>C</b> ALorimeter
<b>FSI</b>	<b>F</b> inal <b>S</b> tate <b>I</b> nteractions
<b>HCAL</b>	<b>H</b> adronic <b>C</b> ALorimeter
<b>HLT</b>	<b>H</b> igh <b>L</b> evel <b>T</b> rigger
<b>IT</b>	<b>I</b> nnner <b>T</b> racker
<b>L0</b>	<b>L</b> evel- <b>0</b>
<b>LHC</b>	<b>L</b> arge <b>H</b> adron <b>C</b> ollider
<b>LHCb</b>	<b>L</b> arge <b>H</b> adron <b>C</b> ollider <b>b</b> eauty
<b>OT</b>	<b>O</b> uter <b>T</b> racker
<b>PID</b>	<b>P</b> article <b>I</b> Dentification
<i>pp</i>	<b>p</b> roton- <b>p</b> roton
<b>PS</b>	<b>P</b> re <b>S</b> hower
<b>RICH</b>	<b>R</b> ing <b>I</b> maging <b>C</b> Herenkov
<b>SDP</b>	<b>S</b> quare <b>D</b> alitz <b>P</b> lot
<b>SM</b>	<b>S</b> tandard <b>M</b> odel
<b>SPD</b>	<b>S</b> cintillator <b>P</b> ad <b>D</b> etector
<b>ST</b>	<b>S</b> ilicon <b>T</b> racker
<b>TT</b>	<b>T</b> racker <b>T</b> uricensis
<b>VELO</b>	<b>V</b> ertex <b>L</b> Ocator



*To my mother.  
All she possessed, she freely gave.*

# Introduction

The origin of the endeavour of particle physics can be traced back to the early tradition of philosophical atomism. The term atomism is derived from the Greek word *atoma* — “things that cannot be cut or divided” — and refers to any doctrine that explains complex phenomena in terms of aggregates of fixed particles or units. This philosophy has found its most successful application as a metaphysical thesis in natural science: according to the atomistic view, the material universe is composed of atoms, minute particles considered to be relatively simple and immutable and too small to be visible; along with the void in which atoms move [2]. The multiplicity of visible forms in nature, then, would be based upon differences in these particles and in their configurations; consequently, any observable changes in the universe must be reduced to changes in atomic configurations.

Not only the general idea of atomism but also the whole spectrum of its different forms originated in ancient Greece. As early as the 5th century BCE, atomism was found in its strict sense in the ideas of Leucippus and his student Democritus: the atoms are absolutely indivisible, qualitatively identical (*i.e.*, distinct only in shape, size, and motion), and combinable with each other only by juxtaposition. Other qualitative forms of atomism are found in the hypotheses of Empedocles, based on the doctrine of the four elements, and that of Anaxagoras, with as many qualitatively different atoms as there are different substances. Yet, in spite of its successful start, atomism did not gain predominance in Greek thought. This is mainly because Plato and Aristotle were not satisfied with atomism as a general solution for the problems of change.

The ideas of atomism would resurface throughout history, but it was only in the nineteenth century that they became fruitful in science with the emergence of atomic chemistry and the kinetic theory of gases. The work of experimentalists Robert Boyle and Antoine Lavoisier, two of the main founders of modern chemistry, allowed John Dalton to hold that there are as many different kinds of elementary atoms as there are chemical elements. By the end of the century, the fact that the properties of chemical compounds are due to an atomic structure that can be represented by a structural formula was undisputed, as well as the kinetic theory of gases was met with impressive empirical success from the mid 1800s onwards. However, there was the emergence and success of phenomenological thermodynamics, which made it possible to deal with a range of thermal and chemical phenomena without resorting to an underlying structure of matter. Consequently, atomism was rejected by leading scientists and philosophers up to the end of the nineteenth century and beyond [3].

Further scientific findings on the structure of matter would disagree with Dalton's notions of chemical atoms at the turn of the century, therefore atomic models were forced to evolve. Atoms were no longer considered indivisible: J. J. Thomson's discovery of the electron [4] revealed the existence of particles with masses much smaller than the lightest atom, and Rutherford's scattering experiment [5] proved the atom had substructure, namely, a nucleus. Atoms were also disproved to be immutable as molecules were no longer seen as a mere juxtaposition of atoms: when entering into a compound, atoms became ions. Finally, any remaining opposition

from the scientific community against an atomic theory was ultimately dismissed by Einstein's theoretical work on Brownian motion [6], together with Jean Perrin's subsequent experimental findings on the topic [7].

The enormous development of particle physics as a field of research that took place in the 20th century is unquestionably coupled with the rapid technological developments. Most notably, the increase in the energies accessible by particle accelerators would immediately be followed by the discovery of new particles. The accomplishments garnered in this period were abundant and radical: the detection of the positron [8], the antiparticle of the electron; the discovery of the neutron [9], a neutral constituent of the nucleus alongside the positive proton; the theoretical proposition [10,11] and ensuing experimental evidence [12,13] in favour of the quark model; in addition to the detection of a multitude of short-lived particles.

Until its development in the third decade of the 20th century, the scientific atomic theory did not differ philosophically very much from that of Dalton, although at first sight the difference may appear large. Early twentieth-century atomism, in a sense, represents the achievement of the ancient Greek ideal insofar as it is a theory of the properties of matter in terms of more elementary subatomic particles, electrons, protons and neutrons, characterised in terms of a few basic properties. The major difference is that the nature of the particles and the laws governing them were arrived at empirically, rather than by *a priori* philosophical argument. In contemporary atomic theory nonetheless, the differences from Dalton are much more fundamental. The hypothesis of the existence of immutable elementary particles has been abandoned: elementary particles can be transformed into radiation and vice versa; and the particles do not even necessarily preserve their identity.

The current, best theory that describes the behaviour of electrons, quarks, and the other fundamental particles of the Universe is referred to as the Standard Model (SM) of particle physics. The SM is the culmination of almost a century of theoretical and experimental development and has shown itself to be both fantastically predictive and accurate throughout the years. This is best exemplified by achievements such as the SM prediction for the electron anomalous magnetic moment, which matches experiment to ten significant figures [14,15], and the discoveries of many particles that were first predicted by the SM, such as the discovery of the Higgs boson by the ATLAS [16] and CMS experiments [17] at LHC in 2012.

The field of high-energy physics, however, aims to tackle the unsolved questions of the SM, either by directly searching for particles that are not predicted by the SM or by high-precision measurements looking for deviations from SM predictions. For instance, a description of gravity is not included in the Standard Model: it is still an open problem to seamlessly combine a quantum theory like the SM to the current theory of gravity, Einstein's General Relativity. The exclusion of gravity in the SM framework is not its only shortcoming as this becomes evident when the theory clashes with cosmological evidence. A number of astronomical observations in the last hundred years have led to the hypothesis that the particles described by the Standard Model constitute but a small fraction of the total mass content of the Universe. The current estimate for the fraction of the total mass that is composed of 'ordinary matter' is  $\sim 16\%$  [18]; the remaining mass is in the form of 'dark matter', of which very little is known.

Another gap in the model is the natural assumption from the standard cosmological model, known as the  $\Lambda$ CDM (Lambda Cold Dark Matter) model, that matter and antimatter should have been produced in equal amounts at the Big Bang. In such Universe, there would be nothing except for 'light', since interacting matter and antimatter annihilate into radiation. Evidently, the present-day cosmos is

matter-dominated, which raises the question of what processes in the early Universe privileged one kind of matter over the other. However, this imbalance manifests due to a tiniest preference, from nature, to matter: it is estimated that for each 10 billion particles of antimatter generated in the Big Bang, 10 billion plus 1 matter particles were simultaneously produced. This matter surplus survived, *i.e.*, did not become light, and originated mostly everything we know: galaxies, stars, planets, living beings, *etc.* Ultimately, one might claim that the Universe as we know it exists because of a natural ‘imperfection’.

The precise mechanism that creates this asymmetry, known as baryogenesis, is still unknown. However, three requirements, the ‘Sakharov conditions’, are known to be necessary in any theory of baryogenesis [19]:

- (i) particle interactions that violate baryon number must exist;
- (ii) interactions that violate  $CP$  symmetry, *i.e.*, the symmetry between particles and antiparticles, must exist;
- (iii) these interactions must have occurred at a time when the Universe was out of thermal equilibrium;

The Standard Model can technically satisfy these three conditions, although for (ii) at an order of magnitude lower than what is necessary to elucidate the observed matter-antimatter asymmetry [20]. This discrepancy implies that additional sources of  $CP$  violation must exist that are not accounted for in the SM, and any disagreement between reliable predictions of  $CP$  violation in the SM and experimental results may reveal new physics.

The study of known  $CP$ -violating processes and searches for new sources of  $CP$  violation are a significant part of the physics programme of the LHCb experiment. The decay channels studied in this thesis have already shown themselves as a rich laboratory for  $CP$ -violating effects [21–23]. Thus, the  $CP$ -asymmetry measurements presented in this work represent an additional step towards a better understanding of these decay channels. First, phase-space integrated  $CP$ -asymmetry measurements to charmless three-body  $B$  decays, which include  $B^\pm \rightarrow K^\pm \pi^+ \pi^-$ ,  $B^\pm \rightarrow K^\pm K^+ K^-$ ,  $B^\pm \rightarrow \pi^\pm \pi^+ \pi^-$  and  $B^\pm \rightarrow \pi^\pm K^+ K^-$ , were performed and served as an update to the ones presented in Ref. [21]. Second, a complementary set of measurements was carried out over  $B$  decays involving neutral vector resonances.

This thesis is organised as follows. Chapter 1 provides an overview of the Standard Model and the mechanisms through which  $CP$  violation occurs. The theoretical motivation for the measurement and existing predictions are also discussed. In Chapter 2, a description of the LHCb detector and its operating components is given. The strategies employed to identify signal candidates against different background sources are detailed in Chapter 3. The fitting strategy used to determine the yields of the four signal channels and their subsequent  $CP$ -asymmetry measurements is presented in Chapter 4. Finally, Chapter 5 introduces an alternative, model-independent method to perform  $CP$ -asymmetry measurements of vector meson decays. The results obtained and their relation to existing measurements are also examined.

The work presented in this thesis is currently under review within the LHCb collaboration.



## Chapter 1

# Theoretical and Experimental Overview

This chapter covers relevant theoretical background and motivation for the work presented in this thesis. The framework of the Standard Model is described first, in Section 1.1, followed by a summary of the distinct properties of decays involving three final-state particles in Section 1.2. A short outline of the manifestations of  $CP$  violation in  $B^\pm$  decays is given in Section 1.3. Finally, an overview of the decays explored in this thesis is presented in Section 1.4. A bulk of the information presented is derived from Ref. [24]; other sources are indicated throughout.

### 1.1 The Standard Model

The Standard Model (SM) of particle physics is a relativistic quantum field theory that respects the symmetries of the gauge group  $SU(3)_C \otimes SU(2)_W \otimes U(1)_Y$ , where the subscripts denote the associated charges conserved by each group:  $C$  standing for colour,  $W$  for weak isospin, and  $Y$  for weak hypercharge. The result is a theory that describes the interactions of matter under the strong, weak, and electromagnetic forces. Both nuclear forces are mostly inaccessible in our daily lives, however, the strong force plays an important role in matter stability, whereas the weak force is responsible for radioactive decays. Gravity, the remaining fundamental force, is still unformulated as a quantum theory and therefore persists outside the framework of the SM.

While the fundamental objects in the theory are the quantum fields themselves, their properties are uncovered through the study of their excitations, *i.e.*, the particles associated with each of them. There are currently twelve different particles in the SM identified to constituting the matter in the Universe; another four, the gauge bosons, *i.e.*, which follow the Bose-Einstein statistics, serve as mediators of the three contemplated fundamental forces. A final particle, the Higgs boson, is associated with the mechanism responsible for generating particles' masses. The SM particles are displayed in Figure 1.1 alongside their mass, electric charge, and spin.

The twelve matter particles are spin- $\frac{1}{2}$  fermions, *i.e.*, which obey the Fermi-Dirac statistics, and can be partitioned into six quarks, which feel the strong force, and six leptons, which do not. The leptons can be further divided into charged leptons and neutrinos; the latter only interact via the weak force. The columns in Figure 1.1 also present another possible categorisation of fermions, into generations. In reality, all the stable matter in the Universe is built up of first-generation fermions only, with their heavier counterparts in other generations holding identical quantum numbers. Finally, there exists an associated antimatter partner to each fermion with same mass and lifetime, but opposite quantum numbers.

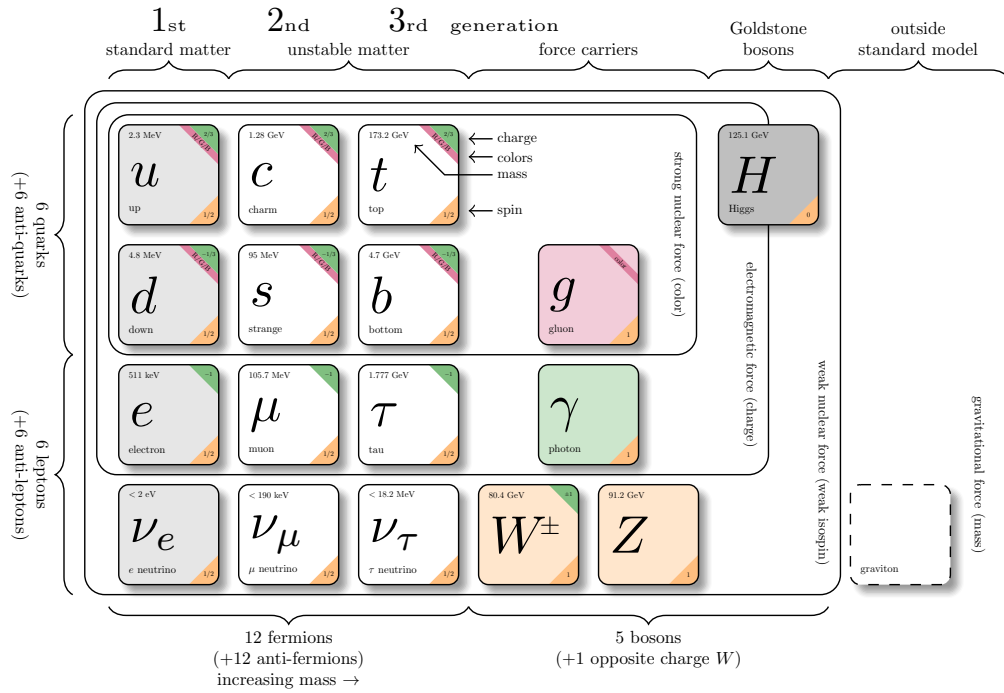


FIGURE 1.1: Diagram of the elementary particles of the Standard Model and their physical properties [25].

The six quarks experience the strong nuclear force because they carry the colour charge, of which three states – *red*, *blue*, *green* – exist. The symmetry in the SM associated with the strong force is  $SU(3)_C$  and the theory that models its interactions is called Quantum Chromodynamics (QCD). In the QCD framework, strong interactions are mediated by gluons, which are spin-1 massless bosons that also carry colour charge themselves. The gluon self-interaction leads to a peculiar feature of the strong interaction: the strength of the force is low at short distances but high at long distances. This means, for instance, that the potential increases as two quarks are being separated, and it rapidly becomes more favourable to form a new pair of quarks. It results in ‘colour confinement’ – neither quarks nor gluons can propagate individually but only within bound states, called hadrons, which must have zero colour charge. Predominantly, this is achieved in one of two different ways: mesons are quark-antiquark ( $q\bar{q}$ ) states and baryons are three-quark ( $qqq$ ) states; exotic states with four or five quarks/antiquarks are possible and have been observed [26, 27].

In the SM, the electromagnetic and weak forces are unified into a common ‘electroweak’ (EW) framework [28–30], the Glashow-Weinberg-Salam (GWS) theory, associated with the symmetry  $SU(2)_W \otimes U(1)_Y$ . The electromagnetic force is mediated by the massless photon ( $\gamma$ ), while the weak force is mediated by three massive spin-1 bosons ( $W^\pm$  and  $Z$ ). The evidence that in nature the three weak bosons are observed as having mass, or equivalently, that the weak force is short-range, is *a priori* a dilemma for any gauge theory describing the weak interaction, since the inclusion of any boson mass terms is forbidden by gauge symmetry. An elegant mechanism to solve this conundrum was published almost simultaneously by Brout and Englert [31], Higgs [32], and Guralnik, Hagen, and Kibble [33], in which all particles are massless at high energies, and below the electroweak scale their masses are

dynamically generated by the spontaneous breaking of the electroweak symmetry  $SU(2)_W \otimes U(1)_Y$ .

### 1.1.1 CPT Symmetries

In the physics framework, a system's symmetries represent transformations that leave it invariant. Also, continuous symmetries play a significant role as they are associated with conservation laws according to Noether's theorem [34].

Beyond its gauge symmetries, the SM can also display three discrete symmetries: parity inversion ( $P$ ), charge conjugation ( $C$ ), and time reversal ( $T$ ). These three can be associated together, being  $CP$  and  $CPT$  the most relevant combinations. The SM must stay invariant under the  $CPT$  combination, as this can be shown to be equivalent with Lorentz invariance for a relativistic quantum field theory. Previously, all three discrete symmetries were assumed to be individually conserved, however both  $P$  and  $C$  were found to be maximally violated in weak interactions.

The parity operator inverts the sign of all three spatial coordinates, *i.e.*, vector  $\mathbf{a}$  becomes  $P(\mathbf{a}) = -\mathbf{a}$ . Parity is a good symmetry of both electromagnetic and strong interactions. However, it was first predicted by Lee and Yang [35] that it could be violated in weak interactions as a solution for the  $\tau$ - $\theta$  puzzle. Indeed, it was later demonstrated by Wu [36], using the beta decay of cobalt-60, that parity was (maximally) violated by the weak interaction. The charge conjugation operation flips the sign of all quantum numbers of a particle, that is, it converts a particle into its antiparticle. It can be seen to be violated by the weak force by noting that the application of  $C$  to left-handed neutrinos results in left-handed antineutrinos, which are still to be seen experimentally and are not described in the SM. Time reversal corresponds to the inversion of the time coordinate.

It was then expected that at least the  $CP$  combination would instead be a good symmetry for weak interactions – *e.g.*, a left-handed neutrino converted into a right-handed antineutrino, both perfectly able to take part in weak interactions. A compelling argument in favour of  $CP$  was that, rigorously trusting  $CPT$  symmetry, the reversibility of time would naturally imply  $CP$  conservation. The observation of  $CP$  violation would suggest, for the first time in physics, the irreversibility of some processes at the fundamental level. Surprisingly though,  $CP$  was also revealed to be violated, first in the decays of  $K_L^0$  mesons [37] and later in the  $B^0$  system [38,39]. Since then,  $CP$  violation has also been seen to manifest in the  $B^+$  and  $B_s^0$  systems [40,41], the  $\Lambda_b^0$  baryon decays [42], and most recently in charm decays [43].

### 1.1.2 The CKM Matrix

The CKM (Cabibbo-Kobayashi-Maskawa) matrix is a  $3 \times 3$  complex unitary matrix that describes the possible mixings between the six different quarks and consists of the model to accommodate  $CP$  violation in electroweak theory. It was developed by Kobayashi and Maskawa [44] as an addition of a third quark generation to the Cabibbo matrix [45], which comprised at the time only half the quarks known today. In a general fashion, the mixing between the down-type quarks' mass and weak eigenstates can be written as

$$\begin{pmatrix} d' \\ s' \\ b' \end{pmatrix} = \begin{pmatrix} V_{ud} & V_{us} & V_{ub} \\ V_{cd} & V_{cs} & V_{cb} \\ V_{td} & V_{ts} & V_{tb} \end{pmatrix}_{\text{CKM}} \begin{pmatrix} d \\ s \\ b \end{pmatrix}, \quad (1.1)$$

where the primed states are the weak eigenstates.

In the CKM matrix, five out of nine components correspond to phases that can be absorbed into the phases of the quark fields. Four parameters remain: three real mixing angles and the KM complex phase, the only source of  $CP$  violation in the SM. The CKM matrix can be rewritten in terms of these parameters only, known as the ‘standard parametrisation’:

$$V_{\text{CKM}} = \begin{pmatrix} c_{12}c_{13} & s_{12}c_{13} & s_{13}e^{-i\delta} \\ -s_{12}c_{23} - c_{12}s_{23}s_{13}e^{i\delta} & c_{12}c_{23} - s_{12}s_{23}s_{13}e^{i\delta} & s_{23}c_{13} \\ s_{12}s_{23} - c_{12}c_{23}s_{13}e^{i\delta} & -c_{12}s_{23} - s_{12}c_{23}s_{13}e^{i\delta} & c_{23}c_{13} \end{pmatrix}, \quad (1.2)$$

where  $c_{ij} \equiv \cos \theta_{ij}$  and  $s_{ij} \equiv \sin \theta_{ij}$ ,  $\theta_{ij}$  corresponds to the Euler angles between families  $i$  and  $j$ , and  $\delta$  is the KM phase.

In addition, Wolfenstein [46] reached another useful parametrisation by noticing that  $s_{13} \ll s_{23} \ll s_{12} < 1$  and expanding in terms of  $s_{12} \equiv \lambda \approx 0.23$ . The CKM matrix can then be described using parameters  $\lambda$ ,  $A$ ,  $\rho$ , and  $\eta$ , which are frequently defined in relation to Equation 1.2 through  $s_{23} \equiv A\lambda^2$ , and  $s_{13}e^{i\delta} \equiv A\lambda^3(\rho - i\eta)$ . These definitions ensure that this parametrisation remains unitary to all orders in  $\lambda$ . The CKM matrix in the Wolfenstein parametrisation is given, up to  $\mathcal{O}(\lambda^3)$ , by

$$V_{\text{CKM}} = \begin{pmatrix} 1 - \frac{1}{2}\lambda^2 & \lambda & A\lambda^3(\rho - i\eta) \\ -\lambda & 1 - \frac{1}{2}\lambda^2 & A\lambda^2 \\ A\lambda^3(1 - \rho - i\eta) & -A\lambda^2 & 1 \end{pmatrix} + \mathcal{O}(\lambda^4). \quad (1.3)$$

In this parametrisation, the hierarchy of the CKM matrix easily presents itself: intra-generational couplings are strong,  $\mathcal{O}(1)$ , whereas couplings between first and third generations are very feeble.

The unitarity of the CKM matrix allows the construction of six orthogonality triangle relations between its different components, given by

$$\sum_i V_{ij}V_{ik}^* = \delta_{jk}, \quad \sum_j V_{ij}V_{kj}^* = \delta_{ik} \quad (1.4)$$

in the cases where  $\delta_{jk}, \delta_{ik} = 0$ . The six triangles have the same area, which is a measure of the total amount of  $CP$  violation in the SM.

It is conventional to take one of these relations in which all terms are of the same order in the expansion parameter  $\lambda$ ,

$$V_{ud}V_{ub}^* + V_{cd}V_{cb}^* + V_{td}V_{tb}^* = 0, \quad (1.5)$$

and dividing it by the best-determined term,  $V_{cd}V_{cb}^*$ , such that one of the sides is of unit length and the apex is the point  $\bar{\rho} + i\bar{\eta} \equiv -V_{ud}V_{ub}^*/V_{cd}V_{cb}^*$ . The parameters  $\bar{\rho}$  and  $\bar{\eta}$  are defined in terms of the other Wolfenstein parameters via

$$\rho + i\eta = \frac{\sqrt{1 - A^2\lambda^4}(\bar{\rho} + i\bar{\eta})}{\sqrt{1 - \lambda^2[1 - A^2\lambda^4(\bar{\rho} + i\bar{\eta})]}}, \quad (1.6)$$

from which the approximations  $\bar{\rho} \approx \rho(1 - \frac{\lambda^2}{2})$  and  $\bar{\eta} \approx \eta(1 - \frac{\lambda^2}{2})$  can be derived.

Equation 1.5, normalised by  $V_{cd}V_{cb}^*$ , is often referred to as the ‘unitarity triangle’ relation, whose illustration is shown in Figure 1.2. The three angles of the unitarity triangle are also accessible to experimental determination and are defined as:

$$\alpha = \arg\left(-\frac{V_{td}V_{tb}^*}{V_{ud}V_{ub}^*}\right), \quad \beta = \arg\left(-\frac{V_{cd}V_{cb}^*}{V_{td}V_{tb}^*}\right), \quad \gamma = \arg\left(-\frac{V_{ud}V_{ub}^*}{V_{cd}V_{cb}^*}\right). \quad (1.7)$$

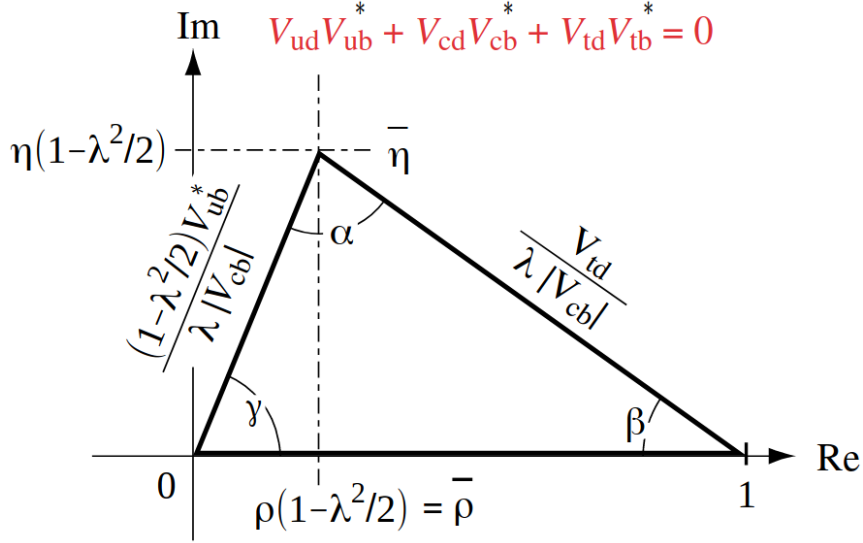


FIGURE 1.2: The unitarity relation given by Equation 1.5 drawn in the complex  $[\bar{\rho}, \bar{\eta}]$  plane [47].

The parameters of the CKM matrix cannot be determined from first principles in the SM, but must be determined *a posteriori*. This turns their experimental determination a central goal in modern particle physics. The same CKM parameters can be evaluated by a handful of distinct measurements, which helps both to refine the precision on these parameters and to ‘stress test’ the theory, with the hope of uncovering effects beyond the Standard Model.

At this point, the particles of interest for this work are introduced by Table 1.1.

Meson	Quark content	Rest mass (MeV/ $c^2$ )	Lifetime (s)
$B^+$ ( $B^-$ )	$u\bar{b}$ ( $\bar{u}b$ )	$5279.32 \pm 0.14$	$\sim 1.64 \times 10^{-12}$
$B^0$ ( $\bar{B}^0$ )	$d\bar{b}$ ( $\bar{d}b$ )	$5279.63 \pm 0.15$	$\sim 1.52 \times 10^{-12}$
$B_s^0$ ( $\bar{B}_s^0$ )	$s\bar{b}$ ( $\bar{s}b$ )	$5366.89 \pm 0.19$	$\sim 1.51 \times 10^{-12}$
$K^+$ ( $K^-$ )	$u\bar{s}$ ( $\bar{u}s$ )	$493.677 \pm 0.016$	$\sim 1.24 \times 10^{-8}$
$\pi^+$ ( $\pi^-$ )	$u\bar{d}$ ( $\bar{u}d$ )	$139.57061 \pm 0.00024$	$\sim 2.60 \times 10^{-8}$

TABLE 1.1: Summary of relevant pseudoscalar mesons and their physical properties [40].

$B$  mesons are pseudoscalars, *i.e.*, they have zero total spin and odd parity (usually noted as  $J^P = 0^-$ ), and are composed of a beauty quark (or antiquark) and a light ( $u, d, s$ ) antiquark (quark). Since the  $t$ -quark is too heavy to hadronise,  $B$  mesons are the heaviest ones found in nature.  $K$  mesons, or kaons, are distinguished by a quantum number called strangeness as they constitute bound states of a strange quark (or antiquark) and an up or down antiquark (or quark). Lastly,  $\pi$  mesons, or pions, consist of quarks (and antiquarks) from the first generation and are the lightest mesons.

## 1.2 Three-Body Kinematics

Electrons and protons and their antimatter counterparts are established as the only stable subatomic particles found in nature; all the remaining ones decay, *i.e.*, go

through the spontaneous process of transforming into other particles. Unstable particles will usually have multiple ways of decaying, or ‘decay channels’, each with its own associated probability.

The particles which were created in this phenomenon, also known as the final state of the decay, must each be less massive than the original, and the total invariant mass of the system must be conserved (see Subsection 3.1.1). Also, the final-state particles may themselves be unstable and prone to additional decays. In the SM, decays are mediated by one or a few of the fundamental forces.

In the decay context, a particle’s crucial observable is its mean lifetime  $\tau$ . It is firmly associated with the dominant interaction type that conducts the transition to its final state. The lifetime of a particle is given by the inverse of its total decay rate, the probability per unit time that the particle will decay,  $\tau = 1/\Gamma_{\text{total}}$ .  $\Gamma_{\text{total}}$  is in turn defined as  $\Gamma_{\text{total}} = \sum_i \Gamma_i$ , where  $\Gamma_i$  corresponds to the decay rate of each channel.

From the Fermi’s golden rule, the specific differential decay rate of a particle with mass  $M$  and four-momentum  $P$ , bringing about a  $n$  final-state particles, each with mass  $m_i$  and four-momenta  $p_i$  and energy  $E_i$  is given by [40]:

$$d\Gamma = \frac{|\mathcal{M}|^2}{2M} (2\pi)^4 \delta^4 \left( P - \sum_{i=1}^n p_i \right) \prod_{i=1}^n \frac{d^3 \vec{p}_i}{2(2\pi)^3 E_i}, \quad (1.8)$$

where the term  $\frac{|\mathcal{M}|^2}{2M}$  refers to the dynamics of the particular decay, embedded in the ‘amplitude’  $\mathcal{M}$ , and the rest of the expression corresponds to an element of the ‘phase space’, *i.e.*, the space in which all accessible final states of the decay are represented.

In two-body decays of spin-0 particles, conservation of momentum ensures that the momenta of the decay products are equal and oppositely-directed in the rest frame of the original particle. Given the isotropy of the problem, the only actual degree of freedom is the arbitrary choice of decay axis. By contrast, three-body decays – or more generally, any multi-body decay – possess additional degrees of freedom and each decay product can seize different amounts of the total energy available.

A generic set of three spin-0 particles holds 12 degrees of freedom in full: all the three four-momenta components. Three degrees of freedom are removed by means of information regarding the three particles’ masses, while conservation of four-momentum removes another four. In the specific case where both initial and all final-state particles are spin-0, the angular dependence is eliminated, that is, the decay distribution must be isotropic in the rest frame of the decaying particle, and this gets rid of three additional degrees of freedom. In conclusion, a spinless three-body decay can be fully described by just a pair of variables.

In 1953, Richard Dalitz established a technique to make use of these two variables and conveniently represent three-body decays in a two-dimensional plot [48], where characteristic patterns express information about the spin and parity of the decaying particles. It was first employed to describe and investigate the  $\tau \rightarrow \pi^+ \pi^+ \pi^-$  decay, revealing the nature of the  $\tau$ -meson by determining its spin and parity.

Contemporarily, these Dalitz plots (DP) are constructed using pairs of two-body invariant mass combinations as the coordinate axes. Consider a three-body decay whose final-state particles are labelled as  $P_i$ , with  $i \in \{1, 2, 3\}$ . The available combinations of two particles are:  $P_1 P_2$ ,  $P_2 P_3$  and  $P_1 P_3$ . Then, the Dalitz variables are

defined as:

$$\begin{aligned} s_{12} &= m_{12}^2 = (p_1 + p_2)^2, \\ s_{23} &= m_{23}^2 = (p_2 + p_3)^2, \\ s_{13} &= m_{13}^2 = (p_1 + p_3)^2, \end{aligned} \quad (1.9)$$

where  $p_i$  are the four-momenta of the  $P_i$  particle, and  $s_{ij}$  correspond to Mandelstam variables.

The choice among the available pairs ( $m_{12}^2$ ,  $m_{23}^2$ ,  $m_{13}^2$ ) for representing the DP depends on the specific decay being studied. In particular, for a decay with three identical particles, two of them have the same charge and so are indistinguishable. In this case, the DP is symmetrised and its axes are chosen as the lower and the higher values of the possible Dalitz variables. Taking, for instance, the  $B^\pm \rightarrow \pi^\pm \pi^+ \pi^-$  decay, the DP chosen axes are:  $m^2(\pi^+ \pi^-)_{\text{low}}$  and  $m^2(\pi^+ \pi^-)_{\text{high}}$ .

Finally, the Dalitz plot is a two-dimensional representation of the decay phase space, which means that each accessible final-state configuration corresponds to a dot in the DP and that the distribution of events is directly proportional to the total amplitude squared. Furthermore, the boundaries of the phase space are delimited by the kinematics of the decay, *i.e.*, the four-momentum conservation, as illustrated in Figure 1.3.

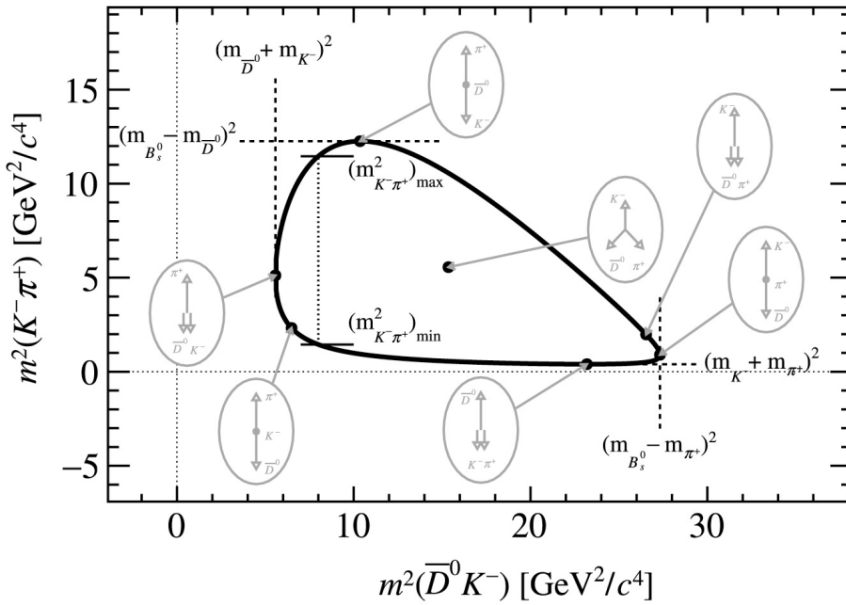


FIGURE 1.3: The Dalitz plot kinematic boundaries and the corresponding momentum configurations of the three final-state particles in  $B_s^0 \rightarrow \bar{D}^0 K^- \pi^+$  decays at points of interest in the DP [49].

As a special case of Equation 1.8, the differential decay rate of a three-body decay is given by

$$d\Gamma = \frac{1}{32(2\pi)^3 M^3} |\mathcal{M}|^2 dm_{12}^2 dm_{23}^2. \quad (1.10)$$

If  $\mathcal{M}$  is constant, the allowed phase space is uniformly populated with events and any minor variation in event distribution over the DP is due to dynamic effects resulting from the interference of the quantum-mechanical amplitudes of the final state particles.

For the most part, however, a three-body decay goes on by way of a number of intermediate quasi-two-body decays, *e.g.*,  $B^\pm \rightarrow \pi^\pm R^0$ , where  $R^0$  is a neutral resonant state such as  $\rho(770)^0$  or  $f_2(1270)$ , which decays through  $R \rightarrow \pi^+ \pi^-$ . These resonances are particles that interact via the strong force and have a very short lifetime ( $\sim 10^{-23}$  s), in contrast to situations where the decaying particle disintegrates directly into three final-state particles as displayed in Figure 1.4.

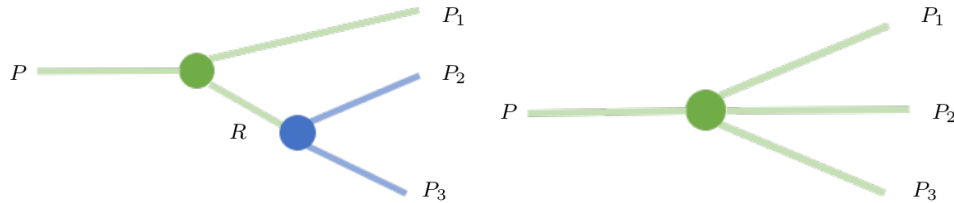


FIGURE 1.4: Illustration of a resonant (left) and a non-resonant (right) three-body decay [50].

The contributions of different resonant states manifest themselves in the DP as bands at the value of the resonance mass squared in the corresponding  $m_{ij}^2$  variable, stretching across the other DP axis. Moreover, the resonance's spin will show in the shape of the resonant band: a scalar ( $J^P = 0^+$ ), will generate a uniformly populated band, a vector ( $J^P = 1^-$ ) generates a two-lobe structure, and a tensor ( $J^P = 2^+$ ) generates three-lobe bands. Lastly, interference effects between different intermediate states are also reflected in the Dalitz plot. An example of a Dalitz plot with multiple contributing resonances is provided in Figure 1.5 to the left.

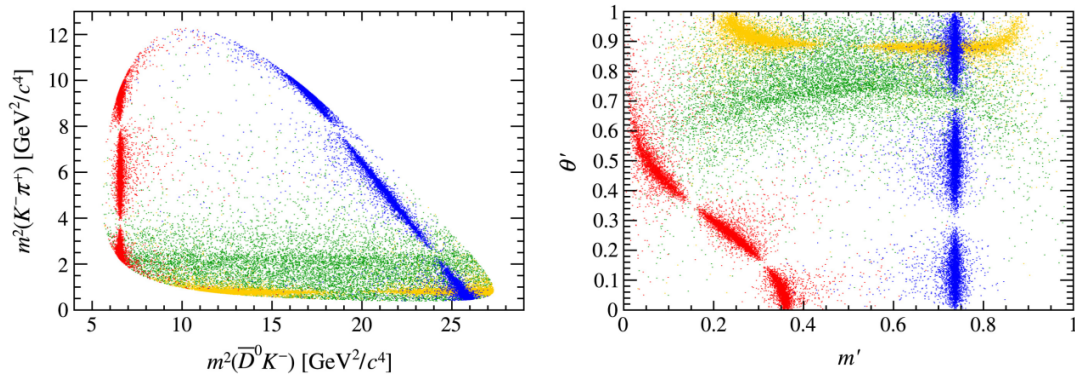


FIGURE 1.5: Illustration of the  $B_s^0 \rightarrow \bar{D}^0 K^- \pi^+$  decay Dalitz plot with intermediate scalar (green), vector (yellow), and tensor (red and blue) highlighted contributions. Interference effects are not included in this illustration. Both conventional (left), and square (right) representations are displayed [49].

In  $B$ -meson decays, events largely fall near the kinematic boundaries of the Dalitz plot. Thus, it is convenient in these cases to apply a coordinate transformation that expands the edge regions such that variations resulting from resonance interference and/or experimental effects can be studied more easily. The 'square Dalitz plot' (SDP) is a transformation of the kind, which reshapes the kinematically-allowed region into a square with unit-length sides. The coordinates of this new representation

are defined as

$$m' \equiv \frac{1}{\pi} \cos^{-1} \left( 2 \frac{m_{ij} - m_{ij}^{\min}}{m_{ij}^{\max} - m_{ij}^{\min}} - 1 \right), \quad (1.11)$$

$$\theta' \equiv \frac{1}{\pi} \theta_{ij},$$

where  $m_{ij}^{\min} = m_i + m_j$ ,  $m_{ij}^{\max} = M_B - m_k$ , and  $\theta_{ij}$  is the angle between  $i$  and  $k$  in the rest frame of  $ij$ , *i.e.*, the resonance rest frame. The effect of the SDP transformation on the different regions of the conventional DP can be seen in Figure 1.5 to the right.

## 1.3 $CP$ Violation in $B^\pm$ Decays

### 1.3.1 Direct $CP$ Violation

The complex phase in the CKM matrix is the exclusive source of  $CP$  violation in the SM. Although, a non-zero CKM phase, or ‘weak phase’, is not a sufficient condition for observable  $CP$ -violating effects in the quark sector.  $CP$  violation can only manifest itself in processes to which multiple amplitudes contribute, as resolved in the following.

The mechanisms for generating such interferences in  $B$  decays fall into three categories:

1.  **$CP$  violation in decays:** also known as ‘direct’  $CP$  violation, happens to both neutral and charged  $B$  mesons when the decay rate of a particle  $P$  to a given final state  $f$  differs from the conjugate process:

$$\Gamma(P \rightarrow f) \neq \Gamma(\bar{P} \rightarrow \bar{f}). \quad (1.12)$$

2.  **$CP$  violation in the mixing:** also called indirect  $CP$  violation, occurs when the transition of a neutral meson to its antiparticle, *e.g.*,  $B^0 \rightarrow \bar{B}^0$ , has a different probability with respect to its  $CP$ -conjugate process,  $\bar{B}^0 \rightarrow B^0$ .

$$\Gamma(P^0 \rightarrow \bar{P}^0) \neq \Gamma(\bar{P}^0 \rightarrow P^0) \quad (1.13)$$

3.  **$CP$  violation in the interference between mixing and decay:** occurs in decays whose final states are common to, for instance,  $B^0$  and  $\bar{B}^0$ . In other words, this type of  $CP$  violation is a result from the fact that  $B^0$  can either directly decay into the final state  $f$  or first oscillate to  $\bar{B}^0$  and then decay to the same state  $f$ .

$$\Gamma(P^0 \rightarrow f) \neq \Gamma(P^0 \rightarrow \bar{P}^0 \rightarrow f) \quad (1.14)$$

Charged particles are prohibited to mix due to charge conservation, thus the last two types of  $CP$  violation are restricted to neutral meson decays. Since this work concerns charged  $B$ -meson decays, this thesis will focus on direct  $CP$  violation, about which a more detailed discussion is given hereafter.

In terms of the decay amplitudes,  $CP$  violation in a decay corresponds to the situation when

$$|A(P \rightarrow f)|^2 - |A(\bar{P} \rightarrow \bar{f})|^2 \neq 0 \quad (1.15)$$

This supplementary requirement can be shown by considering that the amplitudes for the two processes can be generally written as

$$\begin{aligned} A_f &\equiv A(P \rightarrow f) = \sum_k |a_k| e^{i(\delta_k + \phi_k)}, \\ \bar{A}_{\bar{f}} &\equiv A(\bar{P} \rightarrow \bar{f}) = \sum_k |a_k| e^{i(\delta_k - \phi_k)}, \end{aligned} \quad (1.16)$$

where  $\phi_k$  are weak phases, which change sign under  $CP$  ( $CP$ -odd),  $\delta_k$  are ‘strong phases’, the phase components largely produced by strong-force effects, *e.g.*, quark loops and hadronic final-state interactions, which do not change sign under  $CP$  ( $CP$ -even), and  $k$  labels the possible contributing processes. It is the relative phase between two partial amplitudes, rather than the individual phase, that generally leads to observable consequences. In the situation where the decay proceeds via a single amplitude, it is trivial that there can be no  $CP$ -violating amplitude difference:

$$\begin{aligned} |A_f|^2 - |\bar{A}_{\bar{f}}|^2 &= |a_1|^2 e^{i(\delta_1 + \phi_1)} e^{-i(\delta_1 + \phi_1)} - |a_1|^2 e^{i(\delta_1 - \phi_1)} e^{-i(\delta_1 - \phi_1)} \\ &= |a_1|^2 - |a_1|^2 \equiv 0. \end{aligned} \quad (1.17)$$

Thus,  $CP$  violation emerges naturally when multiple amplitudes can interfere with each other, *e.g.*, tree- and loop-level contributions (later described in Section 1.4).

Consider now the following amplitudes:

$$\begin{aligned} A_f &= |a_1| e^{i(\delta_1 + \phi_1)} + |a_2| e^{i(\delta_2 + \phi_2)} \\ \bar{A}_{\bar{f}} &= |a_1| e^{i(\delta_1 - \phi_1)} + |a_2| e^{i(\delta_2 - \phi_2)}. \end{aligned} \quad (1.18)$$

These interfering amplitudes may represent, for instance, two different Feynman diagrams resulting in the same final state. Note that:

$$|A_f|^2 - |\bar{A}_{\bar{f}}|^2 = 2|a_1||a_2| \sin(\delta_1 - \delta_2) \sin(\phi_1 - \phi_2). \quad (1.19)$$

Thus,  $CP$  violation arises from processes with interfering amplitudes with different weak and strong phases. A more interesting quantity that can be observed by experiments is the  $CP$  asymmetry,  $\mathcal{A}_{CP}$ , which can be written as:

$$\mathcal{A}_{CP} = \frac{|A_f|^2 - |\bar{A}_{\bar{f}}|^2}{|A_f|^2 + |\bar{A}_{\bar{f}}|^2}. \quad (1.20)$$

Substituting Eqs. 1.18 into Eq. 1.20, it gives:

$$\mathcal{A}_{CP} = \frac{2|a_1||a_2| \sin(\delta_1 - \delta_2) \sin(\phi_1 - \phi_2)}{|a_1|^2 + |a_2|^2 + 2|a_1||a_2| \cos(\delta_1 - \delta_2) \cos(\phi_1 - \phi_2)}. \quad (1.21)$$

One even notes that the size of the  $CP$  asymmetry depends not only on phase differences but also on the relative size of the two amplitudes.

Finally, although the usual observable when searching for  $CP$  violation in decays is the  $CP$  asymmetry, experimentally, in the case of  $B^\pm$  mesons for instance, one measures the particle and antiparticle yields,  $N_{sig}^+$  and  $N_{sig}^-$ , respectively, which are affected by a chain of effects from production, reconstruction, and final selection of events. Then, the observed raw charge asymmetry is defined as

$$A_{RAW} \equiv \frac{N_{sig}^- - N_{sig}^+}{N_{sig}^- + N_{sig}^+}, \quad (1.22)$$

which still needs to be corrected for eventual production and detection asymmetries.

### 1.3.2 *CPT* Constraint

For a particle decaying exclusively via weak force, the initial state is stable under strong (and electromagnetic) interactions. Conversely, after the weak transition, the final state is the potential result of strong processes associating states with the same quantum numbers. As mentioned earlier, strong phases are in fact also the result of these final-state interactions (FSI). For instance, the total amplitude of the decay of  $P$  to a given final state  $f$  may include contributions as  $P \rightarrow f_i \rightarrow f, i \in \{1, 2, \dots, n\}$ , where  $P \rightarrow f_i$  incorporates the weak transition, and  $f_i \rightarrow f$  the strong processes (elastic or inelastic scatterings). At this point, it is interesting to discuss *CP* violation in the context of *CPT* constraints.

The *CPT* symmetry establishes that the lifetimes,  $\tau$ , (therefore, the total decay widths,  $\Gamma_{\text{total}}$ ) of both particle and its antiparticle are the same. On the other hand, *CP* violation allows for different partial decay widths,  $\Gamma_i$ . Evidently, preserving the equality of total widths for particle and antiparticle while allowing partial widths to be different requires a ‘communication’ between the different decay modes, and this can only happen within modes that have the same flavour quantum numbers.

Thus, final-state interactions which connect states via strong (or electromagnetic) force provide the natural strong phases for *CP* violation to be observable, and are also the key ingredient to allow the preservation of *CPT* symmetry. The central message here is that *CPT* constrains not only the total widths of particle and antiparticle to be the same, but also the sum of partial widths to final states with the same quantum numbers.

$$\sum_i \Delta\Gamma(P \rightarrow f_i) = 0 \quad (1.23)$$

This means, for instance, that if a sizeable positive *CP* asymmetry is found in a given decay mode, there should be strongly-coupled final states with negative *CP* asymmetry to compensate.

### 1.3.3 Theoretical and Experimental Approaches

From the theory side, direct *CP* asymmetry in charmless heavy-meson decays has served as a long and fascinating puzzle over the last decades. It has been extensively examined ever since the seminal Bander, Silverman and Soni’s article [51], published in the late ’70s, which introduced the hypothesis now established as the ‘BSS mechanism’ (see Section 1.4). A reasonable consensus states that the strong phases coming from short-distance effects should be small. If these are taken to be the primary source of strong phases, the level of direct *CP* violation should be correspondingly limited. On the other hand, if one considers that long-distance processes in non-leptonic decays, involving FSI, introduce substantial strong-phase shifts, potentially large direct *CP*-violation effects should be expected.

The current most commonly adopted method to calculate branching fractions and *CP* asymmetries of charmless  $B$ -meson decays is the factorization of the decay amplitude, which was disseminated by the ‘naive’ factorization approach [52]. The breakthrough came in the ’80s by the influential work of Lepage and Brodsky [53], which constitutes the basis for the main frameworks developed to study exclusive

heavy-meson decays. For the  $B$  meson, those main approaches are: QCD factorization (QCDF) [54], perturbative QCD (pQCD) [55] and soft-collinear effective theory (SCET) [56].

Overall, these approaches overlook the constraint that  $CPT$  invariance imposes on  $CP$  asymmetry at the hadronic level by only considering short-distance amplitudes. For a long time, it was presumed that  $B$  mesons would generate many hadronic decay channels with a homogeneous momentum distribution over the phase space: from the allowed rescattering processes up to several hadronic channels. These possible FSI, involving two, three or more hadrons, suggested that  $CPT$  constraints would not be of practical application in charmless  $B$  decays [57]. Nonetheless, more recently, a more abundant sample of experimental data coming from  $B$  factories, at first BaBar and Belle and now LHCb, showed that these multi-meson rescattering processes are not dominant in charmless multi-body  $B$  decays [58, 59].

In the extensive compilation of  $B$  charmless processes presented in Ref. [60], one finds a fair agreement between theories based on factorization techniques and experimental results available for several branching fractions of  $B \rightarrow PP$  and  $B \rightarrow PV$  decays, involving pseudoscalar  $P$  and vector  $V$  mesons. Yet, the same agreement fails to be seen for values of  $CP$  asymmetries from such channels. In fact, there are many discrepancies not only among the different models but also from comparing their results to experimental  $CP$ -asymmetry measurements. Although this situation is worse for  $B \rightarrow PV$  decays, it is important to emphasise that issues are present for both theoretical and experimental descriptions. In the latter,  $B \rightarrow PV$  processes are indeed three-body decays and consequently the observables are determined inside the complexity of a three-body phase space.

Experimentally, given the CKM matrix hierarchy (Equation 1.3), the natural sectors to observe  $CP$  violation are processes involving strange and beauty hadrons. For three or more final-state particles, besides the measurement of the (total) charge asymmetry,  $CP$  violation can be studied through the decay phase-space distribution. As mentioned in Section 1.2, regarding  $B$ -meson decays, the process is mostly dominated by the formation of resonances as intermediate states, which then decay strongly or electromagnetically to form the detectable final state. The distribution of events throughout the phase space is the result of the superposition of the various amplitudes, and the interference pattern depends directly on the strong and weak phases involved. The rich dynamics potentially allow different sources of strong phases to appear. It is then natural to expect localised  $CP$  asymmetries to be stronger than phase-space integrated ones, and they can even change sign. Altogether these features make multi-body decays an excellent tool for studying  $CP$  violation in the hadronic sector.

With the intent of measuring or searching for  $CP$  violation over the phase space, one seeks two approaches: model-dependent and model-independent analyses. The former is based on an amplitude-analysis fit: the decay amplitude is modelled as a coherent sum of intermediate states such that their relative contributions can differ for particle and antiparticle decays. In model-independent strategies, phase-space distributions for particle and antiparticle decays are directly compared to look for regions where there are statistically significant differences, and then localised asymmetries can be measured. The two procedures are complementary: while model-independent techniques can specify the phase-space regions where  $CP$  violation manifests, amplitude analysis can identify its dynamical source.

The simplest and most common approach for an amplitude analysis is the so-called ‘isobar model’, where the total amplitude is described as a coherent sum of a

number of amplitudes describing the different intermediate states:

$$\mathcal{M}(m_{ij}^2, m_{jk}^2) = \sum_R c_R F_R(m_{ij}^2, m_{jk}^2), \quad (1.24)$$

where  $F_R$  encapsulates the dynamics (such as the lineshape and spin-dependence) of the intermediate state  $R$ , and  $c_R$  describes the relative magnitude and phase of the different states – such parameters to be determined by the amplitude fit. The decay amplitude of the  $CP$ -conjugate state,  $\bar{\mathcal{M}}$ , can be constructed in terms of  $\bar{c}_R$  and  $\bar{F}_R$ .

For phase-space integrated measurements in multi-body decays,  $\mathcal{A}_{CP}$  is obtained directly from the event yields from particle and antiparticle decays, correcting for experimental asymmetries when applicable; while for resonant intermediate states, model-independent techniques may be exploited.

## 1.4 Charmless Three-Body $B^\pm$ Decays

The charmless three-body decays of a charged  $B$  meson, hereafter designated as  $B^\pm \rightarrow h^\pm h^+ h^-$ , where  $h^\pm$  represent charged pions and kaons, have collectively stood as an active area of experimental study for the last thirty years. The following decays are included:  $B^\pm \rightarrow K^\pm \pi^+ \pi^-$ ,  $B^\pm \rightarrow K^\pm K^+ K^-$ ,  $B^\pm \rightarrow \pi^\pm \pi^+ \pi^-$  and  $B^\pm \rightarrow \pi^\pm K^+ K^-$ . Yet,  $CP$  violation in local regions of the Dalitz plot for  $B^\pm \rightarrow h^\pm h^+ h^-$  decays was first observed in 2013 by the LHCb collaboration [61, 62]. Integrated  $CP$  asymmetries along the phase space were then measured by the same collaboration in the next year [21], using the total available sample taken between 2011 and 2012. The studies have uncovered sizeable integrated  $CP$  asymmetries but also confirmed rich structures of  $CP$  asymmetries across the phase space. The results for the integrated  $CP$  asymmetries were

$$\begin{aligned} \mathcal{A}_{CP}(B^\pm \rightarrow K^\pm \pi^+ \pi^-) &= +0.025 \pm 0.004 \pm 0.004 \pm 0.007, \\ \mathcal{A}_{CP}(B^\pm \rightarrow K^\pm K^+ K^-) &= -0.036 \pm 0.004 \pm 0.002 \pm 0.007, \\ \mathcal{A}_{CP}(B^\pm \rightarrow \pi^\pm \pi^+ \pi^-) &= +0.058 \pm 0.008 \pm 0.009 \pm 0.007, \\ \mathcal{A}_{CP}(B^\pm \rightarrow \pi^\pm K^+ K^-) &= -0.123 \pm \underbrace{0.017}_{\sigma_{\text{stat}}} \pm \underbrace{0.012}_{\sigma_{\text{syst}}} \pm \underbrace{0.007}_{\sigma_{J/\psi K^\pm}}, \end{aligned} \quad (1.25)$$

where the first uncertainties are statistical, the second, systematic and the third comes from the  $CP$  asymmetry of the  $B^\pm \rightarrow J/\psi K^\pm$  reference mode. The statistical significances of the  $CP$  asymmetries were respectively 2.8, 4.3, 4.2, and  $5.6\sigma$ . The  $B^\pm$  candidates found were about 180 thousand for  $B^\pm \rightarrow K^\pm \pi^+ \pi^-$ , 110 thousand for  $B^\pm \rightarrow K^\pm K^+ K^-$ , 25 thousand for  $B^\pm \rightarrow \pi^\pm \pi^+ \pi^-$  and 6 thousand for  $B^\pm \rightarrow \pi^\pm K^+ K^-$ .

Table 1.2 lists the  $B^\pm \rightarrow h^\pm h^+ h^-$  channels with their corresponding ‘branching fractions’, determined by the channel decay rate divided by the total decay rate ( $\Gamma_i/\Gamma_{\text{total}}$ ), *i.e.*, it represents the probability for that decay to happen. These decay channels are so rare that their analyses is only made possible by high-luminosity experiments, such as the LHCb (described in Chapter 2).

As previously discussed, the presence of at least two amplitudes, with different weak and strong phases, is a requirement for the manifestation of  $CP$  violation in decays. While weak phases in the SM appear from specific CKM matrix elements, strong phases can appear from different sources. At short distances, a  $CP$  asymmetry may come from the BSS mechanism, namely, interference between ‘tree’ and ‘penguin’ quark-level diagrams owning different weak and strong phases.

Decay	BF
$B^\pm \rightarrow K^\pm \pi^+ \pi^-$	$(5.10 \pm 0.29) \times 10^{-5}$
$B^\pm \rightarrow K^\pm K^+ K^-$	$(3.40 \pm 0.14) \times 10^{-5}$
$B^\pm \rightarrow \pi^\pm \pi^+ \pi^-$	$(1.52 \pm 0.14) \times 10^{-5}$
$B^\pm \rightarrow \pi^\pm K^+ K^-$	$(5.2 \pm 0.4) \times 10^{-6}$

TABLE 1.2: Branching fractions for the  $B^\pm \rightarrow h^\pm h^+ h^-$  decay channels [40].

Hadronic  $B$  decays are mediated by  $b \rightarrow q_1 \bar{q}_2 d(s)$  quark-level transitions, with  $q_1, \bar{q}_2 \in \{u, d, c, s\}$ . The topologies of weak-decay Feynman diagrams that contribute to  $B$  decays are generally divided into two sorts: tree and penguin diagrams.

Tree diagrams are processes that emit a  $W^\pm$  boson, which decays into two new quarks, and do not involve internal loops. The penguin processes are those which include internal loops: a  $W$  boson is reabsorbed on the same quark line from which it originates, and a gluon is emitted, which decays into two quarks. The diagram types are illustrated in Figure 1.6.

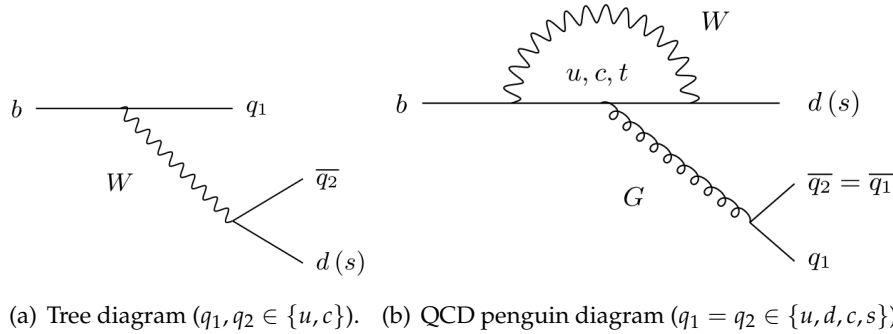


FIGURE 1.6: Tree and Penguin diagrams [63].

The most prevalent decay type, though, for  $B$  mesons are charmed decays, involving  $D$  and  $J/\psi$  mesons, because the  $b \rightarrow c$  transition is CKM favoured. Other transitions such as  $b \rightarrow u$  are CKM suppressed by  $|V_{ub}|$ . For this reason, charmless decays are less frequent than the charmed and charmonium decays. Such decays are tree-level processes, whereas decays of  $b$ -quarks to  $s$ - or  $d$ -quarks can only take place via penguin diagrams. Charmless hadronic decays such as the subject of this thesis have contribution from both penguin and tree-level process.

Still from Ref. [21], the  $CP$  asymmetries across the phase space for the four channels were obtained through the Miranda technique [64] and are reproduced in Figure 1.7. The method enhances local effects by obtaining asymmetries through the division of the DP in bins of equal population for the combined samples of particle and antiparticle decays. Rich  $CP$  violation patterns can be seen along the Dalitz plots, with positive (red) and negative (blue)  $CP$  asymmetries coexisting in the same final state. They represent a clear evidence of how  $CP$  violation effects can be substantially stronger in regions of the phase space when compared to the total, integrated  $CP$  effect.

The phase-space integrated  $CP$ -asymmetry measurements to  $B^\pm \rightarrow h^\pm h^+ h^-$  decays reported by this thesis (Chapter 4) serve as an update to the ones listed in Eqs. 1.25. The used LHCb data sample was recorded between 2015 and 2018 and

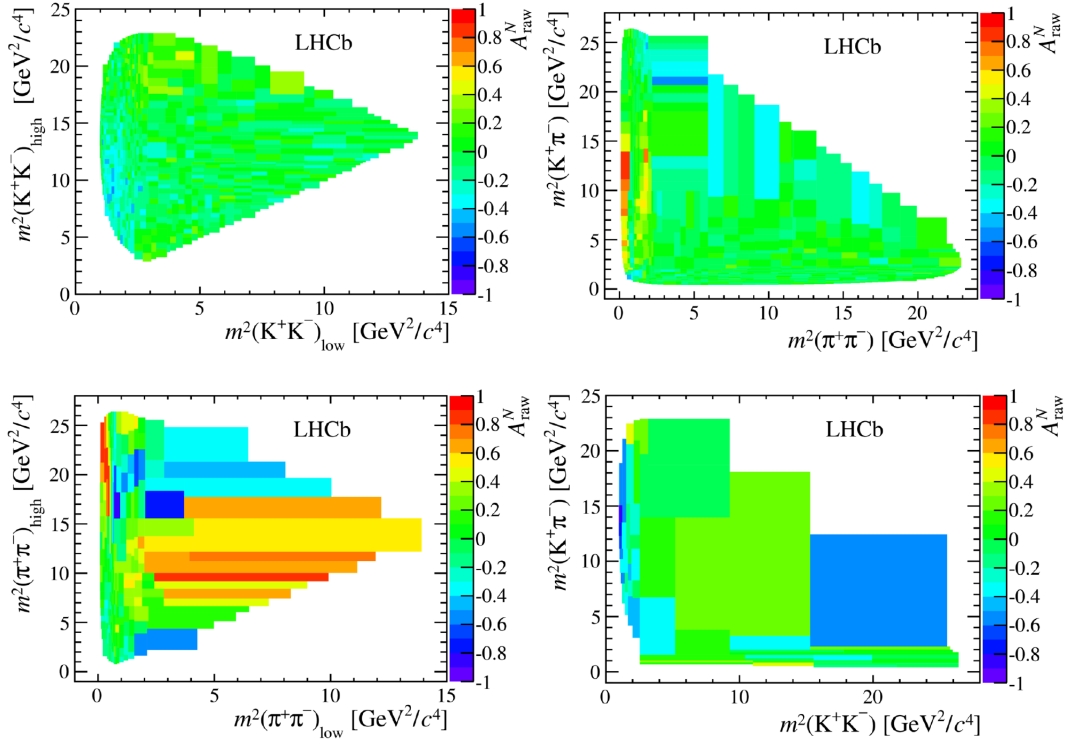


FIGURE 1.7:  $CP$  asymmetry distributions with the Miranda technique, with background-subtracted and acceptance-corrected events for: (top left)  $B^\pm \rightarrow K^\pm K^+ K^-$ , (top right)  $B^\pm \rightarrow K^\pm \pi^+ \pi^-$ , (bottom left)  $B^\pm \rightarrow \pi^\pm \pi^+ \pi^-$  and (bottom right)  $B^\pm \rightarrow \pi^\pm K^+ K^-$ . Taken from Ref. [21].

corresponds to at least four times the data size of the previous measurement. A complementary second set of measurements (Chapter 5) is performed, by means of a model-independent method, over  $B$  decays involving neutral vector resonances, of which few experimental results have been published yet.



## Chapter 2

# The LHCb Experiment

The work described in this thesis uses data collected by the Large Hadron Collider beauty (LHCb) experiment, located at one of the collision points of the Large Hadron Collider (LHC) at CERN. This chapter contextualises CERN and the LHC scientific activity in Section 2.1, and pinpoints the LHCb experimental pursuit in Section 2.2. Particularly, more in-depth discussions about LHCb’s subdetectors, dedicated to tracking and particle identification, take place in Sections 2.3 and 2.4, respectively. Finally, a brief description of the LHCb’s trigger system can be found in Section 2.5. Information on the LHC is mainly derived from Ref. [65], while information on LHCb comes primarily from Refs. [66, 67]; other sources are indicated throughout.

### 2.1 The Large Hadron Collider

At the end of the Second World War, European science was no longer dominant. Following the example of international organisations, a handful of visionary scientists imagined creating a European atomic physics laboratory. Then, at an intergovernmental meeting of UNESCO in Paris, 1951, the first resolution concerning the establishment of a European Council for Nuclear Research (in French, *Conseil Européen pour la Recherche Nucléaire* – CERN) was adopted [68]. In 1954, construction began in Geneva, Switzerland, and the convention establishing CERN was ratified by the 12 founding nations. The European Organization for Nuclear Research was created but the acronym CERN remained. The convention clearly determined its main missions [69]:

“The Organization shall provide for collaboration among European States in nuclear research of a pure scientific and fundamental character (...). The Organization shall have no concern with work for military requirements and the results of its experimental and theoretical work shall be published or otherwise made generally available”.

Today, our understanding of matter goes much deeper than the nucleus, as we know there are more fundamental building blocks of our universe, and CERN’s main area of research is particle physics. Since its inception, many significant breakthroughs have been made, both in particle physics (such as the discovery of the field particles  $W$  and  $Z$ , communicators of the weak interaction) and technologies that have helped improve our day-to-day lives (including the World Wide Web).

The essential aim of a high-energy physics experiment is to describe fundamental particles and enlighten their interactions. Accelerators are the main tool to achieve that because they solve two problems for physicists: the production of new particles and states, and the investigation of the detailed structure of subatomic systems. Essentially, an accelerator takes a particle, speeds it up with electromagnetic fields, and

smashes it into a target or other particles. Surrounding the collision point, detectors are positioned to record the many pieces of the event.

The Large Hadron Collider is the world's largest and most powerful particle accelerator, a 27 km circular collider located between 45 and 170 m deep under the Franco-Swiss border at CERN. It is a two-ring hadron accelerator and makes use of thousands of superconducting magnets to bend (dipole magnets) and tighten (quadrupole magnets) particles' trajectories. Also, it is primarily designed to collide a pair of proton beams, or  $pp$  collisions, travelling at almost the speed of light at centre-of-mass energies,  $\sqrt{s}$ , of up to 14 TeV, as well as lead ion beams up to an energy of 2.8 TeV per nucleon. The energy is a crucial parameter for it determines the mass threshold of the particles that can be produced.

The LHC is the final step in a long chain of particle accelerators required to boost particle energies up to the TeV range. A comprehensive illustration of the accelerator complex is shown in Figure 2.1. In the first step of the chain, protons, produced by ionising hydrogen, are accelerated in a linear accelerator, LINAC2, to an energy of 50 MeV. Next up, the beam is injected into a sequence of successively larger circular accelerators: the Proton Synchrotron Booster (PSB), the Proton Synchrotron (PS), and the Super Proton Synchrotron (SPS), which raise the beam energy to 1.4 GeV, 25 GeV, and 450 GeV respectively. After exiting the SPS, the beam is split in two; the resulting beams are then transferred to the LHC beam pipes, in which they circle in opposite directions. The two beams are then accelerated up to their individual collision energies: in 2011, this energy was 3.5 TeV per beam; in 2012, 4 TeV; finally, between 2015-2018, the beam energy reached 6.5 TeV.

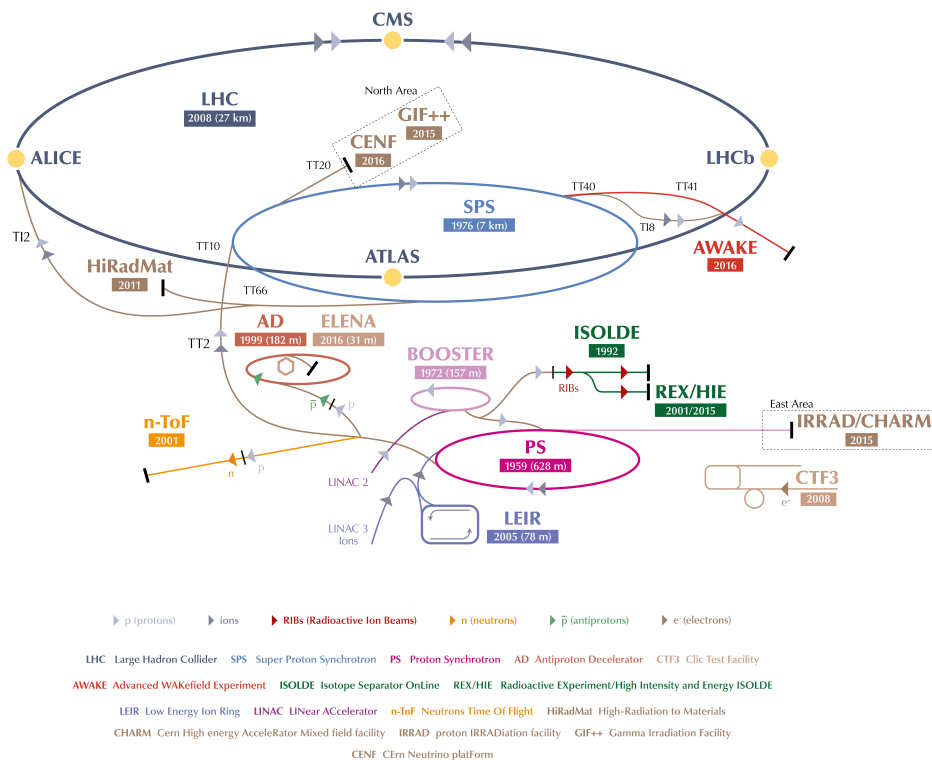


FIGURE 2.1: CERN accelerator complex and experiments [70].

Especially, the most interesting physics results come from very rare events. Hence,

accelerator are required to produce an immense amount of collisions in order to generate such events and have the opportunity to detect them. The instantaneous luminosity  $\mathcal{L}$  is a measure of the number of collisions that take place in a detector per  $\text{cm}^2$  and per second and can be obtained semiquantitatively from [71]:

$$\mathcal{L} \propto \frac{fN^2}{4\pi\sigma^2}, \quad (2.1)$$

where  $N$  is the number of particles in each bunch,  $\sigma$  is the transversal size of the bunch at the interaction point, and  $f$  is the bunch crossing frequency.

The LHC beams are not continuous beams but are composed of a number of proton bunches, with a designed maximum of 2808 bunches per beam, each bunch containing  $\mathcal{O}(10^{11})$  protons. The minimum spacing between bunches is 25 ns, corresponding to a bunch crossing frequency of 40 MHz. The maximum design instantaneous luminosity is  $\sim 10^{34} \text{cm}^{-2} \text{s}^{-1}$ , although operations to date have seen the machine achieve peak instantaneous luminosities of approximately double this number. Particularly, the LHCb detector operates at a much lower instantaneous luminosity, for reasons discussed in Section 2.2.

The main data-taking periods to date have been 2011-2012 and 2015-2018, known as Run 1 and 2, respectively. The long shutdown between the runs was necessary to prepare the machine for operation at higher energies and overall renovation work. A second shutdown, Long Shutdown 2, has started in 2019 and will continue until 2021. A major upgrade, the LHCb Upgrade 1, [72] is currently being commissioned for the start of Run 3 of LHC in 2021.

The integral of the delivered luminosity over time is called integrated luminosity. It is a measurement of the collected data size, and it is an important value to characterize the performance of an accelerator. Commonly, it is expressed in inverse of cross section, most commonly inverse femtobarn,  $\text{fb}^{-1}$ . Figure 2.2 shows comparison of integrated luminosity recorded by the LHCb experiment during different  $pp$  data-taking periods.

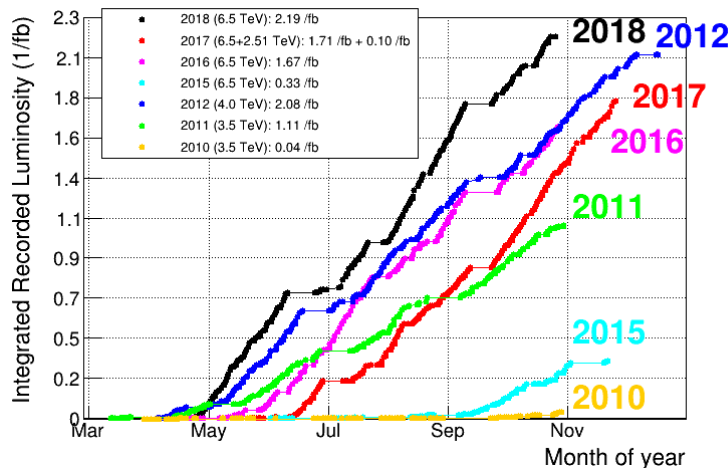


FIGURE 2.2: Recorded integrated luminosities in the LHCb for each year of operation and their corresponding collision energies. [73]

In 2018, LHCb recorded  $2.19 \text{fb}^{-1}$ , the best performance ever achieved and slightly higher than the value obtained in 2012, the last year of Run 1. The total luminosity collected in Run 2 is nearly  $6 \text{fb}^{-1}$ , twice the Run 1 sample of  $3 \text{fb}^{-1}$ . Moreover, since the cross-section for  $b$ - and  $\bar{b}$ -quark production at 13 TeV proton-proton collisions is

about twice that of Run 1 (7 and 8 TeV), the number of beauty particles available for physics analysis is four times higher in the Run 2 data than in Run 1.

The two proton beams are made to collide at four points around the LHC ring where each of the four major LHC experiments are located. ATLAS (A Toroidal LHC Apparatus) and CMS (Compact Muon Solenoid) are the two independent, general-purpose detectors with wide-ranging physics programs, including Higgs, top, and electroweak physics, but also direct searches for beyond-SM physics, such as extra dimensions and dark-matter particles. ALICE (A Large Ion Collider Experiment) is dedicated to strongly-interacting matter at extreme energy densities, where a phase of matter called quark-gluon plasma is formed after heavy-ion collisions. At last, the LHCb experiment is focused on the study of decays of heavy-flavoured hadrons and the search for indirect evidence of non-SM physics via precision measurements of observables such as  $CP$  asymmetries, angular observables, and unitarity-triangle parameters.

## 2.2 The LHCb Detector

In the quest for evidence of  $CP$  violation in the beauty sector, the  $B$  factories BaBar [74] and Belle [75] were the protagonists for many years. The LHCb experiment entered the game with the start of the LHC, and for the last 5 years, has assumed the lead in the experimental field of  $CP$  violation.

The Large Hadron Collider beauty (LHCb) detector is a single-arm forward spectrometer specifically designed for the study of hadrons containing  $b$  or  $c$  quarks. To this intent, it is composed of a set of subdetectors that generally fall into one of two classifications: tracking or particle identification detectors. The LHCb adopts a right-handed Cartesian coordinate system, whose origin is located at the nominal interaction point, the positive  $z$ -axis points along the beampipe, in the direction of the various subdetectors, and the  $y$  axis sits along the vertical. A side-view layout of the detector and its subsystems is shown in Figure 2.3.

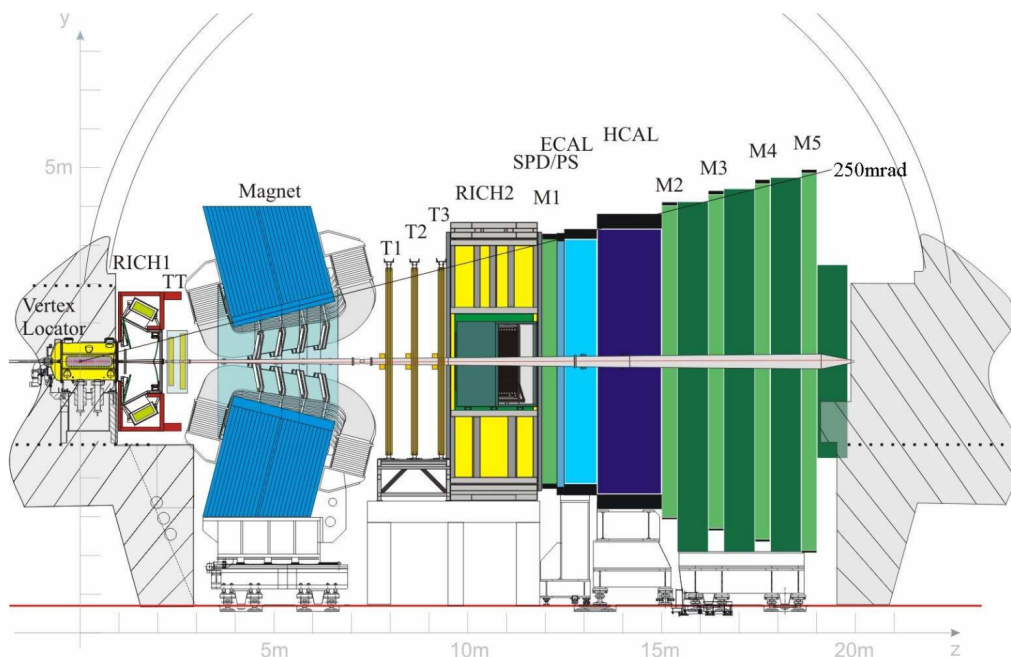


FIGURE 2.3: Schematic side view of the LHCb detector [66].

The geometry of the detector has been chosen to exploit the physics of  $b$ -quark production at the LHC, since at high energies both  $b$ - and  $\bar{b}$ -hadrons are predominantly produced in the same forward or backward cone. The LHCb is the smallest of the four main experiments with dimensions of  $13\text{ m} \times 10\text{ m} \times 21\text{ m}$  allowing an angular coverage of 10 to 300 mrad in the horizontal plane, and from 10 to 250 mrad in the vertical plane. This corresponds to a pseudorapidity range of  $1.6 < \eta < 4.9$ .

Experimentally, pseudorapidity is an easy quantity to measure; all that is required is knowledge of the polar angles of emission of the produced particles,  $\theta$ , as it can be written as

$$\eta = -\ln \left[ \tan \left( \frac{\theta}{2} \right) \right]. \quad (2.2)$$

In hadron collider physics, the pseudorapidity is preferred over the polar angle  $\theta$  because differences in pseudorapidity are Lorentz invariant under boosts along the longitudinal axis. The expected distribution of  $b\bar{b}$  pairs, as a function of the pseudorapidities of the two in the pair, is shown in Figure 2.4; approximately 25% of pairs produced fall within the LHCb detector acceptance.

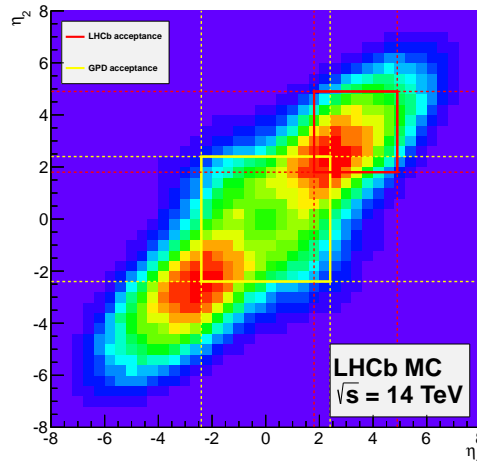


FIGURE 2.4: Pseudorapidity distribution of  $b\bar{b}$  pairs produced in simulated  $pp$  collisions [76]. The central yellow square corresponds to the angular acceptance of ATLAS and CMS, whereas the red square in the top-right quadrant represents the acceptance of the LHCb detector.

The LHCb detector mainly operates at an instantaneous luminosity of the order of  $10^{32}\text{cm}^{-2}\text{s}^{-1}$ , several times lower than the maximum LHC design luminosity. Applying this procedure, known as ‘luminosity levelling’, the probability of a single  $pp$  interaction per bunch crossing is maximised. This feature then succeeds in cutting down the overall number of tracks that must be reconstructed and reducing the amount of radiation damage to the Vertex Locator subdetector.

## 2.3 Tracking

The LHCb tracking system is responsible for the track reconstruction of incoming particles and consists of the Vertex Locator (VELO), a warm dipole magnet, and four planar tracking stations: the first one, the Tracker Turicensis (TT), located upstream of (before) the magnet; and the last three (T1, T2, T3), located downstream of (after)

the magnet. Both VELO and TT use silicon microstrip detectors. In T1-T3, this technology is also employed in the region closest to the beam pipe (Inner Tracker, IT), whereas straw-tubes are applied in the outer region of the stations (Outer Tracker, OT). The TT and the IT were developed in a joint project called the Silicon Tracker (ST).

### 2.3.1 Vertex Locator

The Vertex Locator is the first LHCb subdetector encountered by particles produced in the  $pp$  collision, surrounding the interaction point to obtain precise primary and secondary vertex reconstruction (see Subsection 3.1.1), which is a distinctive feature for  $b$ - and  $c$ -hadron decays. The VELO consists of a series of silicon modules which provide hit information in the  $r$ - and  $\phi$ -coordinates. These pieces of information are essential for the trigger decision and offline analysis. An overview of the VELO layout is seen in Figure 2.5.

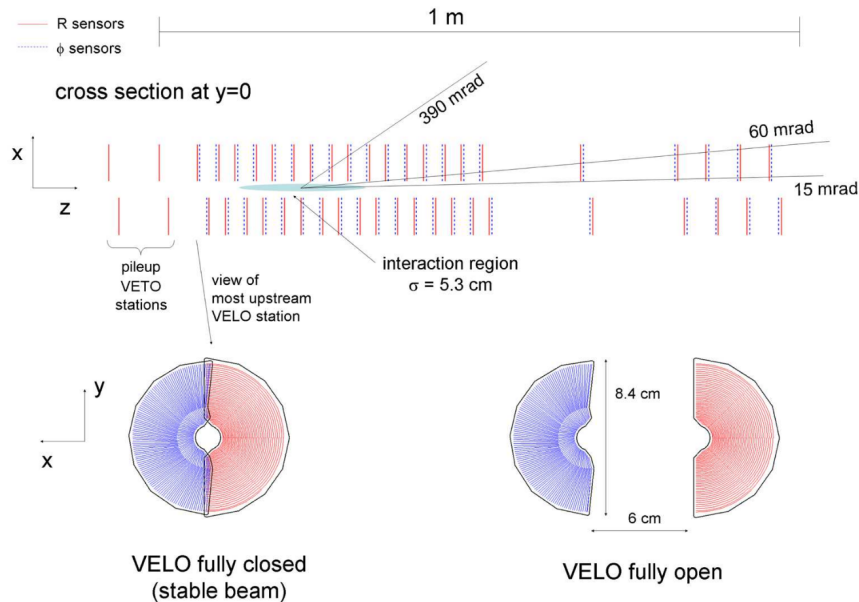


FIGURE 2.5: Arrangement of VELO modules along the beamline (top). Front face of the first module in both the closed and open configurations (bottom) [66].

To achieve its goal, the VELO must be able to gather measurements from the closest possible region to the interaction point: during data-taking conditions the active area of the modules starts at a distance of 8.2 mm away from the beamline. During beam injection and ramping, however, the VELO halves are retracted by a distance of 30 mm in order to allow for beam excursions.

The detectors are mounted in a vessel that maintains a secondary vacuum around the sensors and is separated from the primary machine vacuum by a 300  $\mu\text{m}$  thick walled corrugated aluminium sheet, referred to as RF-foils. A separate vacuum was designed so as to prevent RF (radio frequency) interference induced by the LHC beams and to protect the LHC vacuum from outgassing of the detector modules.

The silicon modules are positioned inside the VELO in such a way that any track within the 300 mrad acceptance must cross at least four modules. This means most

modules populate the region closest to the nominal interaction point, with a minimum distance in the  $z$ -direction between modules of 3.5 cm. To fully cover the acceptance in the azimuthal direction, the two halves must overlap; this is achieved by shifting one VELO half by 1.5 cm in the  $z$ -direction with respect to the other half.

Each of the 21 standard VELO modules is composed of two sensors: the  $R$ -sensor provides information on the radial distance from the beam axis, and the  $\phi$ -sensor provides information on the azimuthal coordinate. There are two additional upstream planes of stations, containing only an  $R$ -sensor each, that collectively form the pile-up veto system. Knowledge of a hit's position along the  $z$ -axis is given by the position of the sensor itself in the LHCb coordinate system.

### 2.3.2 Trackers

The Silicon Tracker consists of two detectors: the Tracker Turicensis (TT) and the Inner Tracker (IT). The Tracker Turicensis is a silicon microstrip detector located between RICH 1 and the LHCb magnet, covering the full acceptance of the detector. The detection mechanism consists of the production of electron-hole pairs in a layer of silicon a few hundreds of micrometers thick. The free electrons are then drifted by an electric field created by a pattern of anodes and cathodes interlaced on the surface of the silicon and separated by a  $\text{SiO}_2$  insulator.

The layout and the TT's physical dimensions are shown in Figure 2.6. The IT covers a smaller cross-shaped region in the centre of the three tracking stations downstream of the magnet and its segmentation and dimensions can be seen in Figure 2.7. Each of the four ST stations has four detection layers in an  $(x-u-v-x)$  arrangement with vertical strips in the first and the last layer and strips rotated by angles of  $-5^\circ$  and  $5^\circ$  in the second and the third layer, respectively.

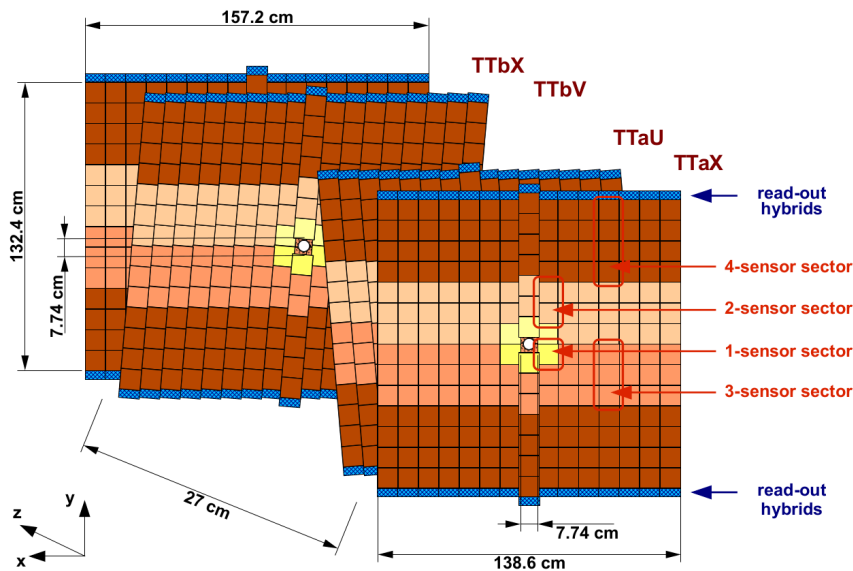


FIGURE 2.6: Layout of the TT. Different readout sectors are indicated by distinct shadings [77].

The purpose of the TT is twofold: it is used to reconstruct the trajectories of low-momentum particles that are swept by the magnet and do not reach the T-stations (T1–T3), and to reconstruct long-lived particles such as  $\Lambda$  and  $K_S^0$ , which decay outside the VELO acceptance. The IT covers the high-occupancy region of the three

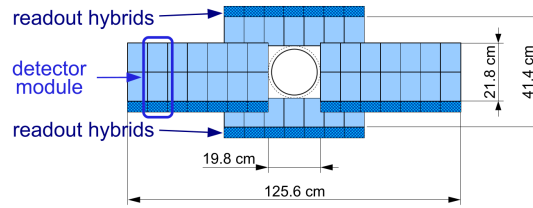


FIGURE 2.7: Layout of an  $x$  detection layer in the second IT station [66].

downstream tracking stations, with silicon trackers arranged in a cross shape around the beam pipe.

The Outer Tracker is a drift-time detector, composed of individual gas-tight straw-tube modules, and it covers most of the acceptance of the three T-stations. In each station, the OT consists of four layers of modules also matching the  $(x-u-v-x)$  formation found in TT and IT. Each module is made up of two rows of straw tubes, as shown in Figure 2.8. Its objective is to track charged particles and to measure their momenta over a large acceptance area.

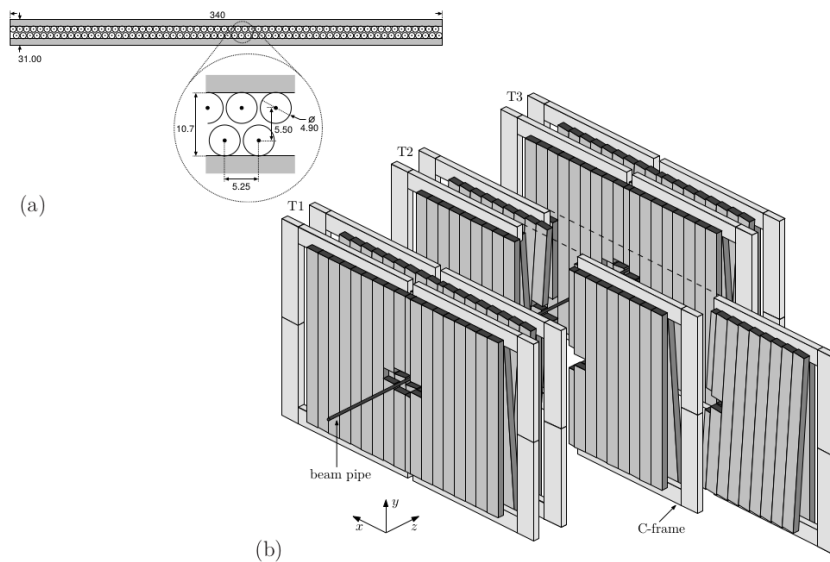


FIGURE 2.8: (a) OT module cross section. (b) Arrangement of OT straw-tube modules in layers and stations [78].

In a drift-time detector, charged particles ionise the gas inside the tubes, with the free electrons then travelling to an anode wire at the centre of the tube. The detection mechanism relies on measuring the drift time of the ionization electrons in the gas to calculate the spatial position of the ionizing particle. The gas mixture chosen is a 70:28.5:1.5 mix of Ar:CO<sub>2</sub>:O<sub>2</sub> [78].

Figure 2.9 shows a layout of all tracking stations in regards of arrangement and scale. ST is shown in purple, whereas OT is depicted in cyan.

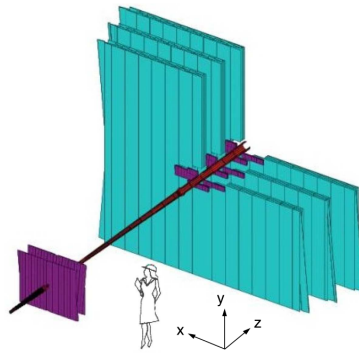


FIGURE 2.9: Arrangement and scale of the tracking stations [66].

### 2.3.3 Magnet

In order to achieve precise momentum measurements of the charged particles travelling through the detector, a well-understood magnetic field is employed to bend their course. A warm dipole magnet is used in LHCb consisting of two conical saddle-shape coils, each composed of fifteen aluminium pancakes, enclosed in an iron yoke, as shown in Figure 2.10. The coils are placed mirror-symmetrically to each other about the  $xz$ -plane, at such positions as to cover full LHCb angular acceptance. The magnetic field generated is parallel to the  $y$ -axis, and the integrated magnetic field delivered over a 10 m track length is 4 Tm.

Since the LHCb magnet deflects positive and negative particles in opposite directions in the  $xz$ -plane, a difference in performance of the left and right sides of the detector leads to charge detection asymmetries. To reach its design sensitivity in  $CP$  violation measurements, LHCb aims to control such detection asymmetries by changing the direction of the magnetic field regularly and then combining data sets with different polarities to cancel left-right asymmetries.

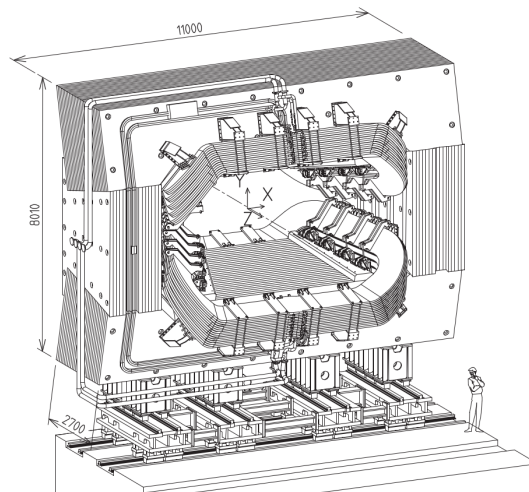


FIGURE 2.10: Schematic view of the dipole magnet (units in mm) [66].

## 2.4 Particle Identification

The majority of decays studied by the LHCb experiment rely on the accurate identification of a small selection of final-state particles, namely, charged hadrons (pions, kaons, protons), muons, electrons, and photons. The LHCb detector employs two Ring Imaging Cherenkov detectors to distinguish between species of charged hadrons; a calorimetry system to measure the energy and identify electrons, photons, and hadrons; and a muon detector system to identify and measure the momentum of muons. The positioning of these subsystems within the detector can be seen in Figure 2.3.

### 2.4.1 Ring Imaging Cherenkov Detectors

The two Ring Imaging Cherenkov (RICH) detectors perform the critical task of identifying pions, kaons, and protons. The decay channels studied in this work are all exclusively composed of pions and kaons in the final state and share the same topology, hence the importance of the information extracted from these subdetectors.

The working principle of RICH relies on the phenomenon of Cherenkov radiation: a charged particle travelling through an optically transparent, dielectric medium at a speed greater than the phase velocity of light in the medium will emit radiation coherently in a cone of angle  $\theta_c$  along the path of the particle. The source of such radiation is the time-dependent polarization of the medium induced by the motion of the particle [79]. The relation between the Cherenkov angle and the particle's speed is given by

$$\cos \theta_c = \frac{c}{nv_p}, \quad (2.3)$$

where  $n$  is the refractive index of the material,  $c$  is the speed of light in vacuum, and  $v_p$  is the speed of the charged particle.

Particle physicists have long exploited Equation 2.3 to measure the speed of charged particles passing through a detector. When combined with an independent measurement of momentum, it is possible for the mass and energy of the particle to be determined. The Cherenkov angles as a function of momentum, for different charged final-state particles in LHCb, can be seen in Figure 2.11.

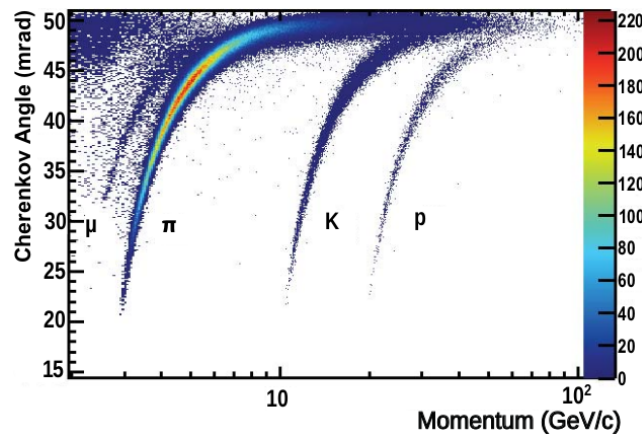


FIGURE 2.11: Reconstructed Cherenkov angle for isolated tracks, as a function of track momentum in the RICH 1  $C_4F_{10}$  radiator [67]. The Cherenkov bands for muons, pions, kaons and protons are clearly visible.

In both RICH detectors, the photons produced in the material are focused onto Hybrid Photon Detectors (HPDs), which are located outside of the detector's acceptance by a combination of flat and spherical mirrors. These HPDs must be shielded from the fringe field of the dipole magnet to protect their performance, and this is accomplished by enclosing them in external iron shields. In the RICH 1, the optical layout is vertical, whereas in RICH 2, it is horizontal as shown in Figure 2.12.

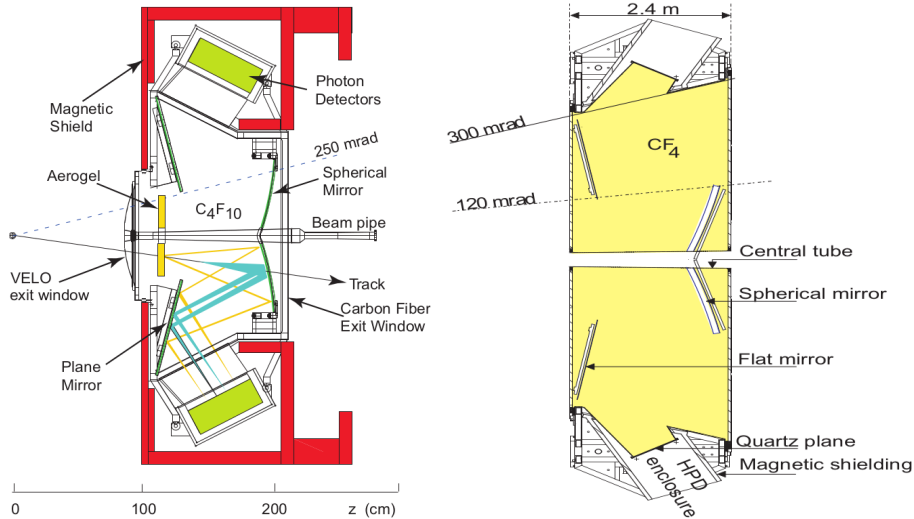


FIGURE 2.12: Side-view schematic layout of the RICH 1 detector (left) and top-view schematic of RICH 2 (right) [66].

RICH 1 is located upstream of the dipole magnet, between VELO and TT, and it covers the full detector acceptance. It was designed to use both decafluorobutane (C<sub>4</sub>F<sub>10</sub>) gas and aerogel as Cherenkov radiators: the C<sub>4</sub>F<sub>10</sub> providing coverage for a higher momentum range, whereas the aerogel covers the lower momentum range. During Run 1, as a result of operating at higher luminosities than designed, the excess of photons produced in the aerogel deteriorated the overall particle identification (PID) in RICH 1. A decision was then made to remove the aerogel for the start of Run 2, which resulted in a speed-up in the RICH reconstruction with no loss of PID performance [80].

RICH 2 is located downstream the magnet, between the tracking stations and the calorimetry system, covering a reduced acceptance range: 15-120 mrad horizontally and 15-100 mrad vertically. It is designed to cover a higher momentum range than RICH 1, which validates its reduced acceptance, since low-momentum particles are swept away by the magnet. The radiator material chosen was tetrafluoromethane (CF<sub>4</sub>) gas.

### 2.4.2 Calorimeters

The calorimetry system performs distinct roles: it selects transverse energy hadron, electron and photon candidates for the first trigger level (L0); it provides identification of photons, electrons, and hadrons, as well as the measurement of their energies and positions; and reconstructs with good accuracy  $\pi^0$  and prompt photons, which is crucial for *B*-meson analyses.

It consists of four subdetectors located downstream of RICH 2: a Scintillator Pad Detector (SPD), a Preshower Detector (PS), an Electromagnetic Calorimeter (ECAL),

and a Hadronic Calorimeter (HCAL). As particles travel through the calorimeter material, energy is lost due to interactions and a particle shower is produced. All four subdetectors use scintillator material (doped polystyrene) as their active medium; the scintillation light produced by the showers is then transported to photomultiplier tubes in the perimeter via wavelength-shifting fibres. Layers of absorber material are interlaced with the scintillator in order to contain the showering particles. Also, the hit density decreases by two orders of magnitude from the inner edge of each calorimeter to the outer edge, hence the variable segmentation adopted for each calorimeter subdetector, as shown in Figure 2.13.

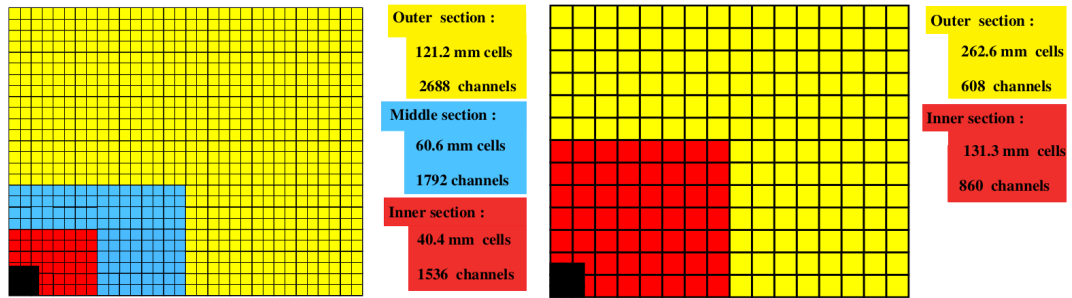


FIGURE 2.13: Lateral segmentation of the SPD/PS and ECAL (left) and the HCAL (right). The upper right quarter of the detector front face is shown. In the left figure the cell dimensions are given for the ECAL [66].

The SPD/PS detectors are two high-granularity rectangular scintillator pads with a 7.6 m-wide and 6.2 m-high sensitive area, and a 15 mm layer of lead absorber between them. They are used in conjunction with the ECAL to provide discrimination between photons, electrons and pions. For example, photons will not interact and create a signal travelling through the SPD but will initiate a shower in the lead absorber layer, generating a signal in the PS. Thus, the presence of a signal in the PS but a lack of one in the SPD identifies the particle as a photon. The thickness of the lead absorber has been optimised to differentiate between electrons and charged hadrons: the radiation length of lead is much shorter than its interaction length, therefore electrons are more likely to start showering in the PS than pions.

The ECAL provides the distinction between electrons and photons and is composed of alternating layers of 2 mm-thick lead and 4 mm-thick scintillator tiles, with a total of 66 layers each. The ECAL forms a 42 cm stack, corresponding to 25 radiation lengths, which is enough to fully contain the electromagnetic showers produced by high-energy photons and electrons. It is designed to achieve an energy resolution of  $\sigma_E/E = 10\% \sqrt{E/\text{GeV}} \oplus 1\%$ , where 10% and 1% represent the stochastic and the constant resolutions, respectively.

The HCAL uses an iron absorber instead of lead, while using scintillator tiles as the active material. Whereas in the ECAL both lead and scintillator layers are arranged transversely, in the HCAL the tiles run parallel to the beam axis. The primary goal of the HCAL is to be used in the hardware trigger, therefore it is not required to fully contain the produced hadronic showers. Due to the limited space available in the LHCb cavern the HCAL has a depth of 1.65 m, corresponding to only 5.6 nuclear interaction lengths in steel. Hadronic showers tend to be larger than electromagnetic ones and so the HCAL is segmented into only two zones, as seen in the right of Figure 2.13. The design energy resolution is  $\sigma_E/E = 69\% \sqrt{E/\text{GeV}} \oplus 0.9\%$ .

### 2.4.3 Muon System

Muon triggering and offline muon identification are fundamental for the LHCb experiment. Muons are encountered in the final states of many  $CP$ -sensitive  $B$  decays, in particular,  $B_d^0 \rightarrow J/\psi (\mu^+ \mu^-) K_S^0$  and  $B_s^0 \rightarrow J/\psi (\mu^+ \mu^-) \phi$ ; and they also perform a major job in  $CP$ -asymmetry and oscillation measurements involving neutral  $B$  mesons. In addition, the study of rare  $B$  decays such as the flavour-changing neutral-current decay,  $B_s^0 \rightarrow \mu^+ \mu^-$ , may reveal new physics beyond the Standard Model. The muon system also provides fast information for the high- $p_T$  muon trigger at the earliest level and muon identification for the high-level trigger and offline analysis.

Muon identification and measurement at LHCb is performed by a system composed of five rectangular stations, M1 to M5. Muons are highly-penetrating particles and, as a result, most of the muon stations (M2–M4) are located at the end of the detector, past the calorimeters, where background from other particles is greatly reduced. These four stations are interleaved with 80 cm-thick iron shielding plates to further decrease background. The first muon station, M1, is positioned upstream of the calorimetry system to improve the  $p_T$  measurement used in the hardware trigger. A layout of the muon system and its subdetectors is depicted in Figure 2.14.

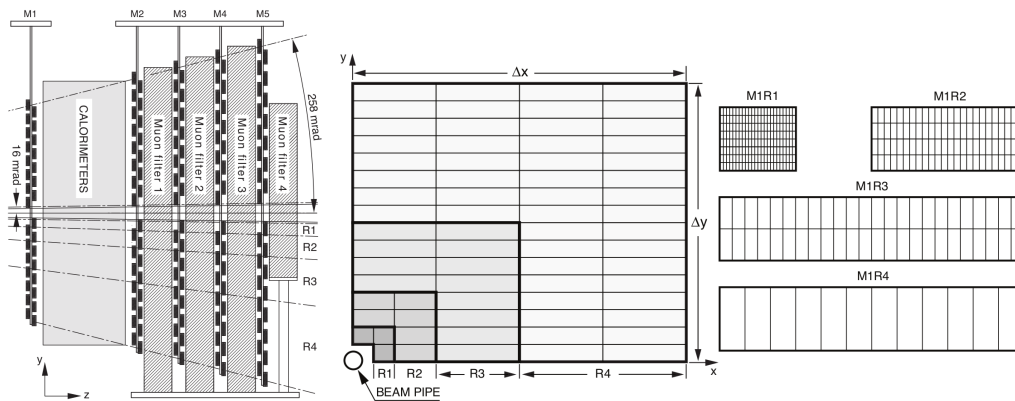


FIGURE 2.14: Side view of the muon system (right). Front view of a quadrant of a muon station, where each rectangle represents one chamber (middle). Division into logical pads of four chambers belonging to the four regions of station M1 (left). [66]

M1–M3 are more granular than M4–M5 and are used to determine the muon track direction, providing a  $p_T$  resolution of 20% in the bending plane. M4 and M5 have limited spatial resolution and are used to identify penetrating particles. The minimum momentum required for a muon to cross the five stations is  $6 \text{ GeV}/c$ . Each station is divided into four concentric regions (R1–R4) to guarantee that the occupancy remains roughly constant between regions.

The muon system, exception for the inner region in M1, is composed of Multi-Wire Proportional Counters (MWPCs). In M1R1, where the particle flux is highest, triple-Gas Electron Multipliers (GEM) are used instead. Both detectors are filled with a gaseous mixture of Ar,  $\text{CO}_2$  and  $\text{CF}_4$  with different proportions to optimize the charge collection. The working principle of such detectors is based on the excitation of the gas molecules by the ionizing particles. The electrons are guided by a very strong electric field close to the anode wires and generate an electron avalanche, leading to a readable electric signal.

Regarding the system performance, a muon detection efficiency well above the design requirement of 99% in all the 5 muon stations is achievable [81].

## 2.5 Trigger

An interaction is defined to be visible if it produces at least two charged particles with sufficient hits in the VELO and T1–T3 to allow them to be reconstructible. The nominal LHC collision rate of 40 MHz translates to an effective frequency of visible interactions at LHCb of about 10 MHz, due to bunch structure and low luminosity as well as accounting for the fraction of  $pp$  collisions that are inelastic. This 10 MHz rate, however is still orders of magnitude higher than what can be stored for physics analysis, which corresponds to a few kHz. A trigger system is therefore crucial to reduce the event rate, while ensuring that events of interest are kept.

The current LHCb trigger system is formed of a hardware level-0 (L0) stage, and two software High-Level Trigger stages (HLT1, HLT2). An overview of the LHCb trigger and the differences in its running between Run 1 and Run 2 are shown in Figure 2.15. The output rate of the LHCb trigger was 3 kHz in 2011, 5 kHz in 2012, and 12.5 kHz in Run 2.

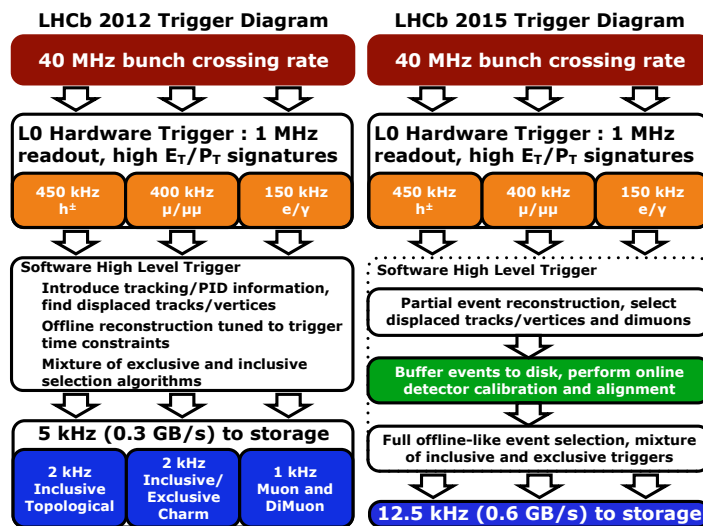


FIGURE 2.15: Overview of the LHCb trigger in Run 1 (left) and Run 2 (right) [82].

The L0 trigger is implemented with the use of custom electronics, which operate synchronously with the 40 MHz bunch-crossing frequency. Its decisions are based on information from the calorimeter and muon systems and are used to reduce the event rate to 1 MHz, the point at which the full detector can be read out. Due to their large mass,  $B$  mesons decays often produce particles with large transverse momentum ( $p_T$ ) and energy ( $E_T$ ), with respect to the beam axis, respectively. The L0 trigger aims to reconstruct: the highest- $E_T$  hadron, electron and photon clusters in the calorimeters and the two highest- $p_T$  muons in the muon chambers. In addition, a pile-up system in the VELO estimates the number of primary  $pp$  interactions in each bunch crossing. The calorimeters calculate the total observed energy and estimate the number of tracks, based on the number of hits in the SPD.

Afterwards, events accepted by the L0 are transferred to a computer system called the Event Filter Farm (EFF), consisting of roughly 1000 nodes during the Run

1 period with an extra 800 nodes added for Run 2. The EFF can run  $\mathcal{O}(10^4)$  instances of the HLT algorithm in parallel.

At the first software stage, HLT1, partial event reconstruction is performed to reduce the output rate to few tens of kHz. Tracks are reconstructed in the VELO and are used to identify primary vertices. Tracks with a high impact parameter are favoured due to the relatively long lifetime of  $B$  mesons. The VELO tracks are then extrapolated to the TT and to the T-stations. The impact parameter and  $p_T$  of tracks are then calculated; the inclusive  $b$ -hadron trigger line selects events containing at least one track with high  $p_T$  and sufficiently displaced from any primary vertex.

HLT2 performs full event reconstruction on all events passing HLT1. The lower input rate allows the trigger selection to be more flexible than the two previous stages. Two types of “trigger line” are defined at this level: inclusive and exclusive. Exclusive trigger lines are optimised to provide the highest possible efficiency for fully-reconstructed  $B$  decays of interest, using all available information, including the mass and vertex quality and separation for the  $B$  candidate and the intermediate resonances, whereas inclusive lines aim to collect decays of resonances which are useful for calibration and likely to have been produced in a  $B$  decay.



## Chapter 3

# $B^\pm$ Candidate Selection

Basically, the procedure to obtain the  $CP$  asymmetry of  $B^\pm \rightarrow h^\pm h^+ h^-$  decays consists of counting the number of  $B^+$  and  $B^-$  candidates in the data samples. The rough data set coming from the detector must then go through a handful of refinement steps before the signal yields can be extracted in the analysis. Distinct aspects related to decay topology and kinematics are taken into account through all selection stages. For each candidate corresponding to a true  $B^\pm \rightarrow h^\pm h^+ h^-$  decay there are many others that approximate their signature, originating from a number of background sources. The different origins of background considered in this analysis, and the strategies and tools employed to optimise their reduction, are described in this chapter.

### 3.1 Introduction

#### 3.1.1 Selection Variables

The selection stages essentially correspond to applying a ‘cut’, namely a threshold value, to a variable and accepting all the events that pass such requirement. The variables used for the selection requirements are mainly based on the topological features of three-body  $B$  meson decays. An illustration of the  $B^\pm \rightarrow h^\pm h^+ h^-$  topology is shown in Figure 3.1. The main variables that concern the current analysis are described hereafter.

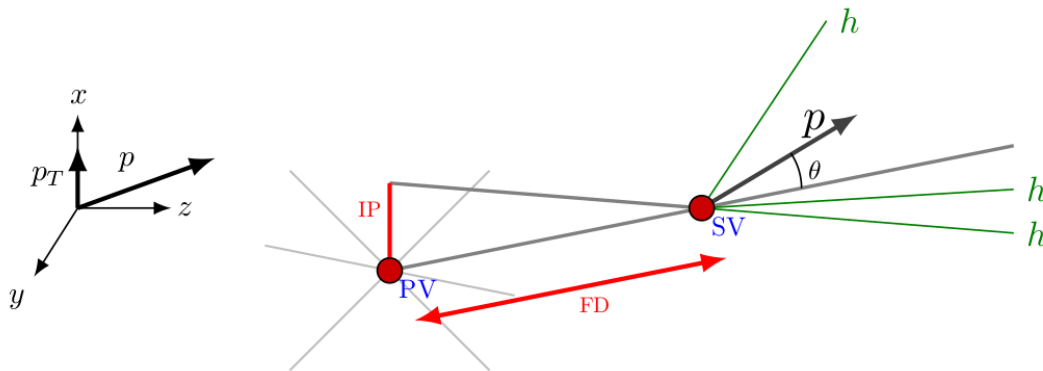


FIGURE 3.1: Schematic view of the topology of a three-body decay.

#### PV, SV and FD

The  $pp$  interaction point, which generates several other particles beyond the  $b\bar{b}$  pair, is named the primary vertex (PV). One of the  $b$  quarks quickly hadronises into a  $B$

meson and travels through a flight distance (FD) before decaying. The spatial point of the  $B$ -meson decay into its daughter particles is referred as secondary vertex (SV).

As reported in Section 1.4, a  $B^\pm$  meson has a mean lifetime of about 1.64 ps and can be considered a relatively long-lived particle. Hence, a typical  $B^\pm$  signature has a displaced vertex with respect to the primary vertex.

## IP

In the framework of high-energy physics, the track's impact parameter measures the transverse distance of the closest approach between the reconstructed track and a vertex, which is usually the primary vertex. Commonly, the final states from a  $B$  meson have a larger impact parameter than a particle produced at the primary vertex.

## IP $\chi^2$ and FD $\chi^2$

The IP significance ( $\chi_{\text{IP}}^2$ ) corresponds to the increase in the vertex-fit  $\chi^2$  when including the track considered, whereas the FD significance ( $\chi_{\text{FD}}^2$ ) represents the ratio between the flight distance squared and the square of combined uncertainties of the primary and secondary vertex positions, which might show a better separation between signal and background.

## SV $\chi^2$

A good quality of the secondary vertex is required by imposing that the three daughter tracks form a good vertex.

## Track $\chi^2/\text{ndf}$

The  $\chi^2$  divided by the number of degrees of freedom of the track fit constitutes a measure of track-reconstruction quality. A good reconstructed track is translated in  $\chi^2/\text{ndf} \sim \mathcal{O}(1)$ .

## $p_T$ and $E_T$

The transverse momentum is the projection of the momentum vector onto the plane perpendicular to the beam axis. Transverse energy may sound as a misleading term, since energy is a scalar quantity, however it corresponds to the energy measured in the calorimeters that is converted into a transverse momentum measurement. A typical signature of a  $B^\pm$  decay has a very high transverse momentum/energy.

## $\cos \theta$

The angle  $\theta$  corresponds to the angle between the  $B$ -meson track and the daughter particle's momentum direction. The cosine of this angle should be very close to 1 for a true  $B^\pm$  candidate.

## DOCA

The distance of closest approach (DOCA) corresponds to the minimum distance between a pair of daughter tracks. In the case of a decay with three final-state particles, these distances are computed from the three possible pairs of tracks. It can be used

to reject particles which are not coming from the same vertex. Usually, the cut is applied to the maximum or minimum DOCA.

### Invariant mass

From four-momentum conservation, the  $B^\pm$  invariant mass is calculated using  $p_B^\mu = p_1^\mu + p_2^\mu + p_3^\mu$  where the left-hand side represents the  $B$ -meson four-momentum, while the right-hand side, the four-momenta of the decay products. The invariant mass of the combination of three  $h$  candidates to reconstruct the mass of a  $B^\pm$  candidate is given by

$$m(hhh) = \sqrt{(p_1^\mu + p_2^\mu + p_3^\mu)^2} = \sqrt{E^2 - \mathbf{p}^2} \quad (3.1)$$

### Particle identification variables

The particle identification (PID) information obtained from the calorimeters, RICH and muon system, as discussed in Section 2.4, are combined to provide a single set of PID variables. The LHCb uses PID variables extensively as selection criteria in the analyses to discriminate pions, kaons, protons, electrons, and muons. In this analysis, the PID variable type used was ProbNN. This quantity is the output of multivariate techniques created by combining tracking and PID information such as the tracking performance and kinematics. This results in a single probability value, *i.e.*, they go from 0 to 1, for each particle hypothesis.

#### 3.1.2 Selection Stages

The selection of  $B^\pm \rightarrow h^\pm h^+ h^-$  signal candidates happens along distinct stages. It begins with a pre-selection which is based mostly on track-quality variables and thus performs very efficiently in removing candidates with low track-reconstruction quality. This stage, further detailed in Section 3.4, can be distributed in three smaller steps. The first one consists of trigger-line choices that pick interesting events from the  $pp$  collision. It is followed by a broader pre-selection, named stripping, which is a common selection for many  $B$  decays with three hadrons in the final states that can be used in different analyses. Finally, a set of loose PID requirements specific for each channel is performed in order to reduce the physical background sources. These background contributions are covered in Section 3.3.

After these preliminary steps, a final selection, as later discussed in Section 3.5, aims on reducing two prominent background contributions that affect the separation of each  $B^\pm \rightarrow h^\pm h^+ h^-$  decays as much as possible: combinatorial and peaking backgrounds. The combinatorial background originates from random combinations of tracks faking the signal, and to reduce its contamination, selection cuts based on a multivariate analysis technique are used. The peaking background mostly comes from  $B$  decays whose final-state particles are misidentified and populate the signal region: dedicated particle-identification criteria are employed. Lastly, to filter out the intermediate charmed contributions, invariant-mass vetoes are applied.

## 3.2 Data and Simulation

This analysis uses a data sample that consists of events collected by the LHCb during Run 2 (2015-2018) when, as mentioned in Section 2.1, the LHC produced  $pp$  collisions at a centre-of-mass energy of 13 TeV and an integrated luminosity of  $5.9 \text{ fb}^{-1}$  was

recorded. The luminosity recorded per year (Figure 2.2) corresponds to  $0.33 \text{ fb}^{-1}$  for 2015,  $1.67 \text{ fb}^{-1}$  for 2016,  $1.71 \text{ fb}^{-1}$  for 2017 and  $2.19 \text{ fb}^{-1}$  for 2018.

The simulation of  $pp$  interactions was produced by PYTHIA 8 with specific LHCb data-taking conditions. These signal and background  $B^\pm \rightarrow h^\pm h^+ h^-$  event samples were generated through the Monte Carlo (MC) method with a flat Dalitz plot representation, *i.e.*, with no resonant decays and no  $CP$  violation. Two sizes of MC samples were used: a ‘small’ MC sample and a ‘large’ MC sample. The small ones were adopted for background estimation, particle identification requirements and to define cuts based on multivariate analysis study. Their sizes are summarised in Table 3.1. The large MC samples were applied to study the acceptance effects after selection cuts. These samples are yet separated by year of data taking – samples for 2017 and 2018 were not available until the time of analysis – and by magnet polarity (MagUp and MagDown).

Decay	Magnet Polarity	2015	2016
$B^\pm \rightarrow K^\pm K^+ K^-$	MagDown	257787	504110
	MagUp	250485	514017
$B^\pm \rightarrow \pi^\pm K^+ K^-$	MagDown	257693	500810
	MagUp	250811	500269
$B^\pm \rightarrow K^\pm \pi^+ \pi^-$	MagDown	250231	500222
	MagUp	255345	500123
$B^\pm \rightarrow \pi^\pm \pi^+ \pi^-$	MagDown	251197	605977
	MagUp	257717	500831

TABLE 3.1: Signal statistics for the small MC samples.

### 3.3 Background Sources

The central purpose of the selection cuts is to discriminate signal from background. Thus, a thorough understanding of the background sources can reveal adequate selection cuts to improve signal purity.

First, it is important to note that the most common decays  $B$  involve charmed mesons as intermediate states because the  $b \rightarrow c$  transition is more frequent than  $b \rightarrow u(d)$ . Therefore, charmed decays represent a crucial background contribution for  $B^\pm \rightarrow h^\pm h^+ h^-$ . In this mass spectrum, charmed background can be either due to an intermediate charm decay or a misidentified charmonium state:  $B^\pm \rightarrow \bar{D}^0 h^\pm$  and  $B^\pm \rightarrow J/\psi K^\pm$ , respectively.

The branching fraction of  $B^\pm \rightarrow J/\psi K^\pm$  makes it a significant background. Topologically,  $B^\pm \rightarrow J/\psi K^\pm$  (with  $J/\psi \rightarrow \mu^+ \mu^-$ ) has comparable properties with the signal. Since the mass difference between  $\pi$  ( $140 \text{ MeV}/c^2$ ) and  $\mu$  ( $106 \text{ MeV}/c^2$ ) is small, this kind of background will occupy the same mass range as the signal. To eliminate the contamination from when muons are misidentified as pions, it is required for hadron tracks not to be muons through a variable for muon identification called `isMuon`.

The other type of fully-reconstructed charmed modes consists of  $B^\pm \rightarrow \bar{D}^0 h^\pm$  decays. Since the  $\bar{D}^0$  meson decays into  $KK$ ,  $\pi\pi$  or  $K\pi$ , the distribution of charmed candidates with the same final-state particles as a signal channel will also peak directly underneath the signal peak.

The most effective approach for removing charmed candidates is an explicit veto on the two-body invariant mass region around  $J/\psi$  and  $\bar{D}^0$  peaks, as described in Subsection 3.5.3.

That being said, distinct types of background are observed in the  $B^\pm \rightarrow h^\pm h^+ h^-$  invariant-mass spectrum and the ones considered can be roughly divided into the following classes:

- Combinatorial background;
- Peaking background;
- Partially-reconstructed background.

### 3.3.1 Combinatorial background

Random combinations of tracks converging to a vertex in an event can happen to form candidates that approximate signal properties well enough to pass the selection criteria. These candidates do not peak at any particular mass value but instead the three-body high-mass sideband (above  $5.4 \text{ GeV}/c^2$ ) is expected to be dominated by combinatorial events which follow a generally monotonic decreasing distribution.

This type of background is highly reduced through multivariate analysis selection and a description of this method and the optimisation of its output is given in Subsection 3.5.1.

### 3.3.2 Peaking background

Fully-reconstructed decays with the same final-state particles as the signal or decays where one or more pions (kaons) are misidentified as kaons (pions) generally form peaks in the signal region of the invariant-mass spectrum, as shown in Figure 3.2. In other words, they play the role of ‘cross-feed’ background to one another.

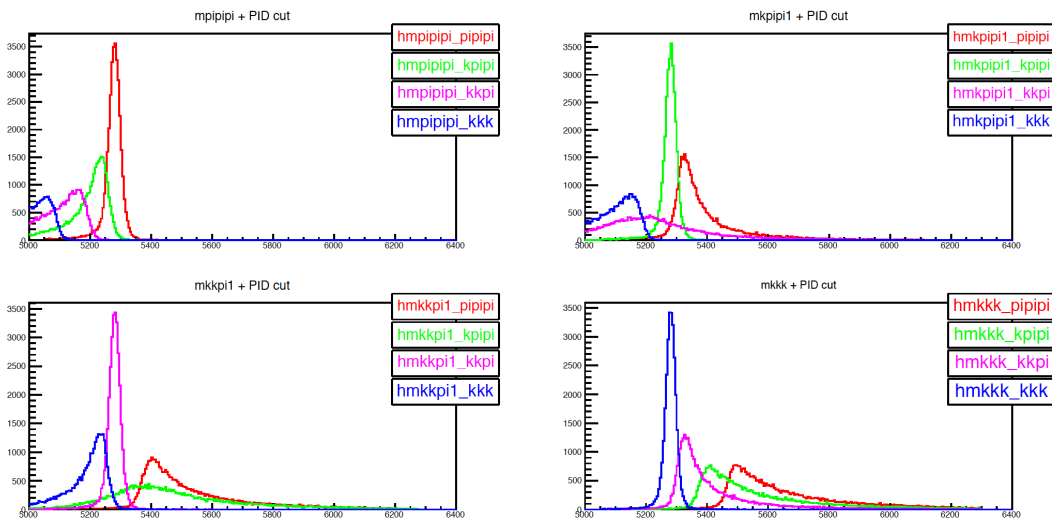


FIGURE 3.2: Simulated distributions of cross-feed background for each  $B^\pm \rightarrow h^\pm h^+ h^-$  channel. The cross-feed shapes are approximate and only illustrative, since they are obtained before the final PID selection. Mass spectrum legend:  $B^\pm \rightarrow \pi^\pm \pi^+ \pi^-$  (top left),  $B^\pm \rightarrow K^\pm \pi^+ \pi^-$  (top right),  $B^\pm \rightarrow \pi^\pm K^+ K^-$  (bottom left) and  $B^\pm \rightarrow K^\pm K^+ K^-$  (bottom right).

The primary effect of the misidentification on the invariant-mass distribution of cross-feed candidates is to shift it by an amount approximately proportional to the mass difference between the correctly-identified and misidentified particle species and the number of misidentified particles. The cross-feed distribution is shifted towards higher mass values in cases where the particle is misidentified as a higher-mass particle, *e.g.*,  $\pi \rightarrow K$ , and towards low masses in the opposite case, *i.e.*,  $K \rightarrow \pi$ . It is also expected that double misidentification is more suppressed than single ones.

Cross-feed background can be very effectively reduced with the use of PID variables, constructed out of information from the LHCb PID system described in Section 2.4. The strategy for optimising the PID selection is detailed in Subsection 3.5.2.

### 3.3.3 Partially-reconstructed background

Partially-reconstructed backgrounds originate from four-body decays with three final-state particles in common with the signal modes, in which the fourth final-state particle has not been included in the event.

The overall shape of each partially-reconstructed background depends on the kinematics of the missing particle; however, a universal feature of such backgrounds is a maximum bound on the three-body invariant-mass distribution, given by the mass difference between the parent particle and the missing particle, *e.g.*,  $m_B - m_{\text{miss}}$ . Background channels originating from  $B^\pm$ ,  $B^0$ , or  $B_s^0$  will therefore populate the low-mass region in the vicinity of the signal peak, with decay channels where the missing particle is a pion or a photon being of most concern.

These backgrounds can be roughly categorised as a function of the masses of the parent particle and the missing particle, and the topology of the decay. The ( $B^\pm$ ,  $B^0$ ) mass difference is negligible and, in this context, so is the difference in ( $\pi^\pm$ ,  $\pi^0$ ) masses. Therefore it is reasonable to group these together under a generic  $B \rightarrow 4$ -body category. The mass difference between ( $B^\pm$ ,  $B^0$ ) and the  $B_s^0$  is large enough to identify  $B_s^0 \rightarrow 4$ -body decays as a separate category. Also, the distribution of partially-reconstructed decays containing an intermediate charm particle is assumed to not differ sufficiently from that of charmless decays to justify their inclusion as a separate category. Finally, decays with a missing photon form a distinct category since the mass threshold extends to the mass of the parent particle.

The most relevant contributions for each of the decays will be discussed next.

- Background contributions of  $B^\pm \rightarrow K^\pm \pi^+ \pi^-$ 
  - Charmed decays:  $B^+ \rightarrow (\bar{D}^0 \rightarrow K^\pm \pi^\mp \pi^0) \pi^+$ , where the  $\bar{D}^0$  meson decays to three particles and the  $\pi^0$  is not reconstructed.
  - Charmless decays:  $B^\pm \rightarrow K^{*\pm} \pi^+ \pi^-$ , where the vector meson  $K^{*\pm}$  decays into a  $K^\pm \pi^0$  final state and the  $\pi^0$  is not reconstructed. Also there is the  $B^\pm \rightarrow \eta' K^\pm$  decay, where the  $\eta'$  decays into  $\rho^0(\pi^+ \pi^-) \gamma$  and the photon is not reconstructed. Table 3.2 indicates the branching fractions of these background contributions.
- Background contributions of  $B^\pm \rightarrow K^\pm K^+ K^-$ 
  - Charmless decays:  $B^\pm \rightarrow K^{*\pm} K^+ K^-$ , where the  $K^{*\pm} \rightarrow K^\pm \pi^0$  is the main contribution. There is also the  $B^\pm \rightarrow K^{*\pm}(K^\pm \pi^0) \phi(K^+ K^-)$  decay. Table 3.3 shows the branching fractions of these background contributions.
- Background contributions of  $B^\pm \rightarrow \pi^\pm \pi^+ \pi^-$

- Charmed decays:  $B^\pm \rightarrow \bar{D}^0(D^0)\pi^+\pi^-$ , where the  $D^0$  decays to  $\pi^+\pi^-\pi^0$  and the  $\pi^0$  is not reconstructed.
- Charmless decays:  $B^\pm \rightarrow \pi^\pm\pi^+\pi^-\pi^0$ , where the  $\pi^0$  track is not reconstructed. Table 3.4 shows the branching fractions of these background contributions.
- Background contributions of  $B^\pm \rightarrow \pi^\pm K^+ K^-$ 
  - Charmed decays:  $B_s^0 \rightarrow D_s^-(K^+K^-\pi^-)\pi^+$  and  $B^0 \rightarrow D^-(K^+K^-\pi^-)\pi^+$ , where a charged pion is not reconstructed and also  $B^\pm \rightarrow D^0(K^+K^-\pi^0)\pi^\pm$ , where  $\pi^0$  is missing in the reconstruction.
  - Charmless decays:  $B^\pm \rightarrow K^{*\pm}(K^\pm\pi^0)\pi^\pm K^\mp$ , where a charged pion and a  $\pi^0$  are not reconstructed and also  $B^0 \rightarrow K^+K^-\pi^+\pi^-$ , where a charged pion is missing in the reconstruction. Table 3.5 indicates the branching fractions of these background contributions.

Description	Decay	BF
Charmed	$B^+ \rightarrow \bar{D}^0\pi^\pm$ with $\bar{D}^0 \rightarrow K^\pm\pi^\mp\pi^0$	$6.9 \times 10^{-4}$
Charmless	$B^\pm \rightarrow K^{*\pm}\pi^+\pi^-$ with $K^{*\pm} \rightarrow K^\pm\pi^0$	$2.5 \times 10^{-5}$
Resonant radiative	$B^\pm \rightarrow \eta'K^\pm$ with $\eta' \rightarrow \rho^0(\pi^+\pi^-)\gamma$	$2.1 \times 10^{-5}$

TABLE 3.2: Partially-reconstructed background contributions to the  $B^\pm \rightarrow K^\pm\pi^+\pi^-$  decay [40].

Description	Decay	BF
Charmless	$B^\pm \rightarrow (K^{*\pm} \rightarrow K^\pm\pi^0)K^+K^-$	$1.2 \times 10^{-5}$
	$B^\pm \rightarrow \phi(K^+K^-)K^{*\pm}(K^\pm\pi^0)$	$1.6 \times 10^{-6}$

TABLE 3.3: Partially-reconstructed background contributions to the  $B^\pm \rightarrow K^\pm K^+ K^-$  decay [40].

Description	Decay	BF
Charmed	$B^+ \rightarrow (\bar{D}^0 \rightarrow \pi^+\pi^-\pi^0)\pi^+$	$7.1 \times 10^{-5}$
Charmless	$B^\pm \rightarrow \pi^\pm\pi^+\pi^-\pi^0$	$< 4.0 \times 10^{-3}$

TABLE 3.4: Partially-reconstructed background contributions to the  $B^\pm \rightarrow \pi^\pm\pi^+\pi^-$  decay [40].

Description	Decay	BF
Charmed	$B_s^0 \rightarrow (D_s^- \rightarrow K^+ K^- \pi^-) \pi^+$	$4.2 \times 10^{-5}$
	$B^\pm \rightarrow (\bar{D}^0 \rightarrow K^+ K^- \pi^0) \pi^\pm$	$1.6 \times 10^{-5}$
	$B^0 \rightarrow (D^- \rightarrow K^+ K^- \pi^-) \pi^+$	$2.5 \times 10^{-5}$
Charmless	$B^\pm \rightarrow (K^{*\pm} \rightarrow K^\pm \pi^0) \pi^\pm K^\mp$	$< 3.4 \times 10^{-5}$
	$B^\pm \rightarrow (K^{*\pm} \rightarrow K^\pm \pi^0) \pi^\mp K^\pm$	$< 2.0 \times 10^{-6}$
	$B^\pm \rightarrow K^+ K^- \pi^+ \pi^-$	$< 7.2 \times 10^{-5}$

TABLE 3.5: Partially-reconstructed background contributions to the  $B^\pm \rightarrow \pi^\pm K^+ K^-$  decay [40].

## 3.4 Pre-Selection

Prior to the optimisation, a few general selection cuts are applied to all signal candidates to guarantee that good-quality, relevant events are selected. The fundamental goal at this stage is to select events with well-reconstructed tracks and vertices, that are likely to contain a  $B$  meson that decays hadronically.

### 3.4.1 Trigger Selection

As described in Section 2.5, the LHCb trigger system plays the role in making data storage possible for the offline analysis by reducing the data set and keeping only interesting events. Post reconstruction, tracks can be associated with the energy deposits that have caused the L0 trigger to fire; thus, particles are identified and can be classified under the particular L0 trigger fired. If the track that fired the trigger originates from the signal candidate, the event is classified as ‘trigger on signal’ (TOS). Otherwise, if the trigger decision originates from the rest of the event, it is classified as ‘trigger independent of signal’ (TIS). The requirements imposed in this analysis are that signal candidates have fired the L0 hadron trigger, TOS, or that any L0 trigger is fired by the rest of the event, TIS.

At the HLT1 level, signal candidates must pass an inclusive beauty and charm trigger line that requires one good-quality, high- $p_T$  track that is significantly displaced from the primary vertex. Now, at the HLT2 level, the  $B$  candidate is required to pass either the 2, 3 or 4-body topological trigger, which uses a multivariate selection algorithm. The algorithm, for a three-body decay, first combines a two-body candidate to another particle, instead of directly defining a three-body object. This procedure is beneficial since it enhances the efficiency of the HLT2 topological lines. By considering the trigger candidate only contains a subset of the final-state particles, it is not appropriate to perform a selection on the mass of  $B$  candidate. For this reason, a corrected mass variable was defined:

$$m_{\text{cor}} = \sqrt{m^2 + |p_{T,\text{miss}}|^2 + |p_{T,\text{miss}}|}, \quad (3.2)$$

where  $p_{T,\text{miss}}$  is the missing transverse momentum to the direction of flight of the  $B$  candidate. Essentially,  $m_{\text{cor}}$  is the minimum correction to the  $B$ -candidate mass if a daughter is missing.

### 3.4.2 Stripping Requirements

The total data set available from the output of the trigger system is still too large to be analysed efficiently by every LHCb member working on physics analyses. This problem is overcome by running centrally a number of user-defined sets of loose selection criteria, known as ‘stripping lines’. The output of similar stripping lines are gathered into ‘streams’, such that events shared between lines in a particular stream are only stored once.

The stripping line used in this analysis is intended to comprise all four charmless three-body  $B$  decays due to their topological similarities. A summary of the cuts applied at this level is given in Table 3.6: only information related to the signal candidate and some select information about the event as a whole is saved in this stream, reducing storage requirements.

Category	Selection criterion
$hhh$ tracks	$p_T > 0.1 \text{ GeV}/c$
	$p > 1.5 \text{ GeV}/c$
	$\chi_{\text{IP}}^2 > 1$
	$\chi^2/\text{ndf} < 3$
	GhostProb $< 0.5$
	Lead $p_T > 1.5 \text{ GeV}/c$
	$\text{DOCA}_{\text{max}} < 0.2 \text{ mm}$
	$5.05 < m(\text{KKK}) < 6.30 \text{ GeV}/c^2$
	$4 < m_{\text{cor}}(\text{KKK}) < 7 \text{ GeV}/c^2$
	$\sum p_T > 4.5 \text{ GeV}/c$
$\sum p > 20 \text{ GeV}/c$	
$\sum \chi_{\text{IP}}^2 > 500$	
$B$ tracks	$\chi_{\text{IP}}^2 < 10$
	$p_T > 1 \text{ GeV}/c$
	FD $> 3 \text{ mm}$
	SV $\chi^2 < 12$
	$\cos \theta > 0.99998$
	$\chi_{\text{FD}}^2 > 500$

TABLE 3.6: Inclusive stripping line selection criteria for charmless  $B^\pm \rightarrow h^\pm h^+ h^-$  decays.

At the stripping level, all final-state particles are reconstructed as kaons within a wide three-body invariant-mass window, with the reconstruction of the other mass hypotheses done offline. Consequently, no particle identification requirements are applied at this level. Only very loose cuts on the invariant mass of the  $B$  candidates are applied, allowing the other signal final states to be reconstructed without loss of efficiency.

Tracks are required to have traversed the entire tracking system with some minimum momentum cuts applied. These tracks must be of good quality, defined by a low  $\chi^2$  value resulting from the track-fitting procedure. The probability of the track being made of partial trajectories from more than one charged particle, *i.e.*, the probability of a ‘ghost’ track, must also be low.

Three tracks are combined by demanding that the sum of their four-momenta is loosely in the region of the  $B$  invariant mass. The minimum distance between their

trajectories must also be small, *i.e.*, the three tracks must roughly have the same origin. These two criteria are applied to reduce the number of candidates that undergo the vertex fit. Following this fit, additional cuts are applied to ensure the goodness-of-fit of the  $B$  candidate decay vertex and its separation from the PV with which it is most closely associated. The associated PV is defined as the primary vertex that returns the smallest  $\chi_{\text{IP}}^2$  value for a given  $B$  candidate.

### 3.4.3 Loose PID Requirements

At this stage, the samples have not had any particle identification requirements from final-state particles applied to them and hence contain all combinations of pions and kaons, which leads to a very high cross-feed contribution from other  $B^\pm \rightarrow h^\pm h^+ h^-$  decays (as discussed in Subsection 3.3.2). Moreover, the RICH system has limited particle-identification efficiency for tracks with momenta greater than 100 GeV/ $c$  and pseudorapidities outside the  $1.5 < \eta < 5.5$  range. Consequently, high-momentum tracks end up having large misidentification probabilities, resulting in an even larger cross-feed background.

In order to control this type of background, fiducial cuts limiting the momentum and pseudorapidity of the decay products combined with loose PID requirements are performed. This selection is implemented over the following ProbNN variables:

- ProbNNk: probability value for the particle to be a kaon ( $K$ ).
- ProbNNpi: probability value for the particle to be a pion ( $\pi$ ).

The loose requirements, applied to the four  $B^\pm \rightarrow h^\pm h^+ h^-$  decay modes, demand that kaon and pion candidates have ProbNNk  $> 0.1$  and ProbNNpi  $> 0.1$ , respectively. Additionally, another set of loose PID requirements were included to remove contributions from muons and electrons in all tracks.

## 3.5 Final Selection

After the pre-selection stage,  $B^\pm \rightarrow h^\pm h^+ h^-$  candidates are further refined by being required to satisfy dedicated criteria so as to reduce physical backgrounds. The final selection stage retains signal candidates with high efficiency by using a multivariate analysis and particle identification cuts, rejects charmed contributions by including  $\bar{D}^0$  and  $J/\psi$  vetoes and discards multiple candidates in an event that passed the final selection, since more than one signal  $B$  candidate per event is expected due to the low branching ratios of the decay channels.

### 3.5.1 Multivariate Analysis Selection

The combinatorial background comes from a random combination of tracks that form a fake signal of  $B^\pm \rightarrow h^\pm h^+ h^-$  candidates and uniformly populates the whole  $B$  mass spectrum. Due to its characteristic exponential shape along the spectrum, cuts on variables with high discrimination power between signal and background can be applied to reduce the combinatorial background contribution. The simple approach would be to apply rectangular cuts on these variables, but as a result of the large number of tracks and the correlation between the variables, it is necessary to adopt a more powerful approach to efficiently select signal events.

The Multivariate Analysis (MVA) selection exploits the correlation between variables and combines them to obtain a single discriminant. There are many multivariate analysis methods available and the one adopted was the Boosted Decision Tree (BDT). It is based on machine learning technique, that roughly comprises three steps: ‘training’ on the simulation samples to learn the differences between signal and background, ‘testing’ on independent simulation samples and ‘evaluating’ the output result on data samples.

For the BDT training, the data and simulation samples described in Section 3.2 were used. Ten variables with good discrimination power between signal and background were chosen as input, the same set for the four channels. Before training, the samples pass through trigger and stripping cuts,  $J/\psi$  and  $D^0$  vetoes and loose PID requirements. In the last one, weights from PIDCalib (see Subsection 4.3.2) are applied on the simulation samples instead of applying the PID cuts, since the compatibility of PID variables between data and simulation is not well represented.

The training is performed using the BDT implementation in the TMVA package [83]. Two types of training were performed: one, specific for each mode (‘self’); and another, ‘common’ to all channels. The former refers to an optimisation performed using their own MC samples as signal and the high-mass sideband region of the  $B$  mass spectrum data sample, region where the combinatorial background is predominant, as background. The latter, used for cross-checking purposes only, concerns merging the MC samples from the four channels to use it as signal and the data from the  $B^\pm \rightarrow \pi^\pm \pi^+ \pi^-$  high-mass sideband region as background. Comparable yields for background and signal samples were used.

The optimal cut on the BDT output is obtained by calculating the figure of merit for each channel:

$$\text{FoM}_{\text{MVA}} = \frac{S_{\text{MC}}}{\sqrt{(S+B)_{\text{data}}}}, \quad (3.3)$$

where  $S_{\text{MC}}$  is the number of events taken from the MC signal sample and  $(S+B)_{\text{data}}$  is the number of events in the signal region  $|(m_B - 5284 \text{ MeV}/c^2)| < 40 \text{ MeV}/c^2$  taken from the data sample for a given BDT cut, after applying the final PID requirements.

This FoM approximates the signal significance in a counting experiment. The signal efficiency is obtained through the ratio between MC signal events before and after applying all selection requirement. In order to increase signal efficiency with very small loss in significance, the cuts were in fact chosen a bit before the maxima. Figure 3.3 shows the signal significance and the specific FoM optimisation for each decay channel. Table 3.7 summarizes the cuts obtained for the self BDT optimisation.

Channel	BDT selection cuts
$B^\pm \rightarrow \pi^\pm \pi^+ \pi^-$	$> -0.03$
$B^\pm \rightarrow K^\pm \pi^+ \pi^-$	$> -0.07$
$B^\pm \rightarrow \pi^\pm K^+ K^-$	$> -0.07$
$B^\pm \rightarrow K^\pm K^+ K^-$	$> -0.15$

TABLE 3.7: Cuts on the BDT output variable calculated by the specific optimisation (self) training for each  $B^\pm \rightarrow h^\pm h^+ h^-$  channel.

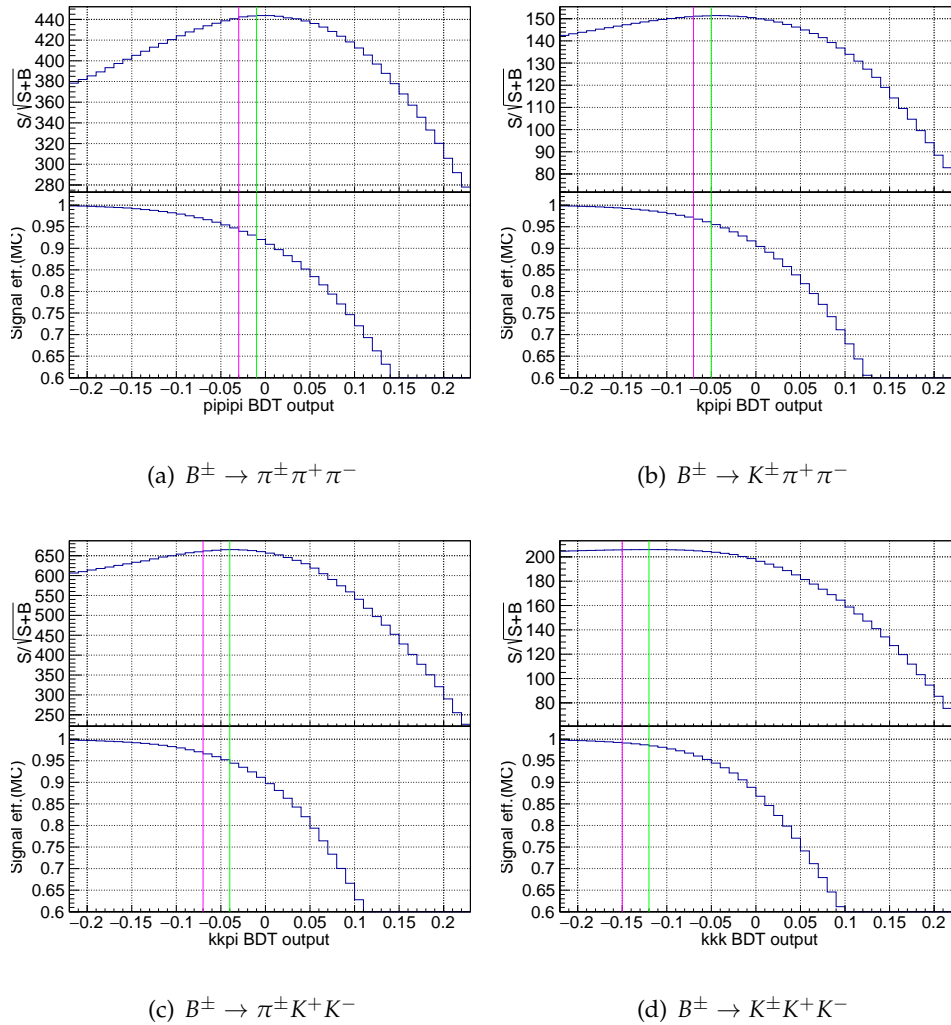


FIGURE 3.3: The figure of merit and the signal efficiency for the self BDT optimisations. The green lines indicate the maximum FoM, whereas the pink ones point out the cut on the chosen BDT output variable.

### 3.5.2 Final PID Selection

The pre-selection stage and the multivariate selection play roles in removing the combinatorial background. Alternatively, the PID selection is aimed at controlling the cross-feed. This background can be drastically reduced, but not eliminated with PID cuts: the signal-selection efficiency rapidly decreases when tight requirements are implemented, so the goal is to achieve a compromise between signal efficiency and background rejection.

The requirements can either be ‘affirmative’ and ‘negative’. The former refers to the probability of a particle being identified as its true type, *e.g.*, a pion candidate being identified as a pion; whereas the latter, to the probability that a particle is not identified as another particle, for instance, a pion candidate not identified as a kaon.

The definition of the final PID requirements is mostly made through  $B^+ \rightarrow \bar{D}^0 h^+$  decays: since the momentum distribution for the products of these decays are similar to those for charmless decays, the requirements are determined by analysing the

evolution of  $\bar{D}^0 \rightarrow h^+h^-$  signals as a function of both positive and negative cuts. Table 3.8 summarises the PID selection criteria that excelled for the four  $B^\pm \rightarrow h^\pm h^+ h^-$  decay channels. In addition to these requirements, a mild  $\text{ProbNN}_e < 0.4$  cut was applied to all tracks in all channels in order to eliminate a residual contamination from  $J/\psi \rightarrow e^+e^-$ , where the electron-positron pair is misidentified as pions or kaons.

Decay	Daughter	PID selection cuts
$B^\pm \rightarrow K^\pm K^+ K^-$	all	$\text{ProbNN}_k > 0.2$
$B^\pm \rightarrow \pi^+ K^\pm \pi^-$	pion kaon	$\text{ProbNN}_{\text{pi}} > 0.25$ & $\text{ProbNN}_k < 0.5$ $\text{ProbNN}_k > 0.2$
$B^\pm \rightarrow K^+ \pi^\pm K^-$	pion kaon	$\text{ProbNN}_{\text{pi}} > 0.7$ & $\text{ProbNN}_k < 0.05$ $d1\_ProbNN_k > 0.4$ & $d3\_ProbNN_k > 0.6$ & $\text{ProbNN}_{\text{pi}} < 0.2$
$B^\pm \rightarrow \pi^\pm \pi^+ \pi^-$	all	$\text{ProbNN}_{\text{pi}} > 0.5$ & $\text{ProbNN}_k < 0.1$

TABLE 3.8: PID selection criteria for  $B^\pm \rightarrow h^\pm h^+ h^-$  decays.

### 3.5.3 Mass Vetoes

As mentioned in Section 3.3, a number of  $B$  decays have a charmed meson as an intermediate state, mostly the  $D$  meson, with the same final states as the signal (also reconstructed with a missing particle). In order to exclude the contributions of  $B^\pm \rightarrow \bar{D}^0 h^\pm$  and  $B^\pm \rightarrow J/\psi K^\pm$  decays, two-body invariant-mass vetoes were applied in the  $[1830, 1900] \text{ MeV}/c^2$  interval around the  $\bar{D}^0$  mass ( $1865 \text{ MeV}/c^2$ ), and in the  $[3050, 3150] \text{ MeV}/c^2$  interval around  $J/\psi$  mass ( $3096 \text{ MeV}/c^2$ ).

## 3.6 Summary

The strategy to select the  $B^\pm \rightarrow h^\pm h^+ h^-$  candidates can be summarised according to the following sequence of selections:

1. **Trigger:** Generic pre-selection to pick interesting events of  $B$  hadronic decays from  $pp$  collision.
2. **Stripping:** Generic pre-selection to group three-body hadronic  $B$  decays.
3. **Loose PID:** Specific loose requirements applied on particle identification variables to reduce the peaking background and reduce the samples for the multivariate analysis.
4. **Multivariate Analysis:** Aims to significantly suppress the combinatorial background by employing a BDT optimisation.
5. **Final PID:** Final particle identification requirement to reduce as much as possible cross-feed background contributions.
6. **Mass Vetoes:** Two-body invariant-mass vetoes to suppress intermediate charmed background contributions.

Subsequently, the samples containing the events that survived the selection stages are apt to be inspected and analysed in measurements such as those described in Chapters 4 and 5.



## Chapter 4

# $CP$ -asymmetry measurements in $B^\pm \rightarrow h^\pm h^+ h^-$ decays

This chapter details a  $CP$ -asymmetry measurement of the four  $B^\pm \rightarrow h^\pm h^+ h^-$  decay channels:  $B^\pm \rightarrow K^\pm \pi^+ \pi^-$ ,  $B^\pm \rightarrow K^\pm K^+ K^-$ ,  $B^\pm \rightarrow \pi^\pm \pi^+ \pi^-$  and  $B^\pm \rightarrow \pi^\pm K^+ K^-$ . This analysis was performed using  $5.9 \text{ fb}^{-1}$  of data collected by the LHCb during Run 2 at a centre-of-mass energy of 13 TeV, and complements the measurement performed with Run 1 data presented in Ref. [21], reported in Eqs. 1.25.

### 4.1 Measurement Strategy

Following the  $B^\pm \rightarrow h^\pm h^+ h^-$  event selection described in Chapter 3, the data samples are in order for analyses to be performed. With the aim of estimating the physical  $CP$  asymmetry precisely, one needs to account for other small asymmetry contributions:

- **Production asymmetry ( $A_P$ ):** The production rate of  $B^+$  and  $B^-$  is not expected to be the same at LHCb due to the  $pp$  nature of the collisions. Since protons are constituted of  $uud$  quarks, only  $u$  valence quarks are available, leading to different production rates for  $B^+$  ( $u\bar{b}$ ) and  $B^-$  ( $\bar{u}b$ ). Since until the analysis moment there was no measurement of  $A_P$  with Run 2 data, the one used was obtained from Run 1 data:  $A_P = (-0.74 \pm 0.15)\%$  [84].
- **Detection asymmetry ( $A_D$ ):** The detection asymmetry accounts for any experimental effect leading to distinct probabilities of observing a  $B^+ \rightarrow h'^+ h^+ h^-$  decay with respect to  $B^- \rightarrow h'^- h^+ h^-$ . It includes the difference between particle and anti-particle interaction with matter, detector acceptance and reconstruction. For  $B^\pm \rightarrow h'^\pm h^+ h^-$  decays, we assume that the net detection asymmetry is due to the bachelor hadron  $h'^\pm$ . Thus, the term  $A_D$  expresses the difference in the interaction of the final-state particles (kaons and pions) with the detector material. The LHCb collaboration previously evaluated these asymmetries as  $A_D^K = (-1.26 \pm 0.18)\%$  [85], while for pions, it was found to be consistent with zero  $A_D^\pi = (0.00 \pm 0.25)\%$  [86]. In this analysis, these asymmetries are implemented as a correction when constructing the acceptance model, discussed in Subsection 4.3.3.

As seen in Eq. 1.22, the basic procedure to experimentally obtain the physical  $CP$  asymmetry consists of determining the number of  $B^+$  and  $B^-$  candidates in the

data samples, which is accomplished by the invariant-mass fit (further discussed in Section 4.2). The mass-fit parameter raw charge asymmetry is defined as

$$A_{\text{RAW}} \equiv \frac{N_{\text{sig}}^- - N_{\text{sig}}^+}{N_{\text{sig}}^- + N_{\text{sig}}^+}, \quad (4.1)$$

where  $N_{\text{sig}}^\pm$  are the number of  $B^\pm$  signal events indirectly obtained from the mass fit result. They are calculated from mass-fit parameters  $N_{\text{sig}} \equiv N_{\text{sig}}^+ + N_{\text{sig}}^-$  and  $A_{\text{RAW}}$  as

$$\begin{aligned} A_{\text{RAW}} &= \frac{N_{\text{sig}}^- - (N_{\text{sig}} - N_{\text{sig}}^-)}{N_{\text{sig}}^- + (N_{\text{sig}} - N_{\text{sig}}^-)} \Rightarrow N_{\text{sig}}^- = \frac{N_{\text{sig}}}{2} (1 + A_{\text{RAW}}) \\ A_{\text{RAW}} &= \frac{(N_{\text{sig}} - N_{\text{sig}}^+) - N_{\text{sig}}^+}{(N_{\text{sig}} - N_{\text{sig}}^+) + N_{\text{sig}}^+} \Rightarrow N_{\text{sig}}^+ = \frac{N_{\text{sig}}}{2} (1 - A_{\text{RAW}}) \end{aligned} \quad (4.2)$$

These numbers of  $B^-$  and  $B^+$  events include phase-space acceptance effects, *i.e.*, decay dynamics and data selection may affect signal efficiency. Thus, an acceptance correction is required (see Section 4.3). The acceptance-corrected raw asymmetry is defined as [21]:

$$A_{\text{RAW}}^{\text{ACC}} \equiv \frac{N_{\text{acc}}^- - N_{\text{acc}}^+}{N_{\text{acc}}^- + N_{\text{acc}}^+} = \frac{\frac{N_{\text{sig}}^-}{R} - N_{\text{sig}}^+}{\frac{N_{\text{sig}}^-}{R} + N_{\text{sig}}^+}, \quad (4.3)$$

and is calculated from the mass-fit parameter  $A_{\text{RAW}}$  and the acceptance-correction factor  $R$  by substituting the expressions for  $N_{\text{sig}}^\pm$  from Eqs. 4.2 into Eq. 4.3 as

$$A_{\text{RAW}}^{\text{ACC}} = \frac{1 + A_{\text{RAW}} - R + A_{\text{RAW}} \cdot R}{1 + A_{\text{RAW}} + R - A_{\text{RAW}} \cdot R}. \quad (4.4)$$

As  $A_{\text{RAW}}^{\text{ACC}}$  is a composition of asymmetries from different sources, noting that  $A_D$  is already included in the acceptance correction, the number of events corrected by the acceptance could also be written as

$$\begin{aligned} N_{\text{acc}}^- &= \frac{N_{\text{acc}}^- + N_{\text{acc}}^+}{2} (1 + \mathcal{A}_{\text{CP}})(1 + A_P), \\ N_{\text{acc}}^+ &= \frac{N_{\text{acc}}^- + N_{\text{acc}}^+}{2} (1 - \mathcal{A}_{\text{CP}})(1 - A_P). \end{aligned} \quad (4.5)$$

Substituting Eqs. 4.5 into Eq. 4.3, the acceptance-corrected raw asymmetry can be expressed in terms of  $\mathcal{A}_{\text{CP}}$  and  $A_P$ :

$$A_{\text{RAW}}^{\text{ACC}} = \frac{\mathcal{A}_{\text{CP}} + A_P}{1 + \mathcal{A}_{\text{CP}} A_P}. \quad (4.6)$$

Finally, we can rewrite Eq. 4.6 by isolating  $\mathcal{A}_{\text{CP}}$ :

$$\mathcal{A}_{\text{CP}} = \frac{A_{\text{RAW}}^{\text{ACC}} - A_P}{1 - A_{\text{RAW}}^{\text{ACC}} A_P}. \quad (4.7)$$

The corresponding statistical uncertainty is obtained from error propagation of Eq. 4.7, assuming no correlation term.

## 4.2 $B^\pm$ Candidate Invariant-Mass Fit

The extraction of the total signal yields and their raw asymmetries of the studied samples are executed by simultaneous unbinned extended maximum-likelihood fits of the  $B^+$  and  $B^-$  invariant-mass distributions in the 5080-5580 MeV/ $c^2$  mass range. As discussed in Section 3.3, the background contributions are classified as combinatorial, partially-reconstructed and peaking backgrounds. The probability density functions (PDF) used to parametrise signal and background distributions were implemented and fitted using the ROOFIT package [87] (based on C++) and are described next.

### 4.2.1 Background Studies

After the final selection, some background contributions are still present in the invariant-mass spectrum, and thus their contributions must be taken into account for the determination of signal yields in the  $B$  mass fit.

The cross-feed contributions were studied using simulated samples after selection in order to find their expected yields as a fraction of the signal yield and their shape parameters in the  $B^\pm$  invariant-mass spectrum. The fraction of a given background with respect to the signal yield is evaluated as:

$$f_{bkg} \equiv \frac{N_{bkg}}{N_{sig}} = \frac{\mathcal{B}_{bkg}}{\mathcal{B}_{sig}} \times \frac{\epsilon_{bkg}}{\epsilon_{sig}}, \quad (4.8)$$

where  $N_{sig}$  is the signal yield,  $f_{bkg}$  is the fraction of the background component, and  $\mathcal{B}_{sig}$  and  $\mathcal{B}_{bkg}$  are the branching ratios of the signal and background channels, respectively, given by the Ref. [40]. The efficiencies are calculated as the fraction of generated events that survive the complete selection.

A broad study of 4-body decay channels from simulation was also conducted. Since the partially-reconstructed background components lie to the left of the signal peaks, their normalisation is always left to float in the fit. The  $B_s^0$  decay channels are found to contribute with a large fraction only to the  $B^\pm \rightarrow \pi^\pm K^+ K^-$  spectrum, and are included as a component only in this channel with a fraction that is left to float. The  $B^0$  and  $B^\pm$  decay channels are included in all fits as a single partially-reconstructed 4-body decay component with a fraction left to float.

The fraction and shape results generally served as input and were fixed to the invariant-mass fit. The fractions obtained from the channels studied are given in Table 4.1. Channels with a background fraction less than 1% were neglected.

### 4.2.2 Fit Model

The reconstructed invariant-mass distributions of  $B^\pm$  are modelled by a sum of PDFs describing the signal distribution and background contributions and each PDF is multiplied by the corresponding number of events:

$$\mathcal{P}^\pm = N_{sig}^\pm \mathcal{P}_{sig}^\pm + \sum_i N_{bkg_i}^\pm \mathcal{P}_{bkg_i}^\pm, \quad (4.9)$$

The summation term represents the possible contributions of combinatorial, peaking, or partially-reconstructed backgrounds.

Signal mode	Background contribution	Fraction (%)
$B^\pm \rightarrow K^\pm \pi^+ \pi^-$	$B^\pm \rightarrow \eta'(\rho^0 \gamma) K^\pm$	11.4
	$B^\pm \rightarrow \pi^\pm \pi^+ \pi^-$	8.9
	$B^\pm \rightarrow \pi^\pm K^+ K^-$	0.6
	$B^\pm \rightarrow K^\pm K^+ K^-$	0.5
$B^\pm \rightarrow K^\pm K^+ K^-$	$B^\pm \rightarrow \pi^\pm K^+ K^-$	1.8
	$B^\pm \rightarrow K^\pm \pi^+ \pi^-$	1.3
$B^\pm \rightarrow \pi^\pm \pi^+ \pi^-$	$B^\pm \rightarrow K^\pm \pi^+ \pi^-$	3.6
$B^\pm \rightarrow \pi^\pm K^+ K^-$	$B^\pm \rightarrow \pi^\pm \pi^+ \pi^-$	0.4
	$B^\pm \rightarrow K^\pm \pi^+ \pi^-$	9.6
	$B^\pm \rightarrow K^\pm K^+ K^-$	8.5
	$B_s^0 \rightarrow D_s^- \pi^+$	1.1

TABLE 4.1: Fractions obtained from MC studies of the relevant background modes for each of the  $B^\pm \rightarrow h^\pm h^+ h^-$  decays.

Using the expressions for  $N_{sig}^\pm$  in Eqs. 4.2, one can define the invariant-mass fit model for  $B^\pm$  distributions as

$$\begin{aligned}
\mathcal{P}^\pm = & \left[ \frac{N_{sig}}{2} \left( 1 \mp A_{RAW}^{sig} \right) \right] \mathcal{P}_{sig}^\pm + \\
& + \left[ \frac{N_{comb}}{2} \left( 1 \mp A_{RAW}^{comb} \right) \right] \mathcal{P}_{comb}^\pm + \\
& + \sum_i \left[ \frac{(f_{bkg_i} N_{sig})}{2} \left( 1 \mp A_{RAW}^{bkg_i} \right) \right] \mathcal{P}_{bkg_i}^\pm
\end{aligned} \tag{4.10}$$

where  $A_{RAW}^{sig}$  is the raw asymmetry term, related to the  $CP$  asymmetry (also including detection and production asymmetries) of the decay channel,  $A_{RAW}^{comb}$  is related to any asymmetry that may exist in combinatorial background, and  $A_{RAW}^{bkg_i}$  refers to the raw charge asymmetry of peaking or partially-reconstructed background components. Now the summation term indicates the contributions of peaking or partially-reconstructed background only.

### Signal fit model

Initially, peaking contributions, such as the signal and cross-feed components, would be modelled in the fit as the sum of two Crystal Ball (CB) functions with common parameters for the  $B^+$  and  $B^-$  samples. MC studies demonstrated this particular choice not only to be able to describe well the signal distribution but also to provide a better fit stability to data in comparison to the old model involving a Cruiff function. The Crystal Ball function is defined as a core Gaussian distribution, with one

of its tails replaced by a power-law distribution [88]

$$\text{CB}_i(m; \mu_i, \sigma_i, a_i, n_i) = \begin{cases} \exp\left[-\frac{(m - \mu_i)^2}{2\sigma_i^2}\right], & \text{if } \frac{(m - \mu_i)}{\sigma_i} > -a_i \\ \left(\frac{n_i}{|a_i|}\right)^{n_i} \left(\frac{n_i - a_i^2}{|a_i|} - \frac{(m - \mu_i)}{\sigma_i}\right)^{-n_i} \exp\left(-\frac{a_i^2}{2}\right), & \text{if } \frac{(m - \mu_i)}{\sigma_i} \leq -a_i \end{cases} \quad (4.11)$$

where  $m$  is the reconstructed mass variable,  $\mu$  and  $\sigma$  are the standard Gaussian mean and standard deviation,  $a$  defines the number of standard deviations from the mean at which the transition from the core to the power-law tail occurs, and  $n$  is the power-law exponent. This definition of the Crystal Ball determines the low-mass, left-hand tail as the power law component; it is possible to define it such that the right-hand tail is the power law component instead.

The addition of the two CB functions is performed with the requirement that the mean and standard deviation of the core Gaussian distribution is the same for both CB functions. Additionally, they are added with one tail to each side such that the resulting function encapsulates the different effects that modify the tails on both sides. The right-hand power-law tail describes the effect of tracking imperfections and other detector effects that are non-Gaussian in nature, while the left-hand tail not only encapsulates these effects but also the effect of missing final-state radiation on the mass distribution. Finally, an extra parameter  $f_{\text{CB}}$  is included to allow for the two CB functions to contribute in different amounts relative to each other. A sum of two Crystal Ball functions with these additional requirements is often referred as a ‘double Crystal Ball’ (dCB) function:

$$\text{dCB}(m) = f_{\text{CB}} \cdot \text{CB}_1(m; \mu_1, \sigma_1, a_1, n_1) + (1 - f_{\text{CB}}) \cdot \text{CB}_2(m; \mu_2, \sigma_2, a_2, n_2). \quad (4.12)$$

However, due to the larger data set from Run 2, signal fit-model studies were conducted and they revealed the requirement of the inclusion of a Gaussian function to the previous double Crystal Ball. The Gaussian or normal distribution is associated with purely statistical processes such as the uncertainty of the invariant-mass distribution, which is obtained from momentum and energy measurements. The motivation for the need of multiple Gaussian functions, Crystal Balls included, comes *a priori* from the fact that the sum of a finite number of Gaussian functions does not correspond to a normal distribution. Each one of them accounts for distinct momentum regions. For instance, high-momentum tracks go through smaller deflections due to the LHCb magnet and thus provide measurements with larger errors. The signal model study is further detailed in Section A.1.

The new signal PDF for  $B^+$  and  $B^-$  is composed by the sum of Gaussian and a double Crystal Ball function with common parameters for  $B^+$  and  $B^-$  samples as defined as

$$\mathcal{P}_{\text{sig}}^\pm = f_G \cdot G(m; \mu_G, \sigma_G) + (1 - f_G) \cdot f_{\text{CB}} \cdot \text{CB}_1(m; \mu_1, \sigma_1, a_1, n_1) + (1 - f_G) \cdot (1 - f_{\text{CB}}) \cdot \text{CB}_2(m; \mu_2, \sigma_2, a_2, n_2). \quad (4.13)$$

where the Gaussian contribution,  $G(m)$ , is written as

$$G(m; \mu_G, \sigma_G) = \frac{1}{\sqrt{2\pi}} \exp \left[ -\frac{(m - \mu_G)^2}{2\sigma_G^2} \right]. \quad (4.14)$$

In the situation of the signal model being given by Equation 4.12, the individual Crystal Balls have their contribution fractions given by  $f_{CB_1} = f_{CB}$  and  $f_{CB_2} = 1 - f_{CB}$ . Alternatively, in the case of the adopted signal fit model (Equation 4.13), these fractions are expressed as

$$\begin{aligned} f_{CB_1} &= (1 - f_G) \cdot f_{CB}, \\ f_{CB_2} &= (1 - f_G)(1 - f_{CB}). \end{aligned}$$

Moreover, discrepancies between simulated samples and signal data distributions are expected since the simulation cannot describe all detector effects perfectly. In order to account for these disparities, coefficients are introduced in the model to fluctuate the mean and width parameters of both the Gaussian and the double Crystal Ball functions.

For the dCB function, the means ( $\mu_1$  and  $\mu_2$ ) and widths ( $\sigma_1$  and  $\sigma_2$ ) are parametrised as

$$\begin{aligned} \mu_i &= m_0 \cdot c(m_0)_{MC}, \\ \sigma_i &= \sigma \cdot c(\sigma)_{MC}, \end{aligned} \quad (4.15)$$

where  $m_0$  and  $\sigma$  are the initial values obtained from the MC, and  $c(m_0)_{MC}$  and  $c(\sigma)_{MC}$  are two coefficients introduced to model, respectively, the variation of  $\mu_i$  and  $\sigma_i$ . These coefficients are free in the fit to data.

For the Gaussian distribution, the mean and width are respectively parametrised as

$$\begin{aligned} \mu_G &= m_0 \cdot c(m_0)_{MC} \\ \sigma_G &= \sigma' \cdot c(\sigma)_{MC} \end{aligned} \quad (4.16)$$

where  $m_0$  and  $\sigma'$  are the initial values obtained from the MC, and  $c(m_0)_{MC}$  and  $c(\sigma)_{MC}$  are the same two coefficients introduced to model, respectively, the variation of  $\mu_G$  and  $\sigma_G$ . These coefficients are free in the fit to data. In summary, from Eqs. 4.15-4.16, one notes that the same  $m_0$  is used for  $G(m)$  and dCB( $m$ ). As for the width, the double Crystall Balls share the parameter whereas the Gaussian function has a separate one.

To recapitulate, the signal PDF depends on 11 parameters:

$$\mathcal{P}_{sig}^\pm(m; m_0, c(m_0)_{MC}, \sigma, c(\sigma)_{MC}, \sigma_G, n_1, a_1, n_2, a_2, f_G, f_{CB}) \quad (4.17)$$

determined from an MC fit and fixed in the fit to data.

### Combinatorial-background fit model

The combinatorial background component present in all four mass spectra is described by an exponential distribution

$$\mathcal{P}_{comb}(m; b) = \exp [b \cdot (m - 5080)] , \quad (4.18)$$

where  $b$ , the free parameter, is extracted from the data fit.

### Peaking-background fit model

The shapes and fractions of the peaking backgrounds due to cross-feeds from the other  $B^\pm \rightarrow h^\pm h^+ h^-$  decays are determined from simulation and fixed in the fit of the data samples. However, the  $B^\pm \rightarrow K^\pm \pi^+ \pi^-$  cross-feed in the  $B^\pm \rightarrow K^\pm K^+ K^-$  decay channel, whose fraction seems to have been overestimated by the simulation, had this parameter left to float in the fit. The peaking background PDFs,  $\mathcal{P}_{bkg}(m)$ , are parametrised by a double Crystal Ball as defined in Eq. 4.12. The asymmetry term of this type of background was fixed at zero in most cases during the fit.

### Partially-reconstructed-background fit model

Partially-reconstructed backgrounds exhibit significantly different behaviour with respect to the components originating from true  $B^\pm \rightarrow h^\pm h^+ h^-$  candidates. Such backgrounds are better modelled as ARGUS functions [89], convoluted with a Gaussian distribution to account for the resolution of the detector. The generalised ARGUS function is defined as

$$\begin{aligned} \mathcal{A}(m; m_t, c, p) = & \frac{2^{-p} c^{2(p+1)}}{\Gamma(p+1) - \Gamma(p+1, c^2/2)} \\ & \times \frac{m}{m_t^2} \left(1 - \frac{m^2}{m_t^2}\right)^p \times \exp\left[-\frac{1}{2}c^2 \left(1 - \frac{m^2}{m_t^2}\right)\right] \end{aligned} \quad (4.19)$$

when  $m < m_t$ , and zero elsewhere. The expressions  $\Gamma(n)$  and  $\Gamma(n, l)$  represent the gamma and upper incomplete gamma functions, respectively,  $m_t$  is the threshold mass value,  $c$  governs the curvature of the function, and  $p$  controls the falling of the slope. The Argus shape parameters, as well as its fractional yield with respect to the signal, are left free to float in the fit.

### Fit Procedure

The fit procedure can be summarised in the following steps:

1. Studies over MC samples are conducted to estimate cross-feed background fractions and shape parameters.
2. A preliminary fit over MC samples is performed to determine shape parameters for the signal model.
3. A fit over data samples is performed where extracted shapes and fractions from MC are fixed, whereas convenient parameters are left to float either for convergence or parameter-determination purposes.

Due to the  $B^\pm \rightarrow K^\pm \pi^+ \pi^-$  sample size and complexity, some particularities were included to improve the fit of this channel. Different mean values for the Gaussian and the Crystal Balls of the signal model were used. Also, the cross-feed charge asymmetries were fixed on the  $\mathcal{A}_{CP}$  values evaluated in the previous measurement [21].

### 4.2.3 Fit Results

The simultaneous mass fits to the  $B^-$  and  $B^+$  data samples are shown in Figures 4.1-4.4. The charge asymmetry is observable by the height difference between the  $B^+$  and  $B^-$  peaks. The complete fit model is represented by the blue full line and comprehends signal and the backgrounds indicated in the legend. Section A.2 collects additional invariant-mass fit results: Table A.1 lists all parameters extracted from the fit to the data samples and Figures A.5-A.8 display the plots for MC and data sample mass fits in logarithmic scale along with pull plots and  $\chi^2/\text{ndf}$  information for the four  $B^\pm \rightarrow h^\pm h^+ h^-$  decays. Finally, the total number of candidates and the raw asymmetry for each channel obtained from the combined Run 2 data sample is shown in Table 4.2.

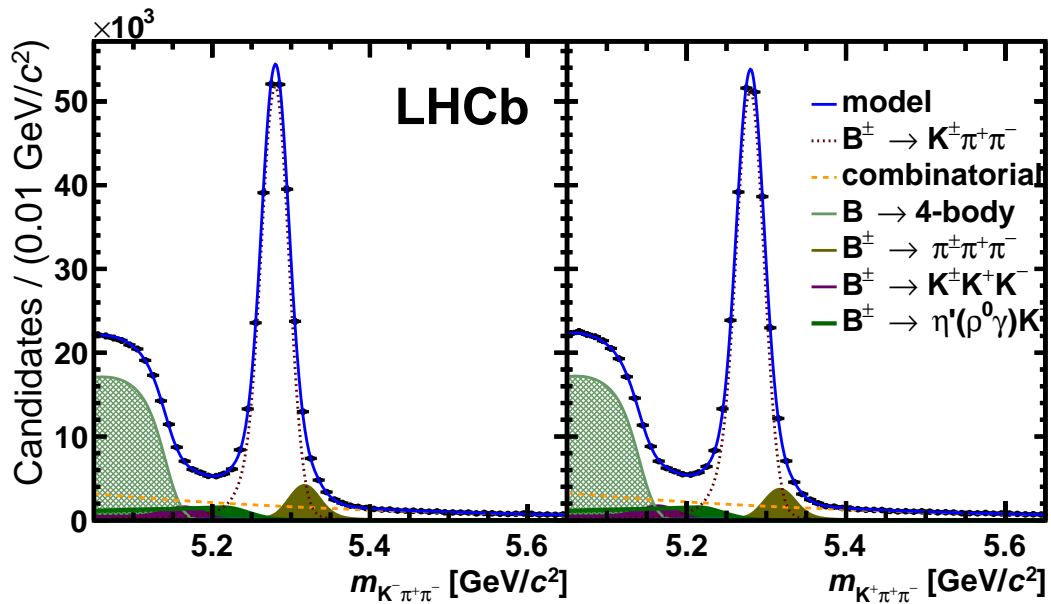


FIGURE 4.1: Fitted invariant-mass distributions of  $B^\pm \rightarrow K^\pm \pi^+ \pi^-$  separated by charge: (left)  $B^-$  and (right)  $B^+$  candidates.

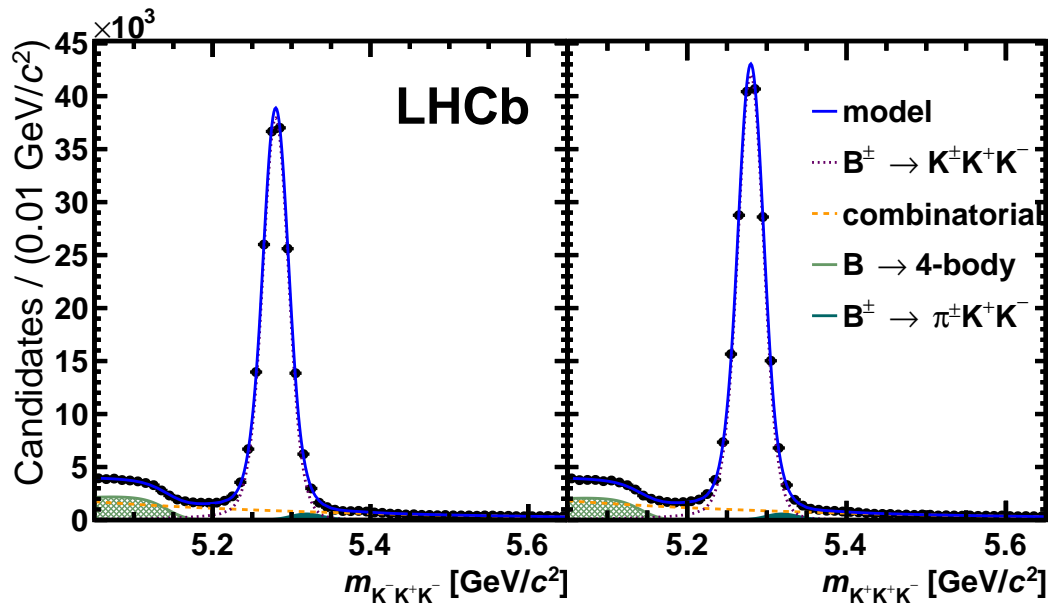


FIGURE 4.2: Fitted invariant-mass distributions of  $B^\pm \rightarrow K^\pm K^+ K^-$  separated by charge: (left)  $B^-$  and (right)  $B^+$  candidates.

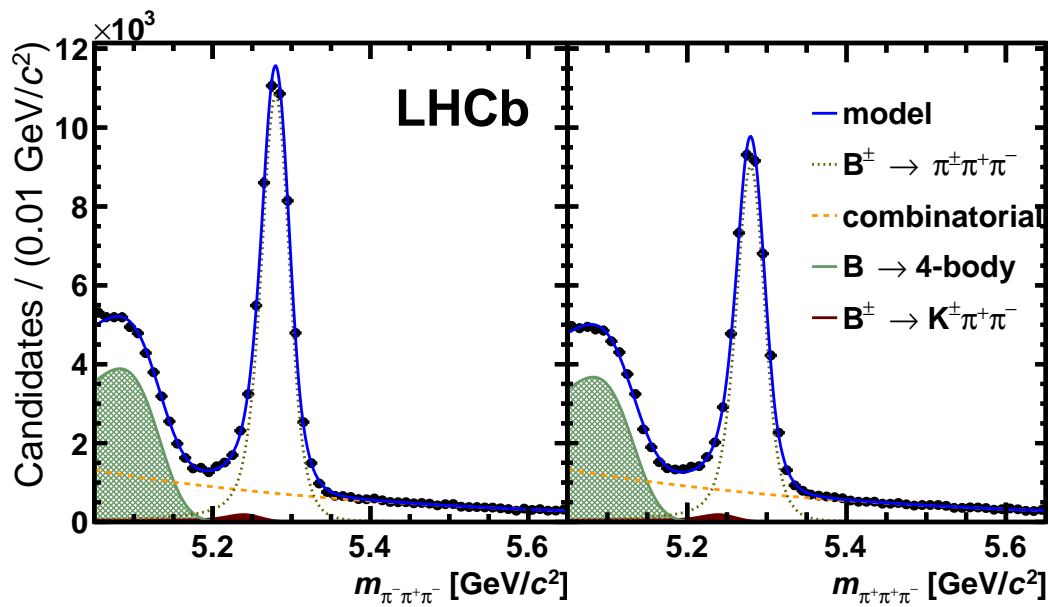


FIGURE 4.3: Fitted invariant-mass distributions of  $B^\pm \rightarrow \pi^\pm \pi^+ \pi^-$  separated by charge: (left)  $B^-$  and (right)  $B^+$  candidates.

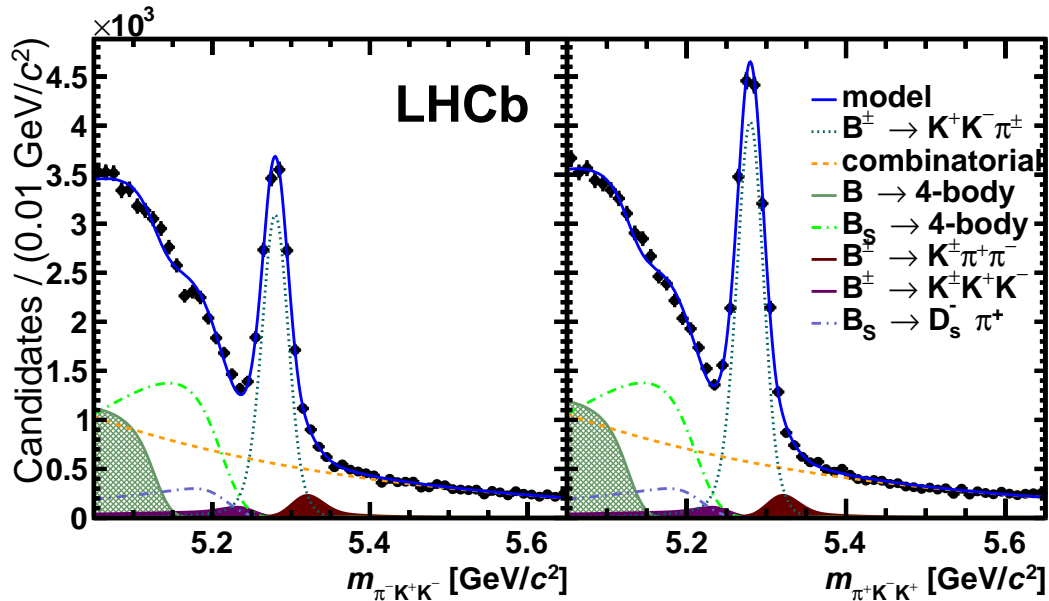


FIGURE 4.4: Fitted invariant-mass distributions of  $B^\pm \rightarrow \pi^\pm K^+ K^-$  separated by charge: (left)  $B^-$  and (right)  $B^+$  candidates.

Channel	$B^\pm$ Yield ( $N_S$ )	$A_{\text{RAW}}$
$B^\pm \rightarrow K^\pm \pi^+ \pi^-$	$492574 \pm 870$	$+0.0055 \pm 0.0016$
$B^\pm \rightarrow K^\pm K^+ K^-$	$355162 \pm 650$	$-0.0513 \pm 0.0018$
$B^\pm \rightarrow \pi^\pm \pi^+ \pi^-$	$101056 \pm 404$	$+0.0910 \pm 0.0036$
$B^\pm \rightarrow \pi^\pm K^+ K^-$	$32832 \pm 300$	$-0.1323 \pm 0.0068$

TABLE 4.2:  $B^\pm$  signal yield and raw asymmetry of the four charmless three-body decays  $B^\pm \rightarrow h^\pm h^+ h^-$  for the combined Run 2 data set.

### 4.3 Phase-Space Acceptance

Three-body decays are dominated by several intermediate contributions, which can interfere with each other leading to structures in the phase-space. Those structures are related to the dynamics of the decay, which is not known *a priori*, and thus not well represented by the simulation. In addition, the selection cuts can distort the signal, which leads to non-uniform efficiency and  $A_{\text{RAW}}$  distributions across the Dalitz plot. As the signal efficiency may be incorrectly represented in MC simulation, an acceptance correction needs to be performed.

As discussed in Section 1.2, a common feature of  $B^\pm \rightarrow h^\pm h^+ h^-$  decays is that both signal and background events populate the kinematic boundaries of the Dalitz plot. Thus, the variation of the efficiency occurring over small areas of the Dalitz plot become difficult to describe in detail. The solution adopted by some analyses is to apply a transformation to the kinematic variables that maps the Dalitz plot into a square: the so-called square Dalitz plot (SDP). Such transformation (Eq. 1.11) improves the resolution in the areas with great variation of efficiency by expanding the corner and the borders of the Dalitz plot relative to the less populated region. Thus, the phase-space acceptance correction is adequately performed by obtaining the acceptance maps in the SDP representation. Figure 4.5 shows a comparison between

the standard Dalitz plot (left) and the square one (right) with the highlighted regions mapped after the transformation.

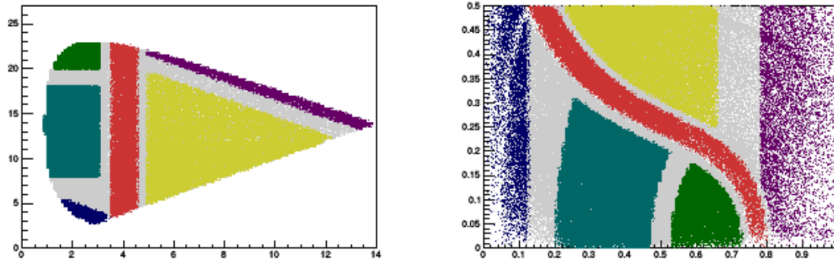
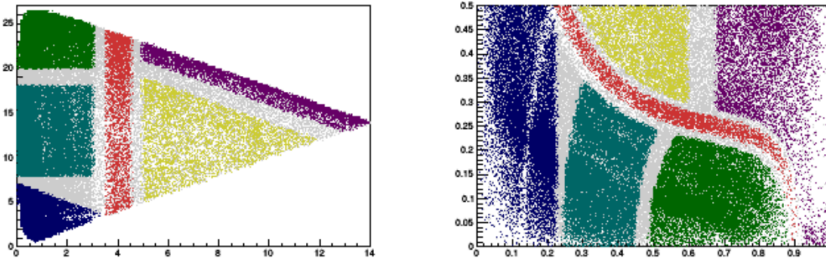
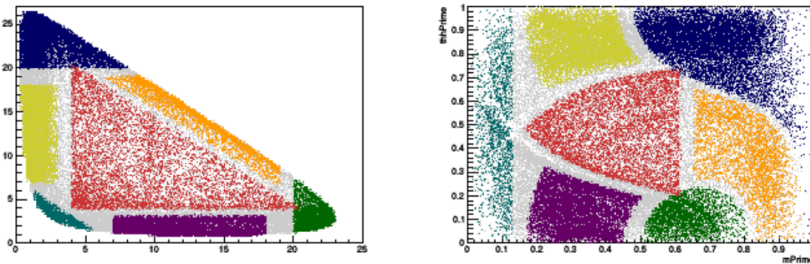
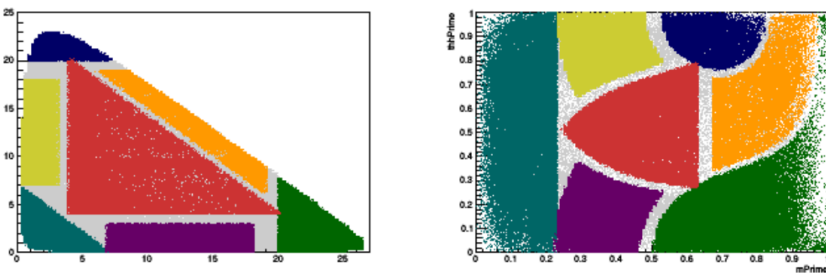
(a)  $B^\pm \rightarrow K^\pm K^+ K^-$ (b)  $B^\pm \rightarrow \pi^\pm \pi^+ \pi^-$ (c)  $B^\pm \rightarrow \pi^\pm K^+ K^-$ (d)  $B^\pm \rightarrow K^\pm \pi^+ \pi^-$ 

FIGURE 4.5: Simulated data projections in the standard Dalitz plot (left) and Square Dalitz plot (right) mapping the transformation of each phase-space region.

### 4.3.1 Acceptance Correction

For each decay channel, the acceptance maps are obtained in the SDP representation for  $B^+$  and  $B^-$  MC samples separately, and each  $B^\pm$  acceptance histogram is built

up from the following individual contribution:

- **Year:** separated by year (2015 and 2016) to take into account the different data-taking configurations.
- **Polarity:** separated by magnet polarity (MagUp and MagDown) to take into account the left-right asymmetry of the detector.
- **Trigger configuration:** This separation is performed in order to apply the trigger correction which needs to be performed due to differences between the TOS efficiency in data and MC simulation. Once the acceptance maps are generated, a L0 trigger efficiency correction is applied.

The acceptance maps of each subsample follow the  $15 \times 15$  binning scheme in the SDP representation and are generated from reconstructed MC samples with kinematic, trigger and TrueID (true MC particle identity variable) cuts, corrected by the efficiency weights for the detection asymmetries and PID cuts divided by a flat generated MC:

$$\text{ACC}^\pm = \frac{\text{histo}_{\text{cor}}^\pm}{\text{histo}_{\text{flat}}^\pm} \quad (4.20)$$

where

- $\text{histo}_{\text{cor}}^\pm$ : Binned histogram of the reconstructed large MC samples generated flat in SDP with selection requirements and corrections.
- $\text{histo}_{\text{flat}}^\pm$ : Binned histogram of large simulated samples generated around the  $4\pi$  solid angle, with no cuts at the generator level to reproduce the phase-space distribution before any acceptance and selection cuts, then scaled to the total estimated number of generated MC.

### 4.3.2 PID Efficiency

In MC simulated samples, a few experimental factors are not considered, like variations in the performance of the RICH detectors for different periods of data recording or non-linear effects like magnetic-field distortions in the detector and temperature variations. This leads to an unreliable simulation of the PID variables and thus to large systematic effects if the PID efficiency. In this sense, the efficiency associated to the identification of pions and kaons is obtained using the tools from the PIDCalib package [90].

This is a data-driven technique that uses a full set of calibration samples of pions, kaons and protons from the denominated ‘golden modes’. It provides the efficiency for the PID selection in Table 3.8 by using samples produced in the experiment that were reconstructed without the RICH detector. The efficiency is obtained as weighting factors for each final-state track and magnet polarity, then added event per event in the acceptance maps.

### 4.3.3 Detection-Asymmetry Correction

For each decay channel, kaon and pion detection asymmetries are included in the acceptance maps as an event per event weight given by

$$w_i^{\text{AD}}(h^+ h'^+ h^-) = (1 + A_D^+) (1 + A'_D) (1 - A_D^-) \quad (4.21)$$

and similarly for its complex conjugate,

$$w_i^{A_D}(h^- h'^- h^+) = (1 - A_D^-) (1 - A_D') (1 + A_D^+) . \quad (4.22)$$

### Kaon detection asymmetry

It is known that the interaction of kaons with the detector can be different for  $K^+$  and  $K^-$ . This asymmetry is momentum-dependent, leading to differences in the detection efficiency [91]. Therefore,  $A_D^K$  is measured in different ranges of kaon momentum. The method for determining the asymmetry is the same as the one described in [92].

### Pion detection asymmetry

For the pion detection asymmetry  $A_D^\pi$  in Eqs. 4.21 and 4.22, we use the values provided in the LHCb analysis note [92], which were obtained using Run 1 data since the pion detection asymmetry is not yet available for Run 2. This is considered acceptable as the pion detection asymmetry was measured to be approximately zero.

### Trigger correction

A correction to the acceptance is performed to take into account the differences between data and MC with respect to the TOS trigger efficiency. The correction is applied to the mutually exclusive TOS and TOS MC subsamples [93]. It consists of the ratio evaluation for data and MC TOS efficiencies in the SDP variables. These correction histograms are then applied to the respective acceptance on each category.

### 4.3.4 Combining Acceptance Maps

Finally, as a last step in the construction of the efficiency model, the acceptance histograms of each category are combined. For each year, the TOS and TISnotTOS histograms are added in the same proportion as data while keeping the overall normalisation. The MagUp and MagDown subsamples are also proportionally added according to the recorded luminosity achieved by year. To obtain the overall acceptance, an average of 2015 and 2016 accordingly to their contribution is performed. Figure 4.6 illustrates how the acceptance maps are combined, while Figures 4.7 and 4.8 display the final acceptance maps for  $B^+$  and  $B^-$  candidates in each decay channel.

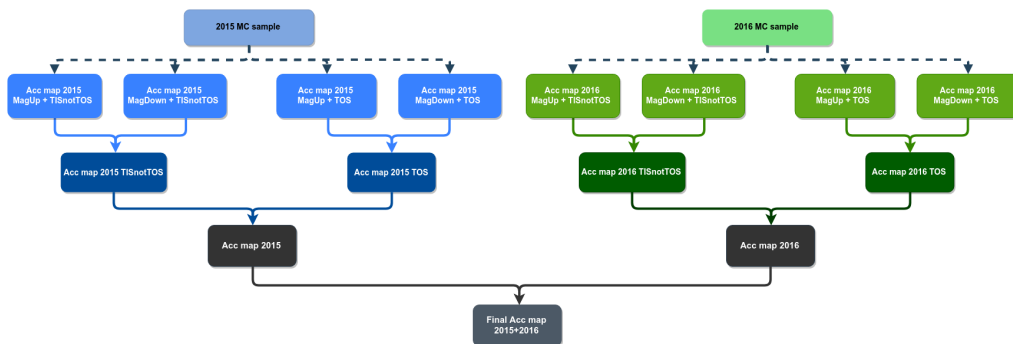
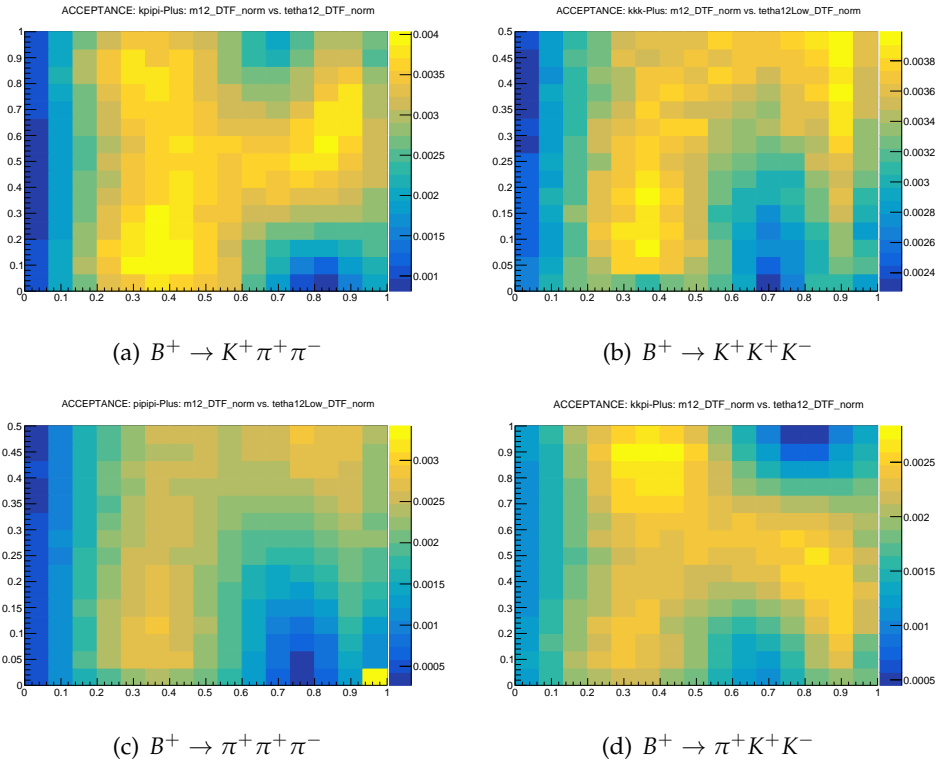
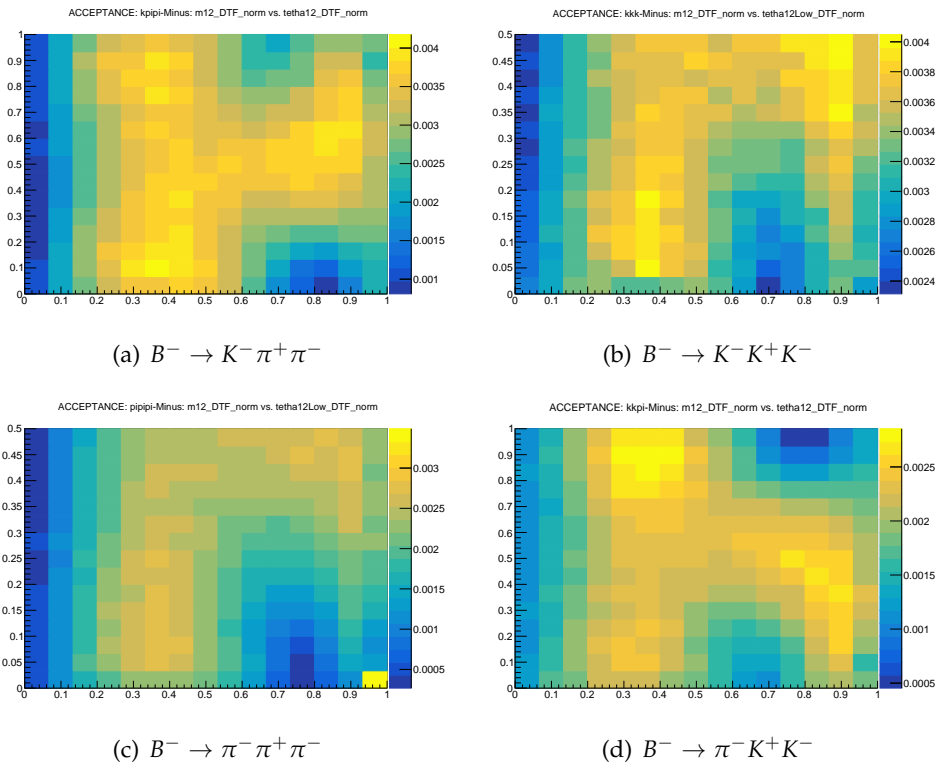


FIGURE 4.6: Flux diagram presenting all the stages needed for the acceptance construction by each charge and channel.

FIGURE 4.7: Overall acceptance maps for  $B^+ \rightarrow h^+ h^+ h^-$  decays.FIGURE 4.8: Overall acceptance maps for  $B^- \rightarrow h^- h^+ h^-$  decays.

### 4.3.5 Average Efficiency

For the determination of  $\mathcal{A}_{CP}$ , the  $A_{RAW}$  needs to be corrected by the average efficiency of the acceptance. The efficiency is then corrected by data distributions as the MC samples used in the acceptance maps do not describe the dynamics of the decays. It is done through the  $s\mathcal{P}$ Plot technique [94], where each MC event is weighted according to the signal data distribution to reproduce the population in the data DP. Thus, the harmonic average of the efficiencies for  $B^+$  and  $B^-$  separately is given by

$$\langle \epsilon^\pm \rangle = \frac{\sum_i^{\text{evts}} w_i^\pm}{\sum_i^{\text{evts}} \frac{w_i^\pm}{\epsilon_i}}, \quad (4.23)$$

where  $w_i$  is the signal data weight and  $\epsilon_i$  is the efficiency for each event  $i$  obtained from the final acceptance maps. To propagate the MC statistical errors to the acceptance, we varied the acceptance histogram content of each bin according to a Gaussian distribution centred at the original value and with width given by the error. The  $A_{RAW}$  value is corrected by the ratio:

$$R = \frac{\langle \epsilon^- \rangle}{\langle \epsilon^+ \rangle} \quad (4.24)$$

Table 4.3 reports  $\langle \epsilon^+ \rangle$ ,  $\langle \epsilon^- \rangle$  and  $R$  for 2015-2016 data. Finally, the acceptance-corrected raw asymmetry  $A_{RAW}^{\text{ACC}}$  is calculated by Eq. 4.4.

Decay channel	$\langle \epsilon^+ \rangle$	$\langle \epsilon^- \rangle$	$R \pm \Delta R$
$B^\pm \rightarrow K^\pm K^+ K^-$	0.0035	0.0035	$1.002 \pm 0.003$
$B^\pm \rightarrow \pi^\pm K^+ K^-$	0.0021	0.0020	$0.977 \pm 0.004$
$B^\pm \rightarrow K^\pm \pi^+ \pi^-$	0.0030	0.0031	$1.019 \pm 0.003$
$B^\pm \rightarrow \pi^\pm \pi^+ \pi^-$	0.0016	0.0017	$1.033 \pm 0.005$

TABLE 4.3: Average efficiency for  $B^+$  and  $B^-$  and the  $R$  ratio for the binned acceptance for  $B^\pm \rightarrow h^\pm h^+ h^-$  decay channels with 2015-2016 data.

## 4.4 Results and Prospects

In this chapter, an update to the measurement of the phase-space integrated  $CP$  asymmetries of the  $B^\pm \rightarrow h^\pm h^+ h^-$  decay modes was presented. The measurement was performed using data collected with the LHCb detector at a centre-of-mass energy of 13 TeV during Run 2 of the LHC, corresponding to an integrated luminosity of  $5.9 \text{ fb}^{-1}$ . The asymmetries were calculated by Eq. 4.7 to be:

$$\begin{aligned} \mathcal{A}_{CP}(B^\pm \rightarrow K^\pm \pi^+ \pi^-) &= +0.003 \pm 0.003, \\ \mathcal{A}_{CP}(B^\pm \rightarrow K^\pm K^+ K^-) &= -0.045 \pm 0.003, \\ \mathcal{A}_{CP}(B^\pm \rightarrow \pi^\pm \pi^+ \pi^-) &= +0.082 \pm 0.005, \\ \mathcal{A}_{CP}(B^\pm \rightarrow \pi^\pm K^+ K^-) &= -0.114 \pm 0.007, \end{aligned}$$

where the uncertainty is statistical. The evaluation of the systematic error is expected to be concluded in the near future. The integrated  $CP$  asymmetry is consistent with zero for  $B^\pm \rightarrow K^\pm \pi^+ \pi^-$ , positive for  $B^\pm \rightarrow \pi^\pm \pi^+ \pi^-$ , and negative for  $B^\pm \rightarrow K^\pm K^+ K^-$  and  $B^\pm \rightarrow \pi^\pm K^+ K^-$  decays and their magnitudes vary from 0.3%

up to 11.4% for  $B^\pm \rightarrow K^\pm \pi^+ \pi^-$  and  $B^\pm \rightarrow \pi^\pm K^+ K^-$  decays, respectively. The preliminary  $\mathcal{A}_{CP}$  significances, calculated by dividing the central values by the summation in quadrature of the uncertainties, are about 1.0 standard deviations ( $\sigma$ ) for the  $B^\pm \rightarrow K^\pm \pi^+ \pi^-$  channel, and surpass  $5\sigma$  for  $B^\pm \rightarrow K^\pm K^+ K^-$ ,  $B^\pm \rightarrow \pi^\pm \pi^+ \pi^-$  and  $B^\pm \rightarrow \pi^\pm K^+ K^-$ . The results are compatible within up to  $3\sigma$  with the previous LHCb measurement, based on  $3.0 \text{ fb}^{-1}$  of recorded data at centre-of-mass energies of 7 and 8 TeV during Run 1:

$$\begin{aligned} \mathcal{A}_{CP}(B^\pm \rightarrow K^\pm \pi^+ \pi^-) &= +0.025 \pm 0.004 \pm 0.004 \pm 0.007, \\ \mathcal{A}_{CP}(B^\pm \rightarrow K^\pm K^+ K^-) &= -0.036 \pm 0.004 \pm 0.002 \pm 0.007, \\ \mathcal{A}_{CP}(B^\pm \rightarrow \pi^\pm \pi^+ \pi^-) &= +0.058 \pm 0.008 \pm 0.009 \pm 0.007, \\ \mathcal{A}_{CP}(B^\pm \rightarrow \pi^\pm K^+ K^-) &= -0.123 \pm \underbrace{0.017}_{\sigma_{\text{stat}}} \pm \underbrace{0.012}_{\sigma_{\text{syst}}} \pm \underbrace{0.007}_{\sigma_{J/\psi K^\pm}} \end{aligned}$$

As described in Chapter 3, the  $B^\pm \rightarrow h^\pm h^+ h^-$  candidates were selected through inclusive selection criteria based on decay topology and kinematics. The background contributions were then reduced by using a multivariate analysis and particle identification requirements.

A simultaneous fit to  $B^+$  and  $B^-$  invariant-mass distributions, detailed in Section 4.2, was performed in each decay channel in order to determine the number of  $B$  candidates. The results for the signal yields were measured to be about 493k candidates for the  $B^\pm \rightarrow K^\pm \pi^+ \pi^-$  channel, 355k for  $B^\pm \rightarrow K^\pm K^+ K^-$ , 101k for  $B^\pm \rightarrow \pi^\pm \pi^+ \pi^-$  and 33k for  $B^\pm \rightarrow \pi^\pm K^+ K^-$ . In comparison with the past measurement, those values coincide to yields about 3 times larger for  $B^\pm \rightarrow K^\pm \pi^+ \pi^-$  and  $B^\pm \rightarrow K^\pm K^+ K^-$ , 4 times for  $B^\pm \rightarrow \pi^\pm \pi^+ \pi^-$  and 5 times for  $B^\pm \rightarrow \pi^\pm K^+ K^-$ . The raw charge asymmetry was obtained from these signal yields by Eq. 4.4. The inclusive  $CP$  asymmetry was finally obtained by correcting the raw asymmetry from acceptance effects and asymmetries experimentally introduced: the detection asymmetry of pions and kaons and the production asymmetry of  $B^+$  and  $B^-$  at the LHCb experiment.

## Chapter 5

# $CP$ -asymmetry measurements in $B \rightarrow PV$ decays

This chapter covers experimental results regarding  $CP$ -asymmetry measurements in  $B \rightarrow PV$  decays, *i.e.*, the ones resulting in a pseudoscalar,  $P$ , and a vector resonance,  $V$ . In Section 5.1, a brief discussion is developed about the theoretical particularities of such decays. Afterwards, Section 5.2 introduces a simple model-independent method to extract the  $CP$  asymmetry from these channels, escaping the complication presented in the commonly employed amplitude analyses. Section 5.3 presents the obtained results by the method.

### 5.1 Introduction

The theoretical studies discussed in literature for  $B \rightarrow PV$  decays restrain themselves to the low-mass  $SU(3)$  vector particles  $\rho(770)^0$ ,  $K^*(892)^0$  and  $\phi(1020)$ . Both  $\rho(770)$  and  $K^*(892)$  decays are restricted to one single two-body channel, whose branching fractions are virtually 100% to  $\pi\pi$  and to  $K\pi$ , respectively. Otherwise,  $\phi(1020)$  decays roughly 85% of the times into  $K\bar{K}$ , but it can also decay into three pions through the  $\rho\pi$  channel with a branching fraction of 15%. In this analysis, the pseudoscalars of concern are kaons and pions.

Table 5.1 covers some of the physical properties of these particles, whereas Table 5.2 summarizes their decay information. Table 5.3 associates the relevant resonant  $B \rightarrow PV$  states to their final-state  $B^+ \rightarrow h^+h^+h^-$  decays. It also displays the branching fractions of the resonant states, which can be compared with the  $B^\pm \rightarrow h^\pm h^+ h^-$  information presented in Table 1.2.

Vector	Quark content	Rest mass (MeV/ $c^2$ )	Width (MeV/ $c^2$ )
$\rho(770)^0$	$\frac{u\bar{u}-d\bar{d}}{\sqrt{2}}$	$775.26 \pm 0.25$	$149.1 \pm 0.8$
$K^*(892)^0$	$d\bar{s}$	$895.55 \pm 0.20$	$47.3 \pm 0.5$
$\phi(1020)$	$s\bar{s}$	$1019.461 \pm 0.02$	$4.249 \pm 0.013$

TABLE 5.1: Summary of relevant neutral vector resonances and their physical properties [40].

The isobar model, further described in Subsection 1.3.3, as well as K-matrix and other amplitude analysis models, holds the bachelor particle as a simple spectator of the process. In other words, this quasi-two-body or (2+1) approximation states that resonances produced in heavy-meson decays do not interact with the third particle. Within this scenario, the  $CPT$  constraint in  $B \rightarrow PV$  processes, involving  $\rho(770)^0$  or  $K^*(892)^0$ , suggests that there is no room to observe  $CP$  asymmetry in these channels.

Vector	Decay channel	Branching fraction
$\rho(770)$	$\pi\pi$	$\sim 100\%$
$K^*(892)$	$K\pi$	$\sim 100\%$
$\phi(1020)$	$K^+K^-$	$(49.2 \pm 0.5)\%$
	$K_L^0 K_S^0$	$(34.0 \pm 0.4)\%$
	$\rho\pi / \pi^+\pi^-\pi^0$	$(15.24 \pm 0.33)\%$

TABLE 5.2: Summary of relevant neutral vector resonances and their main decay channels [40].

Final-State Decay	Resonant State	BF
$B^+ \rightarrow \pi^+\pi^+\pi^-$	$\rho(770)^0\pi^+$	$(8.3 \pm 1.2) \times 10^{-6}$
$B^+ \rightarrow K^+\pi^+\pi^-$	$K^+\rho(770)^0$	$(3.7 \pm 0.5) \times 10^{-6}$
	$K^*(892)^0\pi^+$	$(1.01 \pm 0.08) \times 10^{-5}$
$B^+ \rightarrow \pi^+K^+K^-$	$K^+\bar{K}^*(892)^0$	$< 1.1 \times 10^{-6}$
$B^+ \rightarrow K^+K^+K^-$	$K^+\phi(1020)$	$(8.8_{-0.6}^{+0.7}) \times 10^{-6}$

TABLE 5.3: Branching fractions of the relevant vector resonant states, with their associated final-state  $B^+ \rightarrow h^+h^+h^-$  decay channels [40].

As far as the  $\phi(1020)$  resonance is concerned, it could eventually show  $CP$  asymmetry in a particular final state, but that does not seem to be the case due to the low contribution of tree diagrams to such decays. It is also worth mentioning that the absence of final-state interactions is a hadronic constraint and therefore, the impossibility to observe  $CP$  asymmetry in those processes is independent from the relative short-distance contribution from penguin diagrams.

At least three other manners exist for  $B \rightarrow PV$  decays to result in inelastic rescattering that can produce  $CP$  violation:

- (i) Rescattering from the pseudoscalar-vector pair such as  $PV \rightarrow P'X$ , where  $X$  represents a new particle or particles.
- (ii) The  $PV$  final state not produced promptly, but as a result of a rescattered process coming from another two-body decay channel, with the strong transition matrix related with the one in (i) by detailed balance, or time-reversal invariance.
- (iii) A three-body rescattering involving the bachelor particle.

As mentioned in Subsection 1.3.2, the  $CPT$  constraint demands that the total  $CP$  asymmetry distributed in different channels or phase-space regions that have the same flavour quantum numbers sums up to zero. Particularly for the  $B$ -meson decay, processes (i)-(iii) are estimated to provide only small contributions to the  $CP$ -asymmetry distribution in different channels coupled by the strong interaction.

## 5.2 The Model-Independent Method

With the intent of escaping the dependence of the isobar model when extracting parameters of  $CP$  asymmetry in  $B \rightarrow PV$  processes, Ref. [95] proposed a simple

model-independent experimental method to extract the  $\mathcal{A}_{CP}$  from the data. It is a fast approach that exploits the angular distribution of a vector resonance in the Dalitz plot and the knowledge that such low-mass vector meson generally shares a phase-space proximity region with a scalar meson. Thus, one can take a slice from the central mass of the light vector resonance that includes the interference with a single low-mass scalar resonance along the other Dalitz variable. These scalar resonances are typically  $\sigma$ ,  $\kappa$  and  $f_0(980)$ , or the interference can even happen with a non-resonant contribution.

### 5.2.1 Case Studies

To illustrate the method, a simple case is here demonstrated. In a particular region of the Dalitz plot, a  $B^\pm \rightarrow h_b^\pm V$  decay receives contributions exclusively from a single vector resonance ( $V$ ) along with a constant non-resonant (NR) amplitude, where  $h_b$  represents the bachelor particle. Also,  $V \rightarrow h^+ h^-$ , where  $h^+$  and  $h^-$  are the final-state hadrons, namely kaons and pions.

The simple and elegant isobar model, despite being approximate, can reveal important features. Following Equation 1.24, generally one could represent such total amplitudes for  $B^+$  and  $B^-$  charge-conjugate decays as:

$$\begin{aligned}\mathcal{M}_+ &= a_+^V e^{i\delta_+^V} F_V^{\text{BW}} \cos \theta(s_\perp, s_\parallel) + a_+^{\text{NR}} e^{i\delta_+^{\text{NR}}} F^{\text{NR}} \\ \mathcal{M}_- &= a_-^V e^{i\delta_-^V} F_V^{\text{BW}} \cos \theta(s_\perp, s_\parallel) + a_-^{\text{NR}} e^{i\delta_-^{\text{NR}}} F^{\text{NR}}\end{aligned}\quad (5.1)$$

where  $F^{\text{NR}}$  is a real scalar non-resonant amplitude, and  $\delta_\pm$  contains both the fixed weak and strong phases. For simplicity and without loss of generality, the vector resonance  $V$  is described by a Breit-Wigner (BW) function,  $F_V^{\text{BW}}$ , which is a good representation for narrow and non-overlapping resonances. The  $F_V^{\text{BW}}$  amplitude depends on  $s_\parallel \equiv (p_{h^+} + p_{h^-})^2$ , one of the invariant variables of a Dalitz plot (Equation 1.9) and has the form

$$F_V^{\text{BW}}(s_\parallel) = \frac{1}{m_V^2 - s_\parallel - im_V \Gamma_V(s_\parallel)}, \quad (5.2)$$

where  $\Gamma_V(s_\parallel)$  is the energy-dependent relativistic width. Splitting  $F_V^{\text{BW}}$  into its real and imaginary parts, one obtains

$$\begin{aligned}\mathcal{R}e \left\{ F_V^{\text{BW}}(s_\parallel) \right\} &= \frac{m_V^2 - s_\parallel}{(m_V^2 - s_\parallel)^2 + m_V^2 \Gamma_V^2(s_\parallel)}, \\ \mathcal{I}m \left\{ F_V^{\text{BW}}(s_\parallel) \right\} &= \frac{m_V \Gamma_V(s_\parallel)}{(m_V^2 - s_\parallel)^2 + m_V^2 \Gamma_V^2(s_\parallel)},\end{aligned}\quad (5.3)$$

whereas the BW squared modulus is given by:

$$\left| F_V^{\text{BW}}(s_\parallel) \right|^2 = \frac{1}{(m_V^2 - s_\parallel)^2 + m_V^2 \Gamma_V^2(s_\parallel)}. \quad (5.4)$$

The vector amplitude has an additional strong phase, inherent to the BW form, and a spin-1 factor, proportional to  $\cos \theta(s_\perp, s_\parallel)$ , which also depends on  $s_\perp \equiv (p_{h_b} + p_{h_\pm})^2$ . The angle  $\theta$  is the helicity angle, created by the intersection between the tracks of the

bachelor particle and the centre of mass of the resonance. For a vector resonance in the  $s_{\parallel}$  channel, the cosine of the helicity angle is given by [96]

$$\cos \theta(s_{\perp}, s_{\parallel}) = \frac{(M_B^2 - s_{\parallel} - M_{h_b}^2)(s_{\parallel} + M_{h_+}^2 - M_{h_-}^2) + 2s_{\parallel}(M_{h_b}^2 + M_{h_+}^2 - s_{\perp})}{\sqrt{\lambda(M_B^2, s_{\parallel}, M_{h_b}^2)} \sqrt{\lambda(s_{\parallel}, M_{h_+}^2, M_{h_-}^2)}}, \quad (5.5)$$

where  $\lambda(x, y, z)$  is the Källén function, which can be factorized as

$$\lambda(x, y, z) = [x - (\sqrt{y} + \sqrt{z})^2] [x - (\sqrt{y} - \sqrt{z})^2].$$

It was verified on toy MC samples that the behaviour of  $\cos \theta(s_{\perp}, s_{\parallel})$  remains stable as a function of  $s_{\parallel}$  around the centre value of  $s_{\parallel} = m_V^2$  within a region of about the width of the vector resonance, where  $V$  represents  $\rho(770)^0$ ,  $K^*(892)^0$  or  $\phi(1020)$ . Therefore, the helicity angle can be assumed to be a function of  $s_{\perp}$  only:  $\cos \theta(s_{\perp}, m_V^2 \pm \delta_m) \approx \cos \theta(s_{\perp}, m_V^2)$ .

As defined in Equation 1.20, the CP asymmetry is calculated from the ratio of subtracting to adding the squared moduli of  $B^-$  and  $B^+$  amplitudes. These operations between the squared moduli of the amplitudes in this case can be written as:

$$|\mathcal{M}_+|^2 \mp |\mathcal{M}_-|^2 = \left[ (a_+^V)^2 \mp (a_-^V)^2 \right] |F_V^{\text{BW}}|^2 \cos^2 \theta(s_{\perp}, s_{\parallel}) + \left[ (a_+^{\text{NR}})^2 \mp (a_-^{\text{NR}})^2 \right] |F^{\text{NR}}|^2 \quad (5.6)$$

$$+ 2 \cos \theta(s_{\perp}, s_{\parallel}) |F_V^{\text{BW}}|^2 |F^{\text{NR}}|^2 \times \quad (5.7)$$

$$\left\{ (m_V^2 - s_{\parallel}) \left[ a_+^V a_+^{\text{NR}} \cos(\delta_+^V - \delta_+^{\text{NR}}) \mp a_-^V a_-^{\text{NR}} \cos(\delta_-^V - \delta_-^{\text{NR}}) \right] \right. \quad (5.8)$$

$$\left. - m_V \Gamma_V \left[ a_+^V a_+^{\text{NR}} \sin(\delta_+^V - \delta_+^{\text{NR}}) \mp a_-^V a_-^{\text{NR}} \sin(\delta_-^V - \delta_-^{\text{NR}}) \right] \right\} \quad (5.9)$$

The method here invites us to observe the amplitude distribution on the  $s_{\perp}$  variable for events around the resonance mass, *i.e.*, for  $s_{\parallel} \approx m_V^2$ . This procedure presents a convenience in that it enables us to identify the signature of  $\cos \theta(s_{\perp}, m_V^2)$ . By doing so, one can relate the cosine signatures to a specific type of CP-asymmetry source. Inspecting Equation 5.9, one notes that the first two terms are associated to the individual direct CP asymmetry generated from BSS mechanism. The former is proportional to  $\cos^2 \theta(s_{\perp}, m_V^2)$  due to its vector nature, whereas the second is constant and associated to the scalar NR amplitude. The last two terms in Equation 5.9 are proportional to  $\cos \theta(s_{\perp}, m_V^2)$  and relate to the interference between the NR amplitude and the vector resonance. This type of CP asymmetry has two contributions: one associated to the real part of  $F_V^{\text{BW}}$  and the other, to the imaginary (Equations 5.3).

Summing up, the coefficients  $(a_{\pm}^V)^2$  track the  $\cos^2 \theta(s_{\perp}, m_V^2)$  term, which is related to a CP asymmetry from the BSS mechanism on the vector-meson decay amplitude. The coefficients  $a_{\pm}^V$  track the linear term of  $\cos \theta(s_{\perp}, m_V^2)$  and are connected to a CP asymmetry produced from the FSI interference. Finally, the coefficients  $(a_{\pm}^{\text{NR}})^2$  represent the possibility of CP asymmetry produced by the BSS mechanism in the NR amplitude. Lastly, by observing Equation 5.9 one notes that the squared amplitudes correspond to a quadratic function of  $\cos \theta(s_{\perp}, m_V^2)$ :

$$|\mathcal{M}_{\pm}|^2 = f(\cos \theta(s_{\perp}, m_V^2)) = p_0^{\pm} + p_1^{\pm} \cos \theta(s_{\perp}, m_V^2) + p_2^{\pm} \cos^2 \theta(s_{\perp}, m_V^2). \quad (5.10)$$

All these coefficients can be obtained directly from data by fitting the squared amplitudes with a quadratic function of  $\cos\theta(s_\perp, m_V^2)$ . In the data situation, fitting the squared amplitudes means the fit over the  $B^\pm$  candidate distribution. Especially, the quadratic parameters,  $p_2$ , correspond to the  $(a_\pm^V)^2$  coefficients.

Ultimately, the most important output of this method is the opportunity of a direct measurement of the  $CP$  asymmetry inherent to the BSS mechanism, within a model-independent approach. From the quadratic coefficients of the fit, one directly obtains  $\mathcal{A}_{CP}$  for the vector resonance without needing a model for the amplitude:

$$\mathcal{A}_{CP}^V = \frac{(a_-^V)^2 - (a_+^V)^2}{(a_-^V)^2 + (a_+^V)^2}. \quad (5.11)$$

Another asset of the method is that the consideration of one low-mass scalar resonance like  $\sigma, \kappa$  or  $f_0(980)$  in lieu of a non-resonant contribution does not alter its main features. In this case, the charmless three-body  $B$ -decay amplitudes are given by replacing the NR amplitude for a Breit-Wigner, denoted as  $F_S^{\text{BW}}$ , in Eqs. 5.1. The scalar resonance has a varying inherent strong phase from the BW amplitude that will interfere with the vector amplitude. The difference between squared moduli for  $B^+$  and  $B^-$  amplitudes now results in:

$$\begin{aligned} |\Delta\mathcal{M}|^2 &= |\mathcal{M}_+|^2 - |\mathcal{M}_-|^2 \\ &= \left[ (a_+^V)^2 - (a_-^V)^2 \right] |F_V^{\text{BW}}|^2 \cos^2\theta + \left[ (a_+^S)^2 - (a_-^S)^2 \right] |F_S^{\text{BW}}|^2 + 2\cos\theta |F_V^{\text{BW}}|^2 |F_S^{\text{BW}}|^2 \times \\ &\quad \left\{ \left[ (m_V^2 - s)(m_S^2 - s) - m_V\Gamma_V m_S\Gamma_S \right] \left[ a_+^V a_+^S \cos(\delta_+^V - \delta_+^S) - a_-^V a_-^S \cos(\delta_-^V - \delta_-^S) \right] \right. \\ &\quad \left. - \left[ m_V\Gamma_V (m_S^2 - s) - m_S\Gamma_S (m_V^2 - s) \right] \left[ a_+^V a_+^S \sin(\delta_+^V - \delta_+^S) - a_-^V a_-^S \sin(\delta_-^V - \delta_-^S) \right] \right\}. \end{aligned} \quad (5.12)$$

Comparing this formula with Equation 5.9, it is evident that the coefficients related to the BSS mechanism are identical and the interference term is also proportional to  $\cos\theta(s_\perp, m_V^2)$ . Thus, the amplitudes can be parametrised by the same quadratic function of  $\cos\theta(s_\perp, m_V^2)$  as in the previous example (Equation 5.10).

Finally, the constraint of  $CPT$  applied to the  $CP$  asymmetry in the hypotheses of no three-body rescattering contributions, implies that the integral over the phase space of the asymmetry, computed with Equation 5.9, should vanish. Concerning the linear term in  $\cos\theta$ , it will vanish after integration over the phase space regardless of the situation since it is an odd function. Therefore,  $CPT$  implies that the integration over phase space of the first two terms of Equation 5.9 must be zero. The most probable solution consists in coefficients from  $B^+$  and  $B^-$ ,  $a_\pm$ , being the same. However, they could also be different and compensate upon integration over phase space.

### 5.2.2 Method Viability

As reported by Ref. [95], pseudo-experiments were generated for the  $B^\pm \rightarrow \pi^\pm \pi^+ \pi^-$  decay by using Toy MC simulations with the intent to validate the method presented. The samples for these studies were produced to simulate the results obtained in the BaBar experiment [97], by fitting the data with an isobar model which includes the  $\rho(770)^0$  and  $\rho(1450)^0$  vector resonances, the  $f_0(980)$  scalar, the  $f_2(1270)$  tensor and a flat non-resonant contribution. In their fitting results, they obtained  $CP$  asymmetry in all the resonance channels considered, including the NR contribution.

Specifically for the channel of concern,  $B^\pm \rightarrow \rho(770)^0 \pi^\pm$ , a  $\mathcal{A}_{CP}^V = (18 \pm 7)\%$  was measured.

Two different scenarios were considered for the Toy MC: one of them consisted of applying BaBar inputs for magnitude and phase, and a second one where the magnitudes for  $\rho(770)^0$  were manipulated to produce a null  $CP$ -asymmetry. In both situations, 1000 samples were generated via the LAURA<sup>++</sup> [49] package, each with 20,000 events. In order to confirm the viability of the method in identifying  $CP$ -asymmetry signatures in these samples, the goal was to measure the  $\mathcal{A}_{CP} = 18\%$  obtained by BaBar in the first case, and to find  $\mathcal{A}_{CP} = 0$  in the second one.

The procedure adopted to calculate  $\mathcal{A}_{CP}$  happened as follows:

1. A  $50 \text{ MeV}/c^2$  window around the two-body invariant mass of the vector resonance  $\rho(770)^0$  was chosen and integrated along the parallel Dalitz variable ( $s_{\parallel}$ ), in this case  $m^2(\pi^+ \pi^-)_{\text{low}}$ .
2. The  $B^+$  and  $B^-$  binned distribution histograms were projected into the orthogonal Dalitz variable ( $s_{\perp}$ ), in this case  $m^2(\pi^+ \pi^-)_{\text{high}}$ , and then fitted with a quadratic polynomial function in the region of 5 to  $23.5 \text{ GeV}^2/c^4$ .
3. Finally,  $\mathcal{A}_{CP}$  was calculated by taking the quadratic coefficients obtained from the fitted curves and replacing their values into Equation 5.11.

The plots for the fit with the quadratic function over random samples of  $\rho(770)^0$  are given by the left side of Figure 5.1.

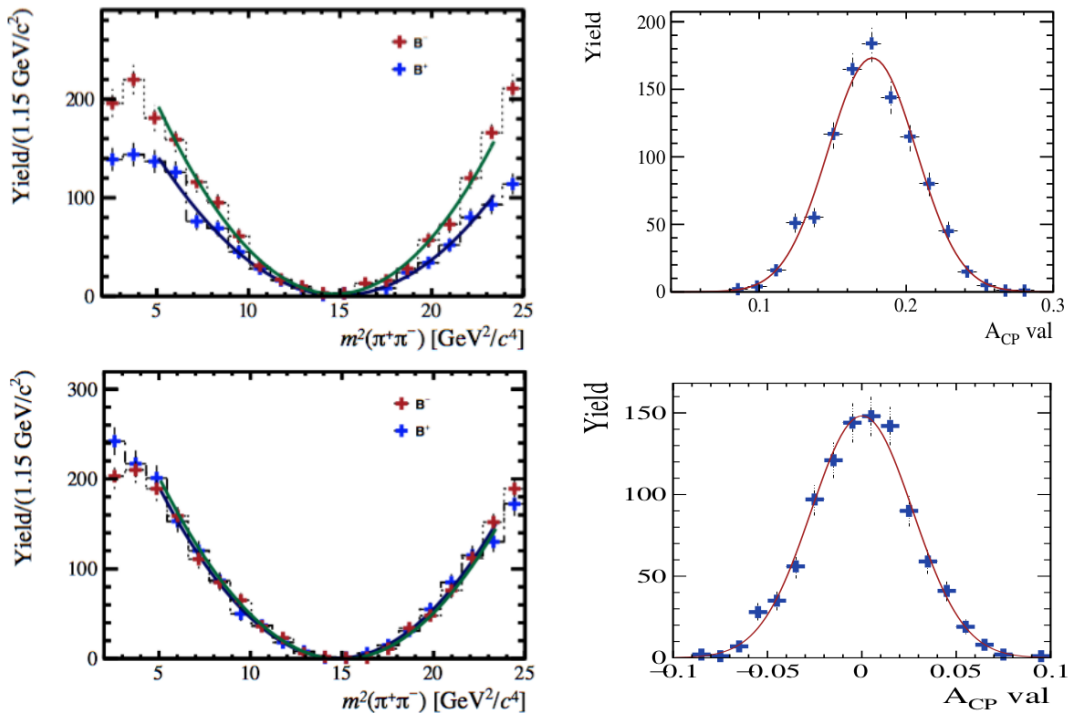


FIGURE 5.1: Left: Quadratic fit to a random sample of  $B^+$  and  $B^-$   $\rho(770)^0$  distributions generated with  $\mathcal{A}_{CP}^{\rho(770)^0} = 0.18$  (top) and  $\mathcal{A}_{CP}^{\rho(770)^0} = 0.0$  (bottom). Right: Distributions of  $\mathcal{A}_{CP}^{\rho(770)^0}$  main values obtained from the fits to the 1000 pseudo-experiments with 20000 events each, simulated with: the BaBar results (top), and  $\mathcal{A}_{CP}^{\rho(770)^0} = 0.0$  (bottom).

The final results were obtained by the distribution of  $\mathcal{A}_{CP}^{\rho(770)^0}$  central values of simulated samples (right side of the same Figure) to be  $\mathcal{A}_{CP}^{\rho(770)^0} = 0.177 \pm 0.03$  and  $\mathcal{A}_{CP}^{\rho(770)^0} = 0.00 \pm 0.03$  for the two cases under study, respectively. Overall, the Toy MC study turned out to be very satisfactory as the values for  $\mathcal{A}_{CP}^{\rho(770)^0}$  obtained from the fit coefficients agree with the correspondent input values within the statistical errors.

In regard to the data scenario, the situation is more complex because there are also resonances present in a crossed channel, that are functions of  $s_{\perp}$ , and can interfere in a nontrivial form with the distribution of  $\cos\theta(s_{\perp}, m_V^2)$ , thus producing other sources of  $CP$  asymmetry beyond the BSS mechanism. However, these interferences are localised at lower masses (in general, below  $5 \text{ GeV}^2/c^4$ ) so, taking into account the big phase space accessible for charmless three-body  $B$  decays, even if this interference region gets excluded, there is still a large sector to perform the analysis and extract  $\mathcal{A}_{CP}^V$  measurements from the fit parameters, with good resolution and limited errors.

## 5.3 Results

This section presents the  $\mathcal{A}_{CP}^V$  measurements in  $B \rightarrow PV$  decays categorised by their final-state  $B^{\pm} \rightarrow h^{\pm}h^+h^-$  decays.

After undergoing the selection routine depicted in Chapter 3, the data samples still need to be acceptance-corrected, as analogously described in Section 4.3, to account for interference structures in the phase space and to overall non-uniform signal efficiencies. This time, the adopted procedure involved probing the acceptance variables in the projection histograms over  $s_{\perp}$  and scaling them to properly correspond to efficiencies, *i.e.*, values from 0 to 1, as shown in Figures B.1(a)–B.5(a). Then, the  $B^+$  and  $B^-$  distributions, such as the ones shown in the left side of Figure 5.1, were divided by the scaled acceptance histograms.

The  $\mathcal{A}_{CP}^V$  for each resonance was calculated by Equation 5.11, where the  $(a_{\pm}^V)^2$  amplitude coefficients were extracted from the a quadratic fit (Equation 5.10) parameters,  $p_2$ , over the individual  $B^+$  and  $B^-$  projected distributions along the  $s_{\perp}$  Dalitz variable. The statistical errors for these  $CP$ -asymmetry measurements were estimated by uncertainty propagation of the fit parameters  $p_2^+$  and  $p_2^-$ .

An extensive study was conducted by altering and fluctuating fit conditions, such as resonance mass window, fit regions, parametrisation of the quadratic function, background reduction by  $s\mathcal{W}$ eight, and charge-separated acceptance correction. Overall, the fluctuation of the resonance mass window, over the span of tens of  $\text{MeV}/c^2$  in the case of  $\rho(770)^0$  and  $K^*(892)^0$ , did not drastically modify the measured  $\mathcal{A}_{CP}^V$ , counting as an indication of the method's robustness.

To guarantee that mostly signal yields would be selected the (5247-5315)  $\text{MeV}/c^2$  three-body invariant mass range was imposed. The convention adopted for the mass window around the resonance mass was to choose the nominal width for each vector meson as listed in Table 5.1. Finally, as mentioned in Section 4.1, we still need to account for the production asymmetry, and thus  $\mathcal{A}_{CP}^V$  is obtained from Equation 4.7.

### 5.3.1 $B^{\pm} \rightarrow \pi^{\pm}\pi^+\pi^-$ decay

From the  $B^{\pm}$  yield distributions over  $m(\pi^+\pi^-)_{\text{low}}$  in  $B^{\pm} \rightarrow \pi^{\pm}\pi^+\pi^-$  decays in Figure 5.2(a), one might spot the existence of two peaking structures. The first is our

mass range of interest due to the presence of the  $\rho(770)^0$  vector, and the second [98], to the presences of the  $\pi\pi \rightarrow KK$  rescattering and the  $f_2(1270)$  tensor. In Figure 5.2(b), one may see the  $B^- - B^+$  yield histogram, which emphasises raw charge asymmetry. The first bump corresponds to the  $\sigma$  scalar [98], also known as  $f_0(500)$ , and the second is associated with the peaking structure around  $1300 \text{ MeV}/c^2$ .

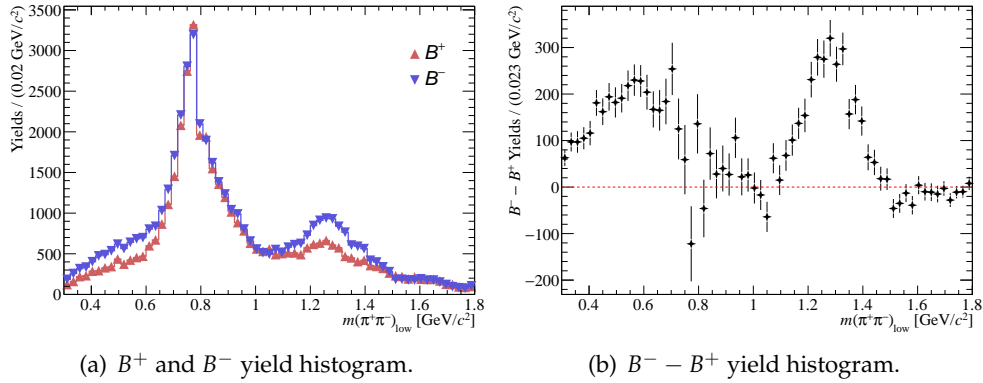


FIGURE 5.2: Yield distributions over  $m(\pi^+\pi^-)_{\text{low}}$  for  $\rho(770)^0$  in  $B^\pm \rightarrow \pi^\pm \pi^+ \pi^-$ .

For  $B^+ \rightarrow \rho(770)^0 \pi^+$  and its  $CP$ -conjugate channel, a  $150 \text{ MeV}/c^2$  mass window centred around  $\rho(770)^0$  mass in  $m(\pi^+\pi^-)_{\text{low}}$  and a  $[5, 21] \text{ GeV}^2/c^4$  fit region in  $m^2(\pi^+\pi^-)_{\text{high}}$  were chosen. The events selected by the mass window, projected over  $s_\perp$ , are highlighted in green in Figure 5.3(a).

Figure 5.3(b) illustrates the quadratic fit performed over the  $B^+$  and  $B^-$  acceptance-corrected yield distributions that extracted the parameters reported in Table 5.4. The goodness-of-fit parameter  $\chi^2/\text{ndf}$  is also listed. Lastly, Figure 5.3(c) displays the  $B^- - B^+$  yield distribution, which is calculated by the subtraction of the  $B^\pm$  distributions from Figure 5.3(b), and its quadratic fit. This last fit is motivated by Equation 5.9 and its exhibition serves chiefly to illustrative purposes, thus their fit parameters were chosen not to be reported.

Fit Parameter	$B^+$	$B^-$
$p_0$	$3705 \pm 61$	$3857 \pm 62$
$p_1$	$-475.9 \pm 8.7$	$-479 \pm 8.7$
$p_2$	$15.52 \pm 0.30$	$15.08 \pm 0.30$
$\chi^2/\text{ndf}$	1.84	1.17

TABLE 5.4: Quadratic fit parameters over  $B^+$  and  $B^-$  yield distributions for  $\rho(770)^0$  in  $B^\pm \rightarrow \pi^\pm \pi^+ \pi^-$  as shown in Figure 5.3(b).

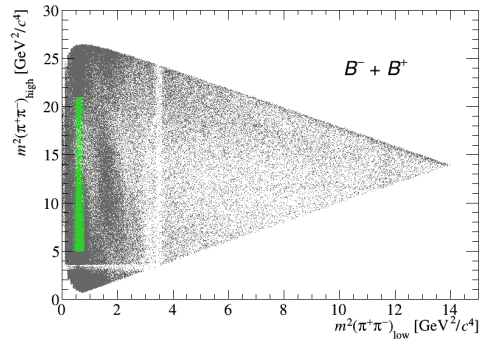
Finally, the  $CP$  asymmetry for the vector resonance was measured to be

$$\mathcal{A}_{CP}^{\rho(770)^0} = (-0.1 \pm 1.4)\%,$$

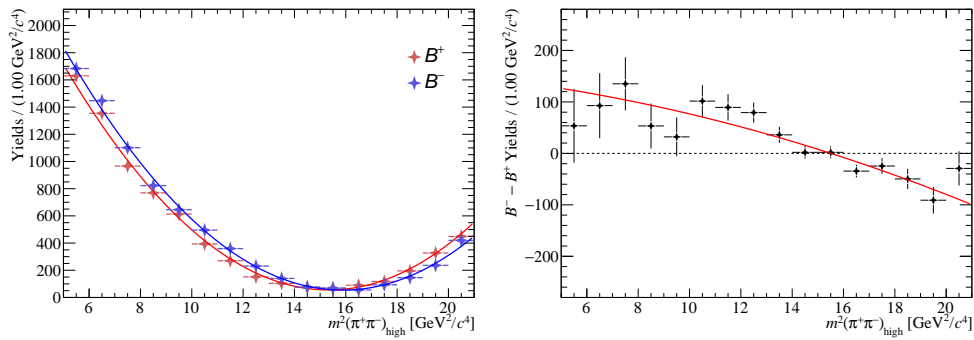
which is compatible with a null  $A_{CP}$ .

This measurement can be compared with the one obtained by the LHCb amplitude analysis for this channel [98]:  $\mathcal{A}_{CP}^{\rho(770)^0} = (0.7 \pm 1.1 \pm 1.6)\%$ . The results are

compatible with each other within  $0.4\sigma$ . One notes that the statistical errors are comparable but the amplitude analysis, despite being determined by a smaller Run 1 sample, still provides more precise measurements.



(a) Selected  $B^\pm \rightarrow \pi^\pm \pi^+ \pi^-$  Dalitz plot region in green.



(b)  $B^+$  and  $B^-$  yield distributions over  $s_\perp$  and (c)  $B^- - B^+$  yield histogram and its quadratic fit.

FIGURE 5.3: Measurement plots for  $\rho(770)^0$  in  $B^\pm \rightarrow \pi^\pm \pi^+ \pi^-$ .

### 5.3.2 $B^\pm \rightarrow K^\pm \pi^+ \pi^-$ decay

#### $\rho(770)^0$ sector

From the  $B^\pm$  yield distributions over  $m(\pi^+ \pi^-)$  in  $B^\pm \rightarrow K^\pm \pi^+ \pi^-$  decays in Figure 5.4(a), one might spot the existence of two peaking structures. The first is our mass range of interest due to the presence of the  $\rho(770)^0$  vector along with an expected non-resonant contribution, and the second, the  $f_0(980)$  scalar. In Figure 5.4(b), one may see the  $B^- - B^+$  yield histogram.

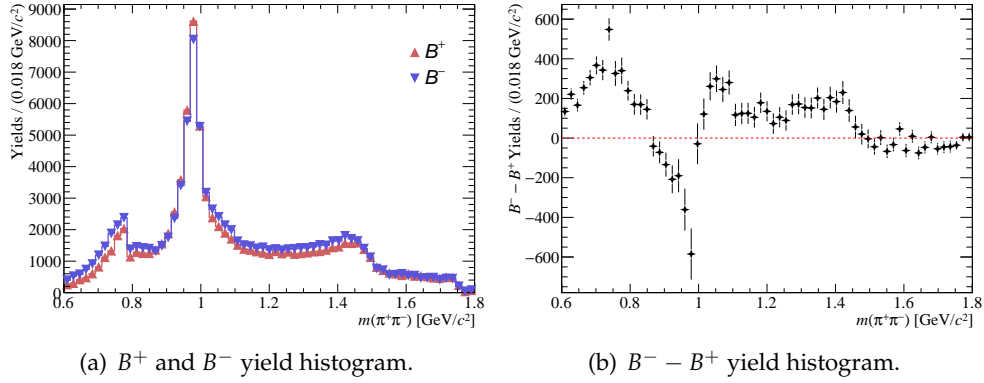


FIGURE 5.4: Yield distributions over  $m(\pi^+ \pi^-)$  for  $\rho(770)^0$  in  $B^\pm \rightarrow K^\pm \pi^+ \pi^-$ .

For  $B^+ \rightarrow \rho(770)^0 K^+$  and its  $CP$ -conjugate channel, a  $150 \text{ MeV}/c^2$  mass window centred around  $\rho(770)^0$  mass in  $m(\pi^+ \pi^-)$  and a  $[5, 22] \text{ GeV}^2/c^4$  fit region in  $m^2(K^\pm \pi^\mp)$  were chosen. The events selected by the mass window, projected over  $s_\perp$ , are highlighted in green in Figure 5.5(a). Figure 5.5(b) illustrates the quadratic fit performed over the  $B^+$  and  $B^-$  acceptance-corrected yield distributions that extracted the parameters reported in Table 5.5. Lastly, Figure 5.5(c) displays the  $B^- - B^+$  yield distribution and its quadratic fit.

Fit Parameter	$B^+$	$B^-$
$p_0$	$1524 \pm 40$	$2259 \pm 48$
$p_1$	$-232.7 \pm 6.3$	$-328.6 \pm 7.3$
$p_2$	$9.54 \pm 0.24$	$12.65 \pm 0.27$
$\chi^2/\text{ndf}$	0.85	0.58

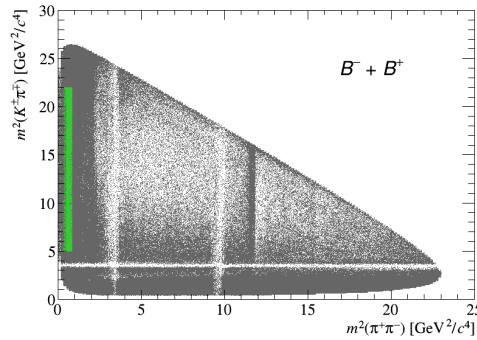
TABLE 5.5: Quadratic fit parameters of  $\rho(770)^0$  in  $B^\pm \rightarrow K^\pm \pi^+ \pi^-$  for  $B^+$  and  $B^-$  yield distributions as shown in Figure 5.5(b).

Finally, the  $CP$  asymmetry for the vector resonance was measured to be

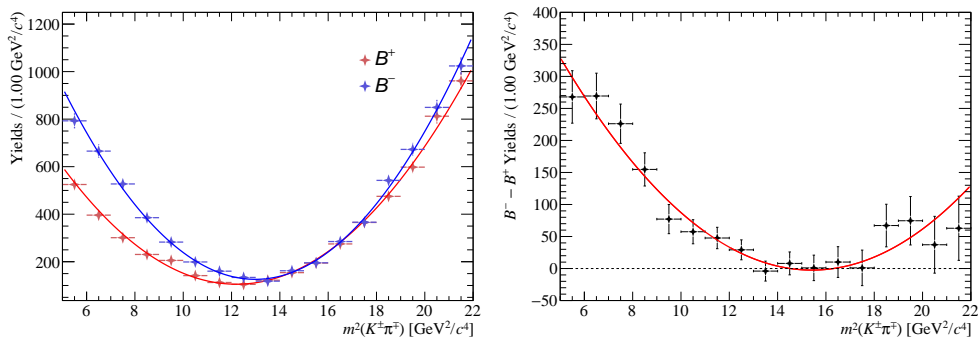
$$\mathcal{A}_{CP}^{\rho(770)^0} = (15.3 \pm 1.4)\%,$$

with impressive  $10.9\sigma$  of significance.

This measurement can be compared with the one obtained by the BaBar experiment for this channel [99]:  $\mathcal{A}_{CP}^{\rho(770)^0} = (44 \pm 10 \pm 4)\%$ . The results are compatible with each other within  $2.7\sigma$ . In this case, our measurements are quite more precise.



(a) Selected  $B^\pm \rightarrow K^\pm \pi^+ \pi^-$  Dalitz plot region in green.



(b)  $B^+$  and  $B^-$  yield distributions over  $s_\perp$  and (c)  $B^- - B^+$  yield histogram and its quadratic fit.

FIGURE 5.5: Measurement plots for  $\rho(770)^0$  in  $B^\pm \rightarrow K^\pm \pi^+ \pi^-$ .

$K^*(892)^0$  sector

From the  $B^\pm$  yield distributions over  $m(K^\pm\pi^\mp)$  in  $B^\pm \rightarrow K^\pm\pi^+\pi^-$  decays in Figure 5.6(a), one might spot the existence of two peaking structures. The first is our mass range of interest due to the presence of the  $K^*(892)^0$  vector and the second, to the  $K_0^*(1430)$  scalar. In Figure 5.6(b), one may see the  $B^- - B^+$  yield histogram, which emphasises raw charge asymmetry.

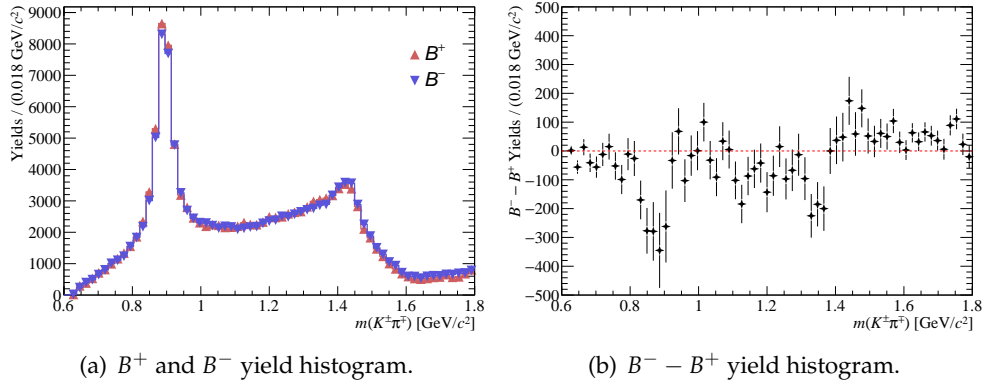


FIGURE 5.6: Yield distributions over  $m(K^\pm\pi^\mp)$  for  $K^*(892)^0$  in  $B^\pm \rightarrow K^\pm\pi^+\pi^-$ .

For  $B^+ \rightarrow K^*(892)^0\pi^+$  and its CP-conjugate channel, a  $50\text{ MeV}/c^2$  mass window centred around  $K^*(892)^0$  mass in  $m(K^\pm\pi^\mp)$  and a  $[5, 17]\text{ GeV}^2/c^4$  fit region in  $m^2(\pi^+\pi^-)$  were chosen, skipping the  $[9, 12]\text{ GeV}^2/c^4$  region due to the  $J/\psi$  mass veto and the undesired presence of  $\chi_{c0}$ . The events selected by the mass window, projected over  $s_\perp$ , are highlighted in green in Figure 5.7(a). Figure 5.7(b) illustrates the quadratic fit performed over the  $B^+$  and  $B^-$  acceptance-corrected yield distributions that extracted the parameters reported in Table 5.6. Lastly, Figure 5.7(c) displays the  $B^- - B^+$  yield distribution and its quadratic fit.

Fit Parameter	$B^+$	$B^-$
$p_0$	$2296 \pm 62$	$2158 \pm 60$
$p_1$	$-459 \pm 13$	$-435 \pm 12$
$p_2$	$24.39 \pm 0.59$	$23.23 \pm 0.57$
$\chi^2/\text{ndf}$	1.26	1.47

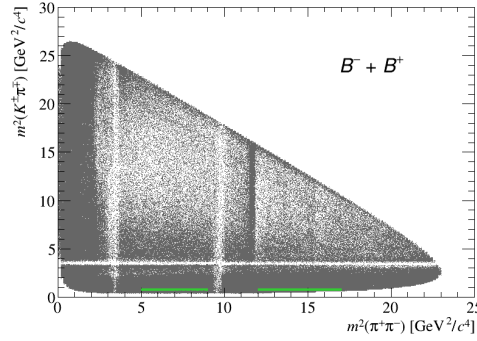
TABLE 5.6: Quadratic fit parameters over  $B^+$  and  $B^-$  yield distributions for  $K^*(892)^0$  in  $B^\pm \rightarrow K^\pm\pi^+\pi^-$  as shown in Figure 5.7(b).

Finally, the  $CP$  asymmetry for the vector resonance was measured to be

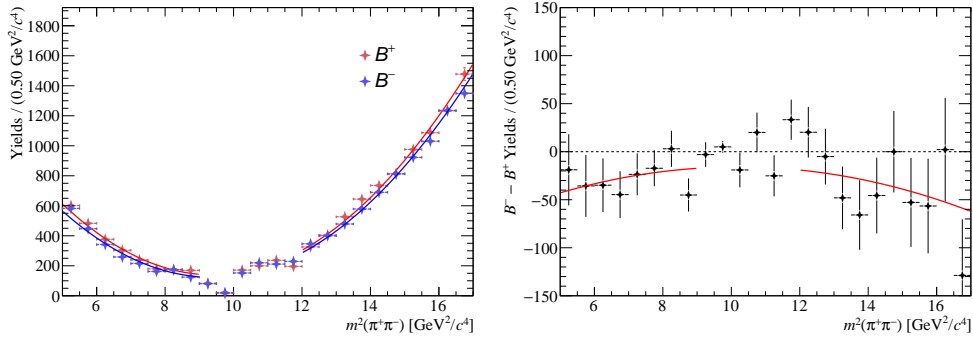
$$\mathcal{A}_{CP}^{K^*(892)^0} = (-1.2 \pm 1.8)\%,$$

which is compatible with a null  $A_{CP}$ .

This measurement can be compared with the one obtained by the BaBar experiment for this channel [99]:  $\mathcal{A}_{CP}^{K^*(892)^0} = (3.2 \pm 5.2 \pm 1.1)\%$ . The results are compatible with each other within  $0.8\sigma$ . Also, in this scenario, our measurements are more precise.



(a) Selected  $B^\pm \rightarrow K^\pm \pi^+ \pi^-$  Dalitz plot region in green.

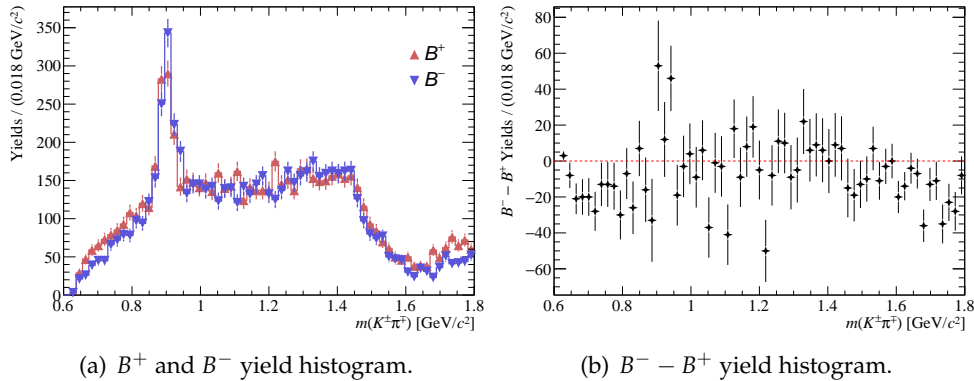


(b)  $B^+$  and  $B^-$  yield distributions over  $s_\perp$  and (c)  $B^- - B^+$  yield histogram and its quadratic fit.

FIGURE 5.7: Measurement plots for  $K^*(892)^0$  in  $B^\pm \rightarrow K^\pm \pi^+ \pi^-$ .

### 5.3.3 $B^\pm \rightarrow \pi^\pm K^+ K^-$ decay

From the  $B^\pm$  yield distributions over  $m(K^\pm \pi^\mp)$  in  $B^\pm \rightarrow \pi^\pm K^+ K^-$  decays in Figure 5.8(a), one might spot the existence of a peaking structure, which corresponds to our mass range of interest due to the presence of the  $K^*(892)^0$  vector, and also the presence the  $K_0^*(1430)$  scalar. In Figure 5.8(b), one may see the  $B^- - B^+$  yield histogram, which emphasises raw charge asymmetry.



(a)  $B^+$  and  $B^-$  yield histogram.

(b)  $B^- - B^+$  yield histogram.

FIGURE 5.8: Yield distributions over  $m(K^\pm \pi^\mp)$  for  $K^*(892)^0$  in  $B^\pm \rightarrow \pi^\pm K^+ K^-$ .

For  $B^+ \rightarrow \bar{K}^*(892)^0 K^+$  and its  $CP$ -conjugate channel, a  $50 \text{ MeV}/c^2$  mass window centred around mass in  $m(K^\pm \pi^\mp)$  and a  $[10, 25] \text{ GeV}^2/c^4$  fit region in  $m^2(K^+ K^-)$  were chosen. The events selected by the mass window, projected over  $s_\perp$ , are highlighted in green in Figure 5.9(a). The change in minimum mass in comparison with the previous channels is due to the phase-space reduction in this case for lower masses. Figure 5.9(b) illustrates the quadratic fit performed over the  $B^+$  and  $B^-$  acceptance-corrected yield distributions that extracted the parameters reported in Table 5.7. Lastly, Figure 5.9(c) displays the  $B^- - B^+$  yield distribution and its quadratic fit.

Fit Parameter	$B^+$	$B^-$
$p_0$	$440 \pm 36$	$515 \pm 37$
$p_1$	$-52.1 \pm 4.3$	$-56.9 \pm 4.3$
$p_2$	$1.602 \pm 0.127$	$1.620 \pm 0.123$
$\chi^2/\text{ndf}$	0.74	1.04

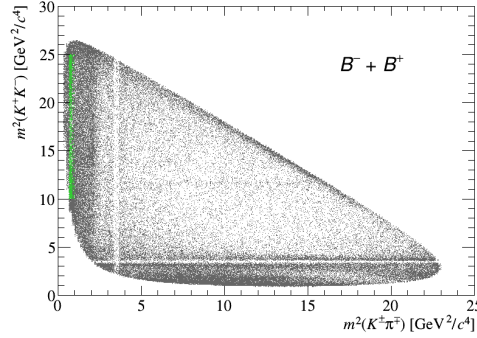
TABLE 5.7: Quadratic fit parameters over  $B^+$  and  $B^-$  yield distributions for  $K^*(892)^0$  in  $B^\pm \rightarrow \pi^\pm K^+ K^-$  as shown in Figure 5.9(b).

Finally, the  $CP$  asymmetry for the vector resonance was measured to be

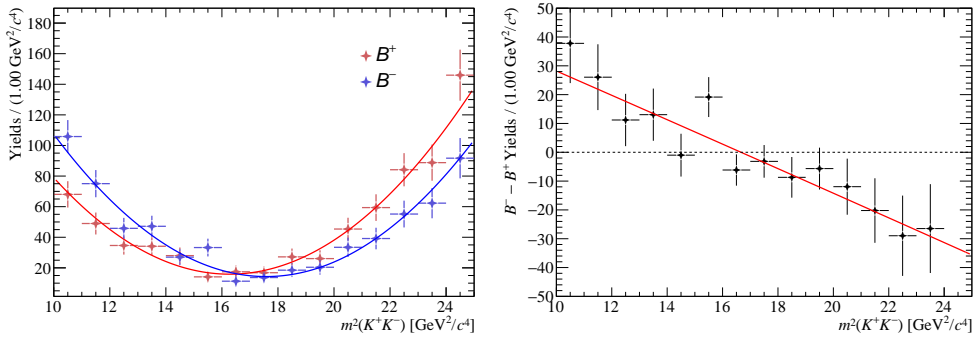
$$\mathcal{A}_{CP}^{K^*(892)^0} = (1.8 \pm 5.4)\%,$$

which is compatible with a null  $A_{CP}$ .

This measurement can be compared with the one obtained by the LHCb analysis amplitude for this channel [22]:  $\mathcal{A}_{CP}^{K^*(892)^0} = (12.3 \pm 8.7 \pm 4.5)\%$ . The results are compatible with each other within  $1.1\sigma$ . Also, in this scenario, our measurements are more precise.



(a) Selected  $B^\pm \rightarrow \pi^\pm K^+ K^-$  Dalitz plot region in green.



(b)  $B^+$  and  $B^-$  yield distributions over  $s_\perp$  and (c)  $B^- - B^+$  yield histogram and its quadratic fit.

FIGURE 5.9: Measurements plots for  $K^*(892)^0$  in  $B^\pm \rightarrow \pi^\pm K^+ K^-$ .

### 5.3.4 $B^\pm \rightarrow K^\pm K^+ K^-$ decay

From the  $B^\pm$  yield distributions over  $m(K^+K^-)$  in  $B^\pm \rightarrow K^\pm K^+ K^-$  decays in Figure 5.10(a), one might spot the existence of a peaking structures, which corresponds to our mass range of interest due to the presence of the  $\phi(1020)$  vector. In Figure 5.10(b), one may see the  $B^- - B^+$  yield histogram, which emphasises raw charge asymmetry.

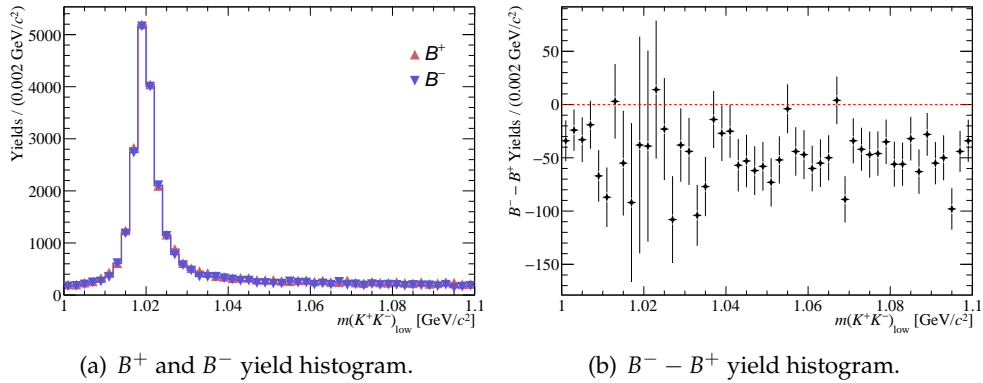


FIGURE 5.10: Yield distributions over  $m(K^+K^-)_{\text{low}}$  for  $\phi(1020)$  in  $B^\pm \rightarrow K^\pm K^+ K^-$ .

For  $B^+ \rightarrow \phi(1020)K^+$  and its  $CP$ -conjugate channel, a  $5 \text{ MeV}/c^2$  mass window centred around mass in  $m(K^+K^-)_{\text{low}}$  and a  $[12, 16.5] \text{ GeV}^2/c^4$  fit region in  $m^2(K^+K^-)_{\text{high}}$  were chosen. This region was chosen for the same reason as the  $K^*(892)^0$  in  $B^\pm \rightarrow K^\pm \pi^+ \pi^-$ , regarding undesired resonances. The events selected by the mass window, projected over  $s_\perp$ , are highlighted in green in Figure 5.11(a).

Figure 5.11(b) illustrates the quadratic fit performed over the  $B^+$  and  $B^-$  acceptance-corrected yield distributions that extracted the parameters reported in Table 5.8. Lastly, Figure 5.11(c) displays the  $B^- - B^+$  yield distribution and its quadratic fit.

Fit Parameter	$B^+$	$B^-$
$p_0$	$15698 \pm 14$	$15841 \pm 12$
$p_1$	$-2324.5 \pm 1.4$	$-2344.3 \pm 1.1$
$p_2$	$86.092 \pm 0.076$	$86.752 \pm 0.064$
$\chi^2/\text{ndf}$	0.73	0.76

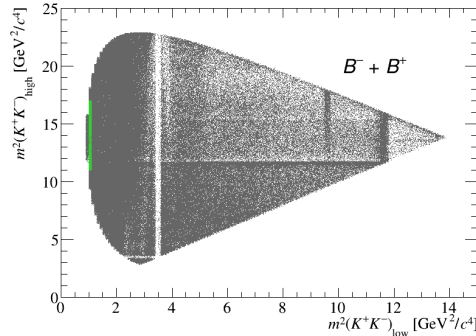
TABLE 5.8: Quadratic fit parameters over  $B^+$  and  $B^-$  yield distributions for  $\phi(1020)$  in  $B^\pm \rightarrow K^\pm K^+ K^-$  as shown in Figure 5.11(b).

Finally, the  $CP$  asymmetry for the vector resonance was measured to be

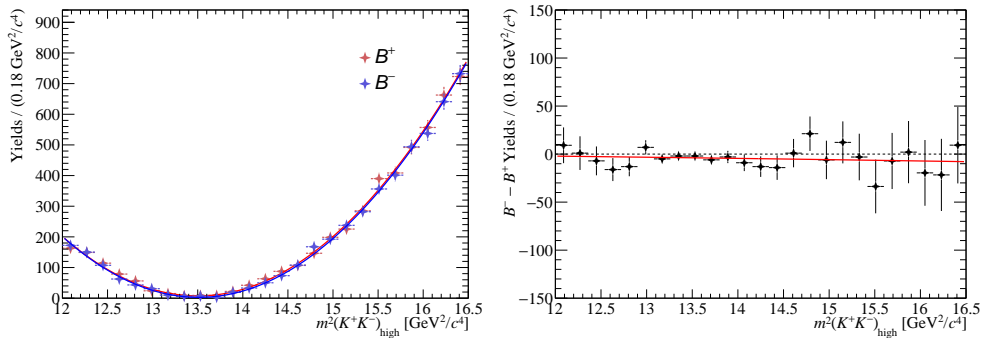
$$\mathcal{A}_{CP}^{\phi(1020)} = (1.7 \pm 0.7)\%.$$

which is consistent with a null  $A_{CP}$ .

This measurement can be compared with the one obtained by the BaBar experiment for this channel [100]:  $\mathcal{A}_{CP}^{\phi(1020)} = (12.8 \pm 4.4 \pm 1.3)\%$ . One might say there is some tension between the asymmetries, since the BaBar measurement differs from ours by  $2.4\sigma$ , however it does not represent an  $\mathcal{A}_{CP}^V$  observation.



(a) Selected  $B^\pm \rightarrow K^\pm K^+ K^-$  Dalitz plot region in green.



(b)  $B^+$  and  $B^-$  yield distributions over  $s_\perp$  and (c)  $B^- - B^+$  yield histogram and its quadratic fit.

FIGURE 5.11: Measurement plots for  $\phi(1020)$  in  $B^\pm \rightarrow K^\pm K^+ K^-$ .

## 5.4 Summary and Considerations

Table 5.9 summarizes the  $\mathcal{A}_{CP}^V$  measurements obtained from Equation 5.11 out of  $B \rightarrow PV$  decays by exploiting the model-independent method introduced in Subsection 5.2. These measurements were performed through quadratic fits to the  $B^+$  and  $B^-$  yield distributions over orthogonal Dalitz variable. The number of events situated inside the fit region, namely, the integral, for each case is reported in Table 5.10. The systematic errors for these measurements are planned to be soon evaluated.

At first glance, it is outstanding that, following the prediction from  $CPT$  constraint [95], the measured vector  $CP$ -asymmetries were compatible with zero, with the exception of  $\rho(770)^0$  in the  $B^\pm \rightarrow K^\pm \pi^+ \pi^-$  decay, which differs from zero by  $10.9\sigma$ . Such conjecture claims that  $CP$  should be suppressed in  $B \rightarrow PV$  except

Decay channel	Vector	Measured $\mathcal{A}_{CP}^V$	$\mathcal{A}_{CP}^V$ (experiment)
$B^\pm \rightarrow \pi^\pm \pi^+ \pi^-$	$\rho(770)^0$	$-0.001 \pm 0.014$	$+0.007 \pm 0.011 \pm 0.016$ (LHCb)
$B^\pm \rightarrow K^\pm \pi^+ \pi^-$	$\rho(770)^0$	$+0.153 \pm 0.014$	$+0.44 \pm 0.10 \pm 0.04$ (BaBar)
	$K^*(892)^0$	$-0.012 \pm 0.018$	$+0.032 \pm 0.052 \pm 0.011$ (BaBar)
$B^\pm \rightarrow \pi^\pm K^+ K^-$	$K^*(892)^0$	$+0.014 \pm 0.053$	$+0.123 \pm 0.087 \pm 0.045$ (LHCb)
$B^\pm \rightarrow K^\pm K^+ K^-$	$\phi(1020)$	$+0.012 \pm 0.010$	$+0.128 \pm 0.044 \pm 0.013$ (BaBar)

TABLE 5.9: Summary of  $CP$ -asymmetry measurements for the vector resonance channels and their associated final-state  $B^\pm \rightarrow h^\pm h^+ h^-$  decays.

Decay channel	Vector Resonance	$B^+$ Integral	$B^-$ Integral	$B^\pm$ Integral
$B^\pm \rightarrow \pi^\pm \pi^+ \pi^-$	$\rho(770)^0$	8060	7613	15673
$B^\pm \rightarrow K^\pm \pi^+ \pi^-$	$\rho(770)^0$	6035	7443	13478
	$K^*(892)^0$	11816	11219	23035
$B^\pm \rightarrow \pi^\pm K^+ K^-$	$K^*(892)^0$	751	689	1440
$B^\pm \rightarrow K^\pm K^+ K^-$	$\phi(1020)$	9673	9512	19185

TABLE 5.10: Selected event statistics for the quadratic fit histograms.

for FSI, such as rescattering effects with the bachelor particle. A distinct feature of  $\rho(770)^0$  in  $B^\pm \rightarrow K^\pm \pi^+ \pi^-$  is the vector contribution being smaller than the scalar one, as seen in Figure 5.4(a), whereas the other way around is true for the rest of the studied cases. Regarding the statistical errors, except for  $\rho(770)^0$  in  $B^\pm \rightarrow K^\pm \pi^+ \pi^-$  and  $K^*(892)^0$  in  $B^\pm \rightarrow \pi^\pm K^+ K^-$ , they reinforce the absence of  $CP$  violation, since they restrain the  $\mathcal{A}_{CP}^V$  measurements to a few percent.

Comparison between our results and previous measurements can be made, as reported by Table 5.9, where the first uncertainty is statistical, and the second, systematic. The BaBar experiment provides references for  $B^\pm \rightarrow K^\pm K^+ K^-$  [100] and  $B^\pm \rightarrow K^\pm \pi^+ \pi^-$  [99] decays, whereas the LHCb supplies amplitude-analysis measurements for  $B^\pm \rightarrow \pi^\pm \pi^+ \pi^-$  [98] and  $B^\pm \rightarrow \pi^\pm K^+ K^-$  [22].

Overall, the main conclusion is that the method is trustworthy, effective and qualified to be applied to data, since it provided  $\mathcal{A}_{CP}^V$  measurements with competitive errors.

# Conclusion

In this thesis, new results and studies on the charge asymmetry of  $B$  meson decays, which are a good laboratory to investigate  $CP$ -violation mechanisms, were presented. The analysis was focused on charmless three-body  $B^\pm$  decays:  $B^\pm \rightarrow K^\pm \pi^+ \pi^-$ ,  $B^\pm \rightarrow K^\pm K^+ K^-$ ,  $B^\pm \rightarrow \pi^\pm \pi^+ \pi^-$  and  $B^\pm \rightarrow \pi^\pm K^+ K^-$ .

The  $B$  factory responsible for providing the data was the LHCb experiment. This data set corresponds to an integrated luminosity of  $5.9 \text{ fb}^{-1}$  acquired during Run 2 (2015-2018) of LHC, when  $pp$  collisions were produced at a centre-of-mass energy of 13 TeV. The  $B^\pm \rightarrow h^\pm h^+ h^-$  candidates were selected through inclusive selection criteria based on decay topology and kinematics. The background contributions were then reduced by using a multivariate analysis and particle identification requirements. This selection process allowed the  $B^\pm \rightarrow h^\pm h^+ h^-$  data samples to undergo two analyses.

First, a simultaneous fit to  $B^+$  and  $B^-$  invariant-mass distributions was performed in each decay channel in order to determine the number of  $B$  candidates and the raw charge asymmetry. For a single channel, these yields corresponded up to 5 times the number of candidates obtained by the previous LHCb measurement [21]. The inclusive  $CP$  asymmetry was finally obtained by correcting the raw asymmetry from acceptance effects and experimentally-introduced asymmetries. The measured  $CP$  asymmetries are listed below:

Decay channel	$\mathcal{A}_{CP} \pm \sigma_{\text{stat}}$
$B^\pm \rightarrow K^\pm \pi^+ \pi^-$	$+0.003 \pm 0.003$
$B^\pm \rightarrow K^\pm K^+ K^-$	$-0.045 \pm 0.003$
$B^\pm \rightarrow \pi^\pm \pi^+ \pi^-$	$+0.082 \pm 0.005$
$B^\pm \rightarrow \pi^\pm K^+ K^-$	$-0.114 \pm 0.007$

The measurement significances should be appreciated as they surpass  $5\sigma$  for  $B^\pm \rightarrow K^\pm K^+ K^-$ ,  $B^\pm \rightarrow \pi^\pm \pi^+ \pi^-$  and  $B^\pm \rightarrow \pi^\pm K^+ K^-$ , which is indicative of an observation of  $CP$  violation for these channels; particularly, it represents an inaugural result for  $B^\pm \rightarrow K^\pm K^+ K^-$  and  $B^\pm \rightarrow \pi^\pm \pi^+ \pi^-$  decays. Also, the  $\mathcal{A}_{CP}$  obtained were compatible within up to  $3\sigma$  with the previous measurement (Eqs. 1.25).

Second, a simple model-independent method was employed to extract  $CP$  asymmetries from  $B \rightarrow PV$  decays without the expense of standard procedures such as amplitude analyses. The measured  $CP$  asymmetries are listed below:

Decay channel	Vector Resonance	$\mathcal{A}_{CP}^V \pm \sigma_{\text{stat}}$
$B^\pm \rightarrow \pi^\pm \pi^+ \pi^-$	$\rho(770)^0$	$-0.011 \pm 0.017$
$B^\pm \rightarrow K^\pm \pi^+ \pi^-$	$\rho(770)^0$	$+0.143 \pm 0.019$
	$K^*(892)^0$	$-0.024 \pm 0.019$
$B^\pm \rightarrow \pi^\pm K^+ K^-$	$K^*(892)^0$	$+0.001 \pm 0.055$
$B^\pm \rightarrow K^\pm K^+ K^-$	$\phi(1020)$	$-0.001 \pm 0.011$

The method's concept benefits from the angular distribution of a vector resonance in the DP and the feature that such low-mass vector meson generally shares a phase-space proximity region with a scalar meson.

It is remarkable that the measured vector *CP*-asymmetries were mostly compatible with zero following the *CPT* constraint. Then, one might conclude, in the case of  $\rho(770)^0$  in the  $B^\pm \rightarrow K^\pm \pi^+ \pi^-$  decay, that rescattering processes with the bachelor particle must take place. Overall, the method proved to be satisfactory as it produced  $\mathcal{A}_{CP}^V$  measurements with competitive errors, and reliable, since it presented compatible results in comparison with standard analysis amplitude approaches.

The measurements presented in this thesis constitute a preliminary result of the analysis that has been performed by the LHCb Charmless Three-Body *B*-Decay Rio analysis group, which is carried out by a research team from CBPF and other institutions, such as UFRJ, UFTM and UNAH. The analysis note for the LHCb collaboration is in preparation, having already been examined by the referees, and the release is expected for the near future. It will also include the evaluation of the systematic errors as well as an inspection of patterns of localised  $\mathcal{A}_{CP}$  together with measurements for integrated asymmetries in these regions so as to relate them to the amplitude analyses [22, 23] of some of these modes.

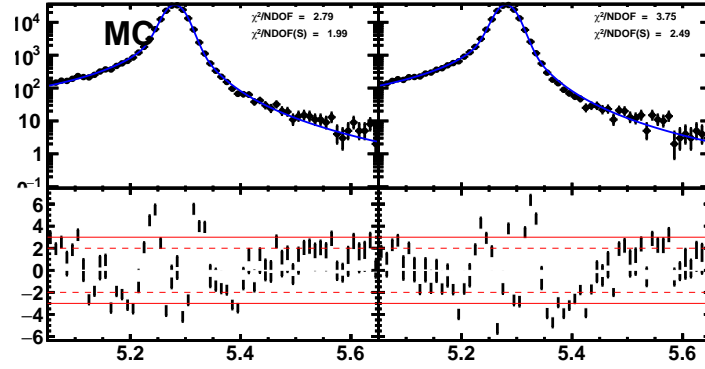
## Appendix A

# Invariant-Mass Fit

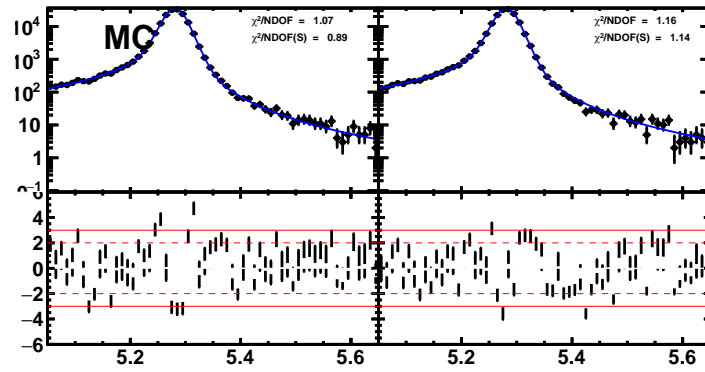
This appendix serves as a complement to Section 4.2, which presents the invariant-mass fit to the  $B^-$  and  $B^+$  data samples.

### A.1 Signal Fit-Model Study

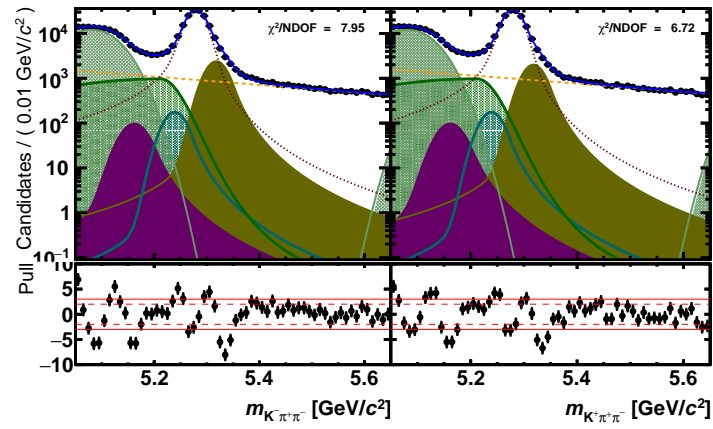
This section exhibits part of the conducted studies that led to the inclusion of a Gaussian distribution to the double Crystal Ball function as a signal fit model, mentioned in Subsection 4.2.2. At the time the examination was advancing, the only data samples available were from 2015, 2016 and 2017. The study consisted of alternating the signal fit models between Equations 4.12 (dCB) and 4.13 (dCB + Gaussian) to all four  $B^\pm \rightarrow h^\pm h^+ h^-$  channels for comparison effects. Figures A.1–A.4 display the comparison invariant-mass fits for each channel between signal fit models before and after the inclusion of a Gaussian distribution to a double Crystal Ball function. The improvement in the fit quality is evident both for the  $\chi^2/\text{ndf}$  parameters, which are now closer to 1, as for the stability in pull distributions. Still, the signal yields estimated by the fits and their errors do not fluctuate considerably from including a Gaussian distribution.



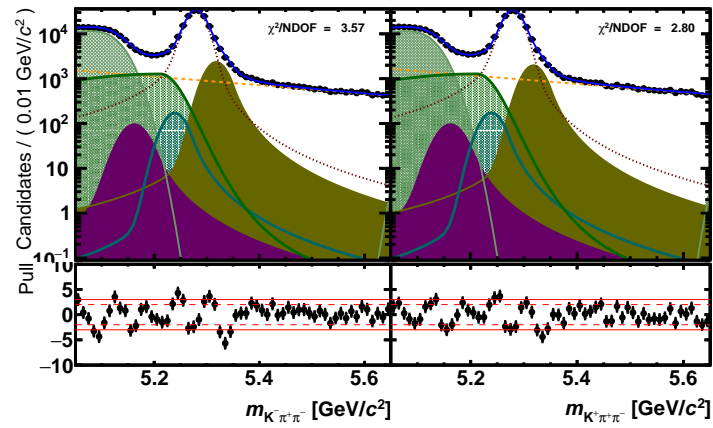
(a) dCB: MC fit



(b) dCB + Gaussian: MC fit

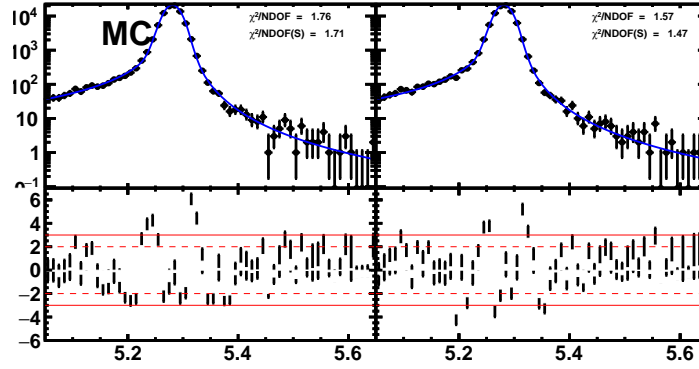


(c) dCB: data fit

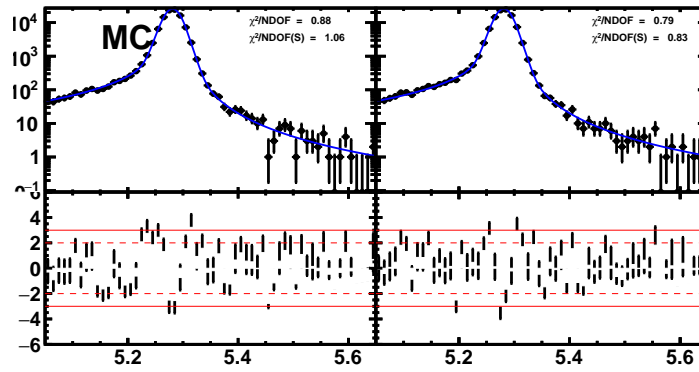


(d) dCB + Gaussian: data fit

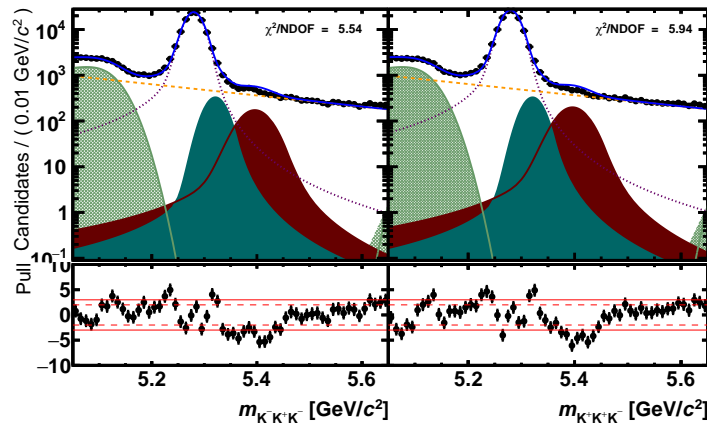
FIGURE A.1:  $B^{\pm} \rightarrow K^{\pm}\pi^+\pi^-$  comparison invariant-mass plots between signal fit models: MC and data fits in logarithmic scale before and after the inclusion of a Gaussian distribution to a dCB function.



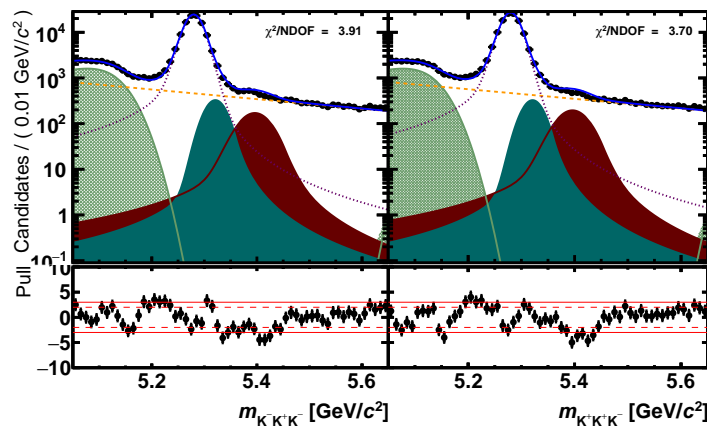
(a) dCB: MC fit



(b) dCB + Gaussian: MC fit

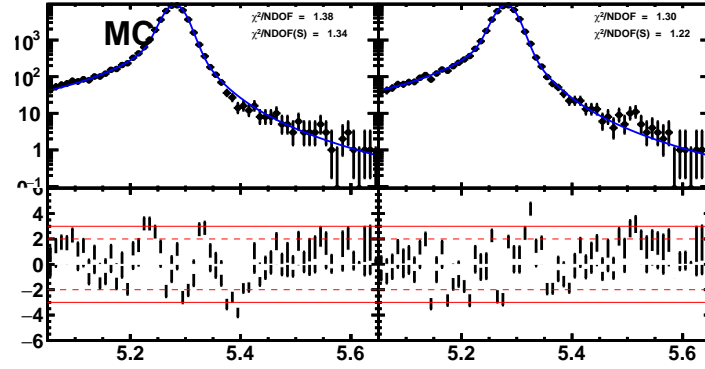


(c) dCB: data fit

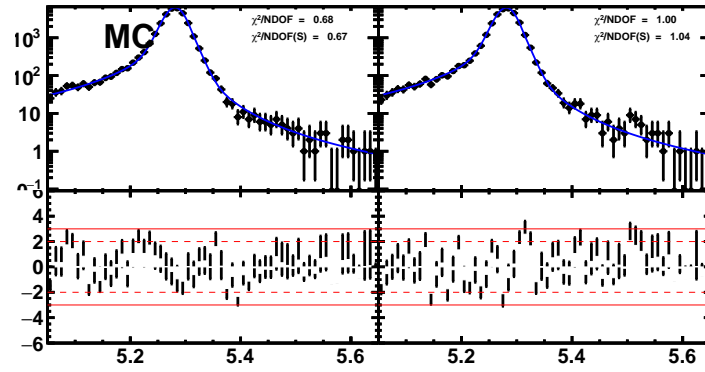


(d) dCB + Gaussian: data fit

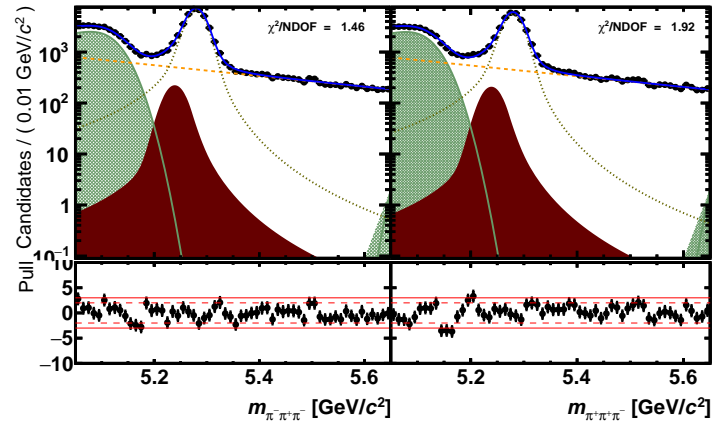
FIGURE A.2:  $B^\pm \rightarrow K^\pm K^+ K^-$  comparison invariant-mass plots between signal fit models: MC and data fits in logarithmic scale before and after the inclusion of a Gaussian distribution to a dCB function.



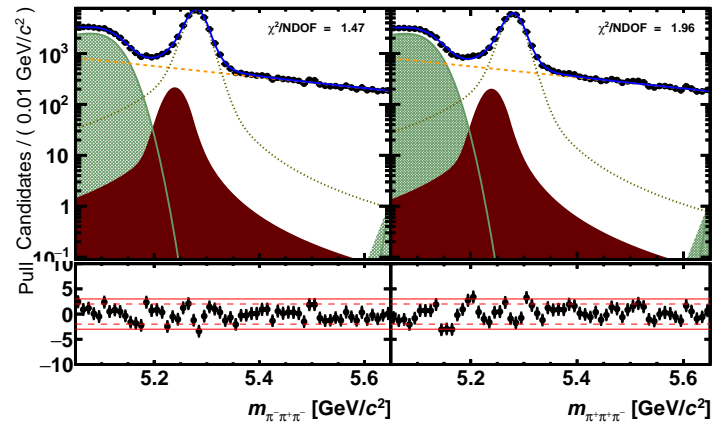
(a) dCB: MC fit



(b) dCB + Gaussian: MC fit

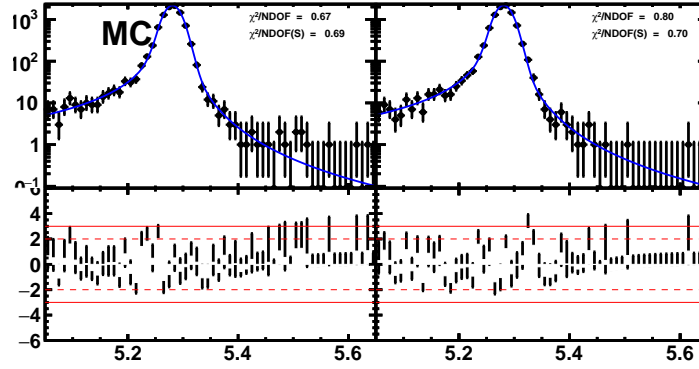


(c) dCB: data fit

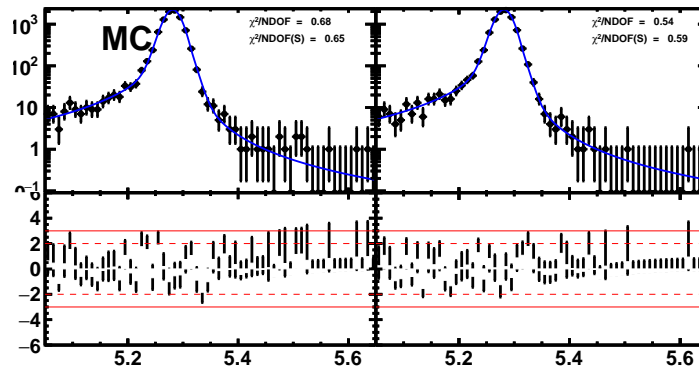


(d) dCB + Gaussian: data fit

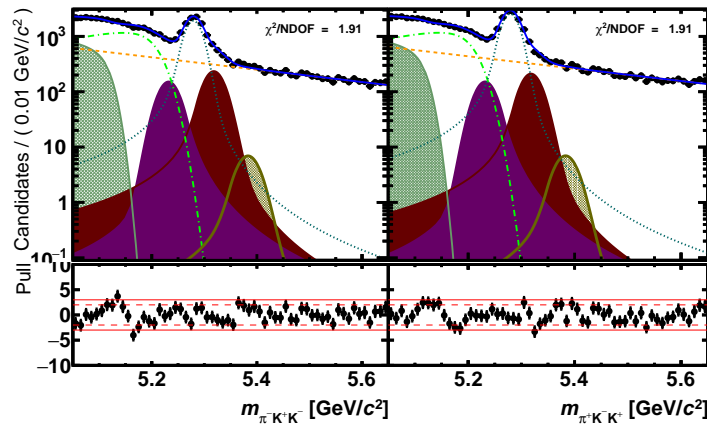
FIGURE A.3:  $B^\pm \rightarrow \pi^\pm \pi^+ \pi^-$  comparison invariant-mass plots between signal fit models: MC and data fits in logarithmic scale before and after the inclusion of a Gaussian distribution to a dCB function.



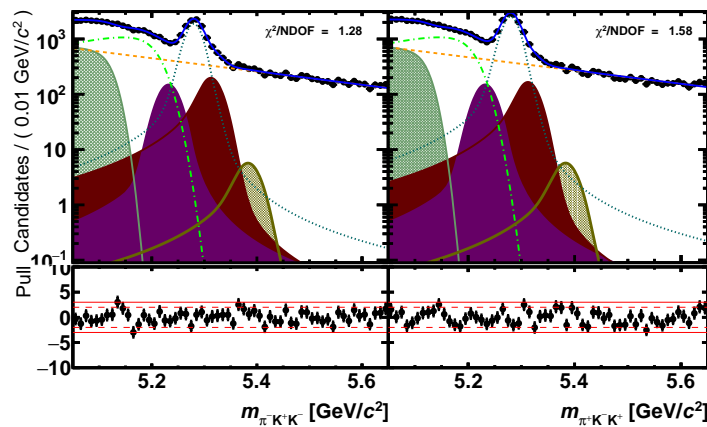
(a) dCB: MC fit



(b) dCB + Gaussian: MC fit



(c) dCB: data fit



(d) dCB + Gaussian: data fit

FIGURE A.4:  $B^\pm \rightarrow \pi^\pm K^+ K^-$  comparison invariant-mass plots between signal fit models: MC and data fits in logarithmic scale before and after the inclusion of a Gaussian distribution to a dCB function.

## A.2 Complementary Mass-Fit Results

This section reports complementary invariant-mass fit results to the  $B^-$  and  $B^+$  data samples presented in Subsection 4.2.3. Table A.1 displays the parameters extracted from the mass-fit distributions of data samples, including background contributions. Also, Table A.2 illuminates what the background components labelled as ‘Reflections 3-5’ in Table A.1 translate to in each channel. Finally, Figures A.5-A.8 show the plots for MC and data sample mass fits in the logarithmic scale along with pull plots for  $B^\pm \rightarrow K^\pm \pi^+ \pi^-$ ,  $B^\pm \rightarrow K^\pm K^+ K^-$ ,  $B^\pm \rightarrow \pi^\pm \pi^+ \pi^-$  and  $B^\pm \rightarrow \pi^\pm K^+ K^-$  decays.

TABLE A.1: Parameters extracted from the invariant-mass fit distributions of data samples. The numbers tagged by a ‘(C)’ were fixed in the corresponding fit.

Parameter	$B^\pm \rightarrow K^\pm \pi^+ \pi^-$	$B^\pm \rightarrow K^\pm K^+ K^-$	$B^\pm \rightarrow \pi^\pm \pi^+ \pi^-$	$B^\pm \rightarrow \pi^\pm K^+ K^-$
Signal component				
$m_0[\text{MeV}/c^2]$	5277.6 $\pm 0.065077$	5280.9 (C)	5280.8 (C)	5281.1 (C)
$(m_0)_2[\text{MeV}/c^2]$	5292.3 $\pm 0.19476$	—	—	—
$(m_0)_3[\text{MeV}/c^2]$	5271.1 $\pm 0.38917$	—	—	—
$c(m_0)_{MC}[\text{MeV}/c^2]$	—	0.99979 $\pm 0.0000063788$	0.99980 $\pm 0.000015050$	0.99976 $\pm 0.000026964$
$\sigma[\text{MeV}/c^2]$	14.620 (C)	13.626 (C)	16.407 (C)	14.014 (C)
$\sigma_3[\text{MeV}/c^2]$	25.080 (C)	—	—	—
$\sigma_G[\text{MeV}/c^2]_G$	15.169 (C)	17.963 (C)	25.175 (C)	19.007 (C)
$c(\sigma)_{MC}[\text{MeV}/c^2]$	0.0000 (C)	1.1139 $\pm 0.0020253$	1.0119 $\pm 0.0044818$	1.0960 $\pm 0.0098867$
$a_1$	0.86658 (C)	1.2750 (C)	0.83638 (C)	0.82345 (C)
$n_1$	1.7563 (C)	1.6314 (C)	1.9244 (C)	1.9533 (C)
$a_2$	-2.01428 (C)	-1.81696 (C)	-1.72397 (C)	-1.97014 (C)
$n_2$	1.8641 (C)	2.5892 (C)	2.5095 (C)	2.1858 (C)
$f_{Gaus}$	0.57399 (C)	0.37001 (C)	0.23304 (C)	0.36058 (C)
$f_{CBs}$	0.57032 (C)	0.43903 (C)	0.39616 (C)	0.31880 (C)
$A_{RAW}$	0.0055078 $\pm (-0.0015776,$ $\pm +0.0015798)$	-0.0512601 $\pm (-0.0017842,$ $\pm +0.0017847)$	0.091036 $\pm (-0.0036328,$ $\pm +0.0036301)$	-0.132273 $\pm (-0.0068015,$ $\pm +0.0068183)$
$N_{sig}$	492574 $\pm 869.86$	355162 $\pm 650.43$	101056 $\pm 404.21$	32832 $\pm 300.33$
Combinatorial component				
shift	5080.0 (C)	5200.0 (C)	5083.0 (C)	5083.0 (C)
$b$	-0.00268525 $\pm 0.000057603$	-0.00295643 $\pm 0.000035042$	-0.00258079 $\pm 0.000039994$	-0.00271109 $\pm 0.000084702$
$A_{comb}$	-0.0177866 $\pm 0.0037983$	-0.0246597 $\pm 0.0050476$	-0.00859032 $\pm 0.0053627$	-0.0122181 $\pm 0.0062923$
$N_{comb}$	192964 $\pm 2670.0$	99283 $\pm 787.92$	80844 $\pm 662.32$	61965 $\pm 1190.8$
$B \rightarrow 4\text{-body (partially-reconstructed component)}$				
meanRes	0.0000 (C)	0.0000 (C)	0.0000 (C)	0.0000 (C)
$\sigma [\text{MeV}/c^2]$	15.143 $\pm 0.37068$	18.252 (C)	26.020 (C)	15.153 (C)
$m_t [\text{MeV}/c^2]$	5147.6 $\pm 0.45955$	5149.0 (C)	5135.3 (C)	5133.6 (C)
$c$	-13.0419 $\pm 1.0646$	-13.3033 (C)	-20.7589 (C)	-9.38510 (C)

Continued on next page

Table A.1 – Continued from previous page

	$B^\pm \rightarrow K^\pm \pi^+ \pi^-$	$B^\pm \rightarrow K^\pm K^+ K^-$	$B^\pm \rightarrow \pi^\pm \pi^+ \pi^-$	$B^\pm \rightarrow \pi^\pm K^+ K^-$
$p$	0.43842 $\pm 0.021780$	0.38303 (c)	0.25885 (c)	0.41695 (c)
$N_{bkg1}$	290234 $\pm 1157.3$	37793 $\pm 485.43$	64389 $\pm 471.83$	15764 $\pm 527.02$
$A_{bkg}$	-0.00305104 $\pm 0.0023122$	0.027179 $\pm 0.0084691$	0.028217 $\pm 0.0052198$	-0.0298699 $\pm 0.016590$
$B_s^0 \rightarrow 4\text{-body}$ (partially-reconstructed component)				
meanRes	–	–	–	0.0000 (c)
$\sigma$ [MeV/ $c^2$ ]	–	–	–	22.000 (c)
$m_t$ [MeV/ $c^2$ ]	–	–	–	5220.7 (c)
$c$	–	–	–	-18.7998 (c)
$p$	–	–	–	0.50000 (c)
$N_{bkg2}$	–	–	–	41698 $\pm 2623.1$
$A_{bkg}$	–	–	–	0.0000 (c)
Reflection 3				
$m_0$ [MeV/ $c^2$ ]	5317.0 (c)	5385.0 (c)	5239.0 (c)	5321.0 (c)
$\sigma$ [MeV/ $c^2$ ]	20.000 (c)	22.000 (c)	21.000 (c)	20.000 (c)
$a_1$	1.7000 (c)	1.4000 (c)	0.22000 (c)	1.7000 (c)
$a_2$	-1.11000 (c)	-0.490000 (c)	-2.04000 (c)	-0.300000 (c)
$n_1$	1.5900 (c)	1.6900 (c)	0.18000 (c)	1.3400 (c)
$n_2$	1.9200 (c)	2.5700 (c)	2.7500 (c)	18.380 (c)
$f_{CB}$	0.61000 (c)	0.35000 (c)	0.67000 (c)	0.54000 (c)
$Fraction$ [%]	0.090323 $\pm 0.0015827$	0.0030413 $\pm 0.00052996$	0.036000 (c)	0.096000 (c)
$A_{bkg}$	0.058000 (c)	0.0000 (c)	0.0000 (c)	0.0000 (c)
Reflection 4				
$m_0$ [MeV/ $c^2$ ]	5164.0 (c)	5319.0 (c)	–	5232.0 (c)
$\sigma$ [MeV/ $c^2$ ]	25.000 (c)	20.000 (c)	–	21.000 (c)
$a_1$	0.56000 (c)	2.2000 (c)	–	0.070000 (c)
$a_2$	-2.45000 (c)	-0.790000 (c)	–	-2.23000 (c)
$n_1$	0.0000 (c)	1.0400 (c)	–	19.400 (c)
$n_2$	2.6400 (c)	2.7100 (c)	–	1.6300 (c)
$f_{CB}$	0.52000 (c)	0.62000 (c)	–	0.86000 (c)
$Fraction$ [%]	0.058660 $\pm 0.0033157$	0.018300 (c)	–	0.085000 (c)
$A_{bkg}$	-0.0360000 (c)	0.0000 (c)	–	0.0000 (c)
Reflection 5				
$m_0$ [MeV/ $c^2$ ]	5233.0 (c)	–	–	5379.0 (c)
$\sigma$ [MeV/ $c^2$ ]	22.000 (c)	–	–	16.200 (c)
$a_1$	0.57000 (c)	–	–	1.2800 (c)
$a_2$	-2.08000 (c)	–	–	-0.170000 (c)
$n_1$	0.34000 (c)	–	–	1.8400 (c)
$n_2$	1.3000 (c)	–	–	2.7000 (c)
$f_{CB}$	0.89000 (c)	–	–	0.39000 (c)
$Fraction$ [%]	0.0060000 (c)	–	–	0.0040000 (c)
$A_{bkg}$	-0.123000 (c)	–	–	0.0000 (c)
$B^\pm \rightarrow \eta'(\rho^0 \gamma) K^\pm$				
$m_0$ [MeV/ $c^2$ ]	5214.0 (c)	–	–	–
$\sigma$ [MeV/ $c^2$ ]	31.000 (c)	–	–	–
$a_1$	0.055000 (c)	–	–	–
$a_2$	-0.300000 (c)	–	–	–
$n_1$	20.000 (c)	–	–	–

Continued on next page

Table A.1 – Continued from previous page

	$B^\pm \rightarrow K^\pm \pi^+ \pi^-$	$B^\pm \rightarrow K^\pm K^+ K^-$	$B^\pm \rightarrow \pi^\pm \pi^+ \pi^-$	$B^\pm \rightarrow \pi^\pm K^+ K^-$
$n_2$	20.000 (C)	—	—	—
$f_{CB}$	0.99500 (C)	—	—	—
Fraction [%]	0.11360 (C)	—	—	—
$A_{bkg}$	0.0000 (C)	—	—	—
$B_s^0 \rightarrow D_s^- \pi^+$				
meanRes	—	—	—	0.0000 (C)
$\sigma$ [MeV/c <sup>2</sup> ]	—	—	—	22.147 (C)
$m_t$ [MeV/c <sup>2</sup> ]	—	—	—	5217.7 (C)
$c$	—	—	—	-9.79980 (C)
$p$	—	—	—	—
$N_{bkg2}$	—	—	—	8951.5 ±2455.5
$A_{bkg}$	—	—	—	0.0000 (C)

Component	$B^\pm \rightarrow K^\pm \pi^+ \pi^-$	$B^\pm \rightarrow K^\pm K^+ K^-$	$B^\pm \rightarrow \pi^\pm \pi^+ \pi^-$	$B^\pm \rightarrow \pi^\pm K^+ K^-$
Reflection 3	$B^\pm \rightarrow \pi^\pm \pi^+ \pi^-$	$B^\pm \rightarrow K^\pm \pi^+ \pi^-$	$B^\pm \rightarrow K^\pm \pi^+ \pi^-$	$B^\pm \rightarrow K^\pm \pi^+ \pi^-$
Reflection 4	$B^\pm \rightarrow K^\pm K^+ K^-$	$B^\pm \rightarrow \pi^\pm K^+ K^-$	-	$B^\pm \rightarrow K^\pm K^+ K^-$
Reflection 5	$B^\pm \rightarrow \pi^\pm K^+ K^-$	-	-	$B^\pm \rightarrow \pi^\pm \pi^+ \pi^-$

TABLE A.2: Correspondent reflection component to each channel as presented in Table A.1.

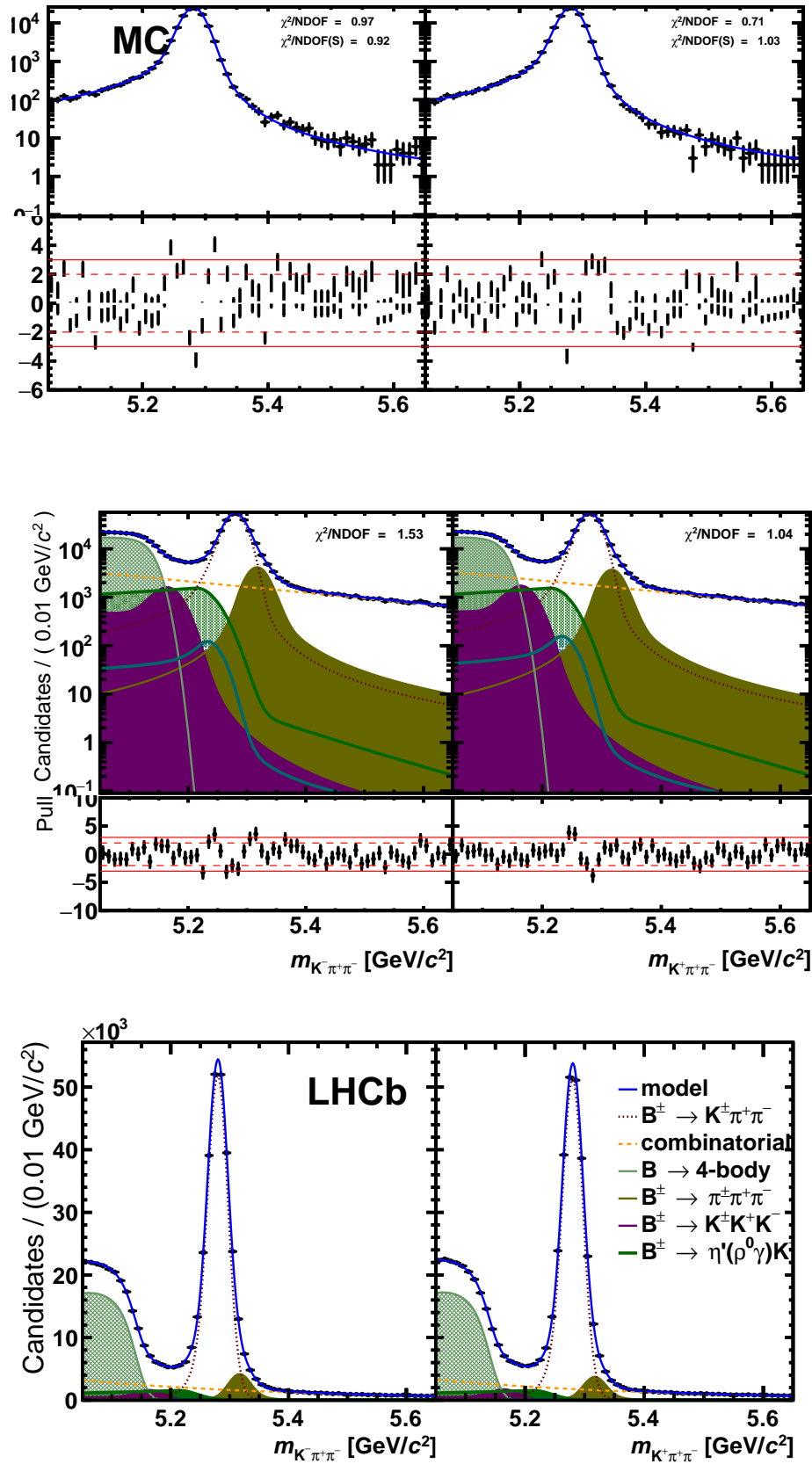


FIGURE A.5: Additional invariant-mass fit plots for  $B^\pm \rightarrow K^\pm \pi^+ \pi^-$ : (top) MC sample in logarithmic scale, with pull; (middle) data sample in logarithmic scale, with pull; (bottom) data sample plot.

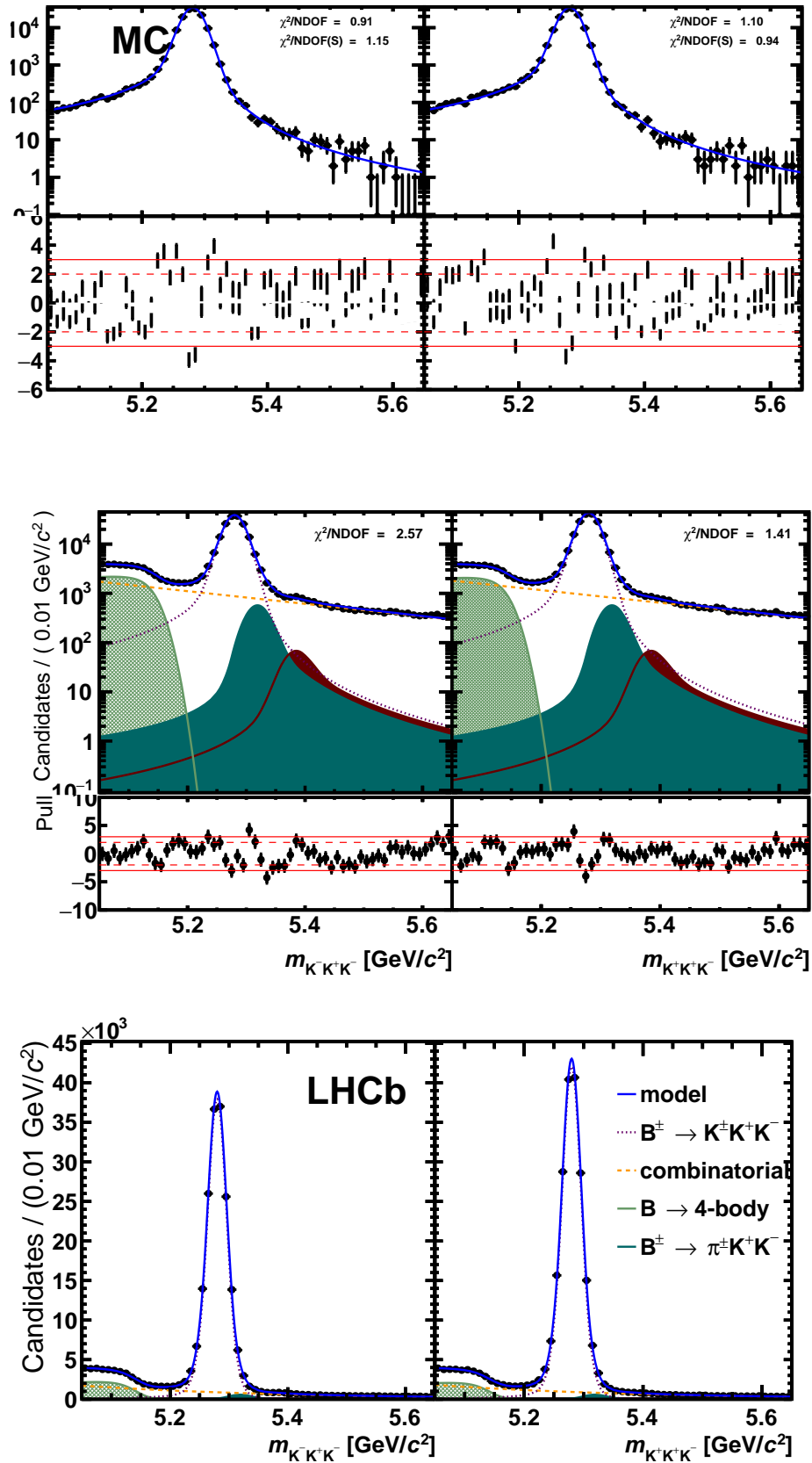


FIGURE A.6: Additional invariant-mass fit plots for  $B^\pm \rightarrow K^\pm K^+ K^-$ : (top) MC sample in logarithmic scale, with pull; (middle) data sample in logarithmic scale, with pull; (bottom) data sample plot.

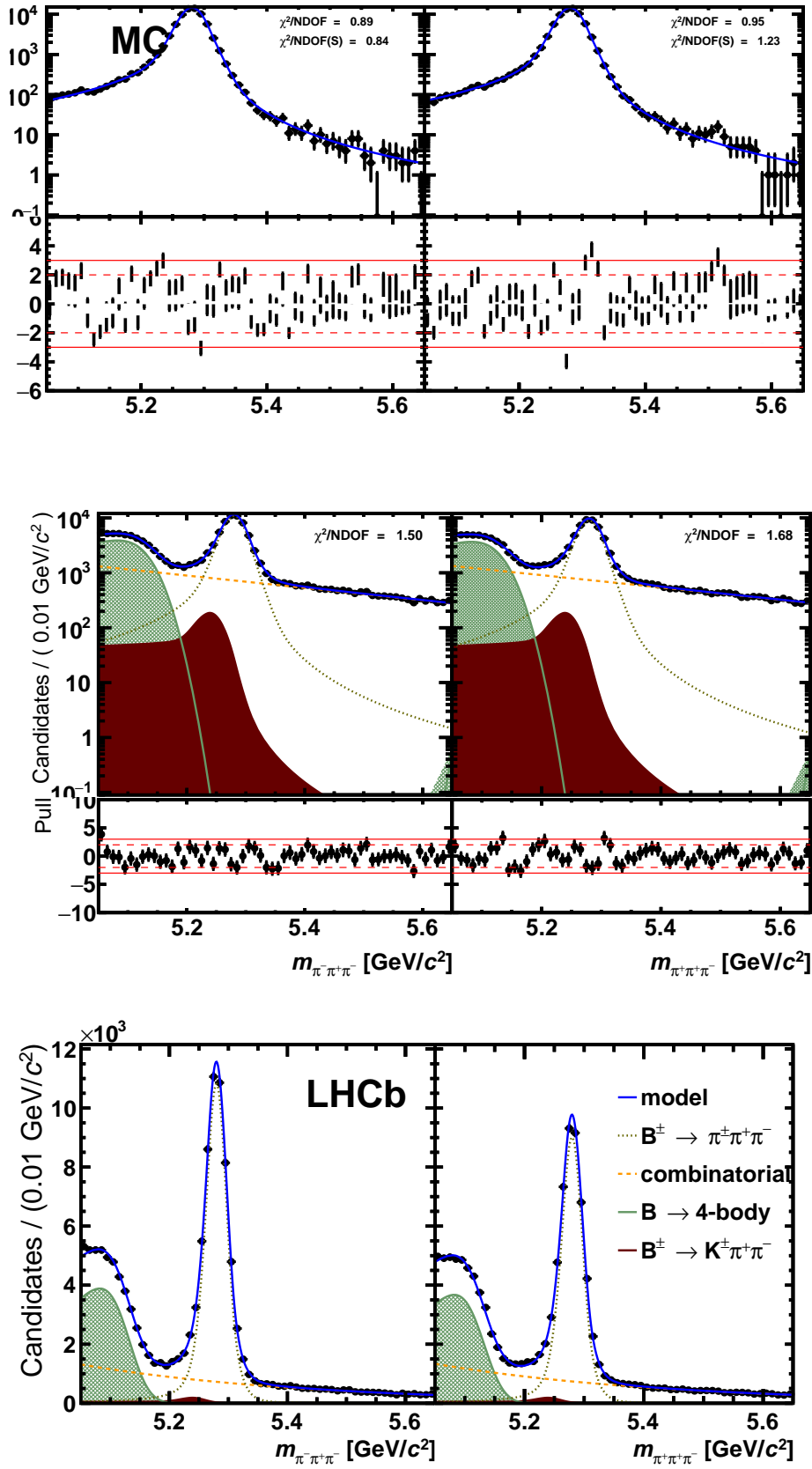


FIGURE A.7: Additional invariant-mass fit plots for  $B^\pm \rightarrow \pi^\pm\pi^+\pi^-$ : (top) MC sample in logarithmic scale, with pull; (middle) data sample in logarithmic scale, with pull; (bottom) data sample plot.

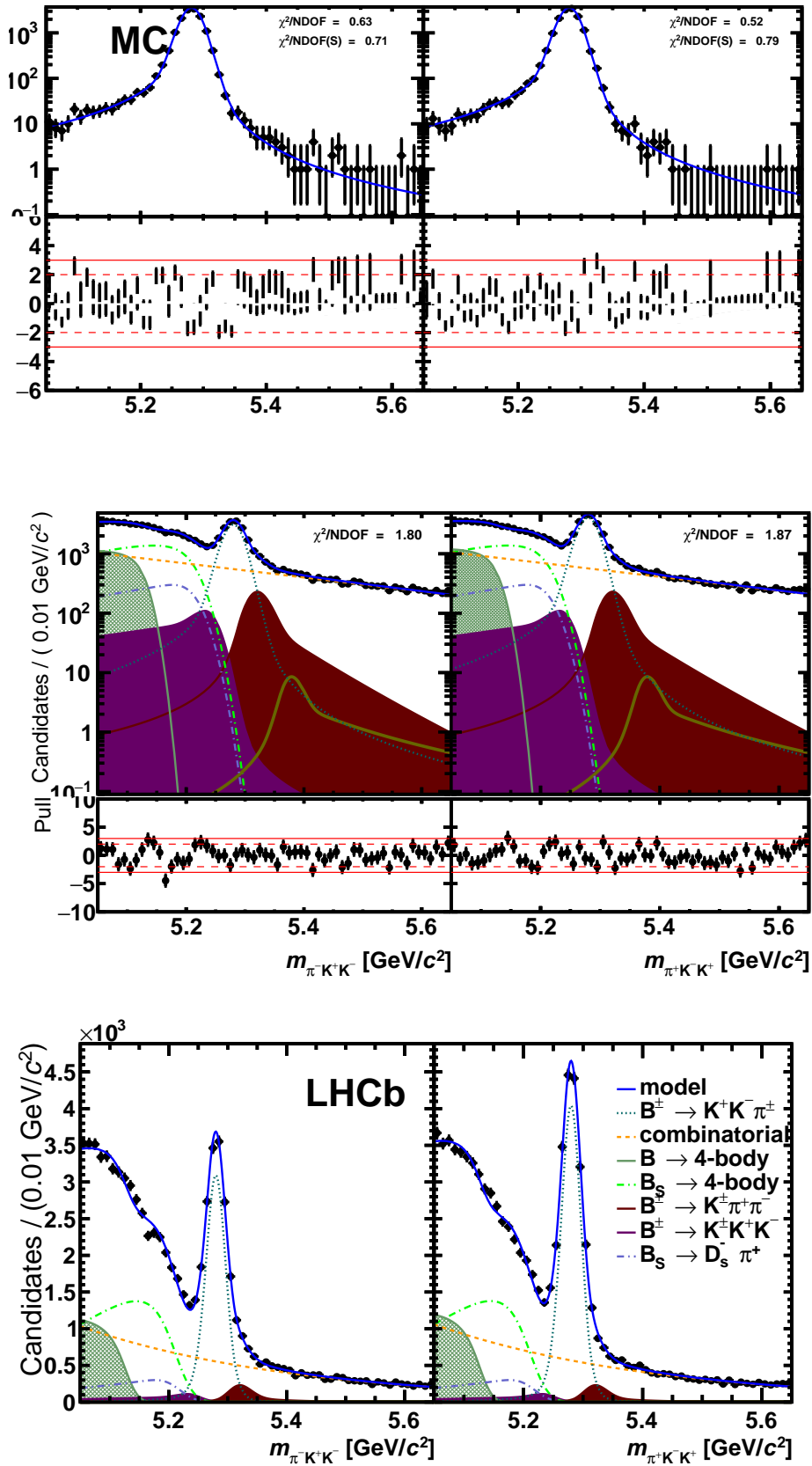
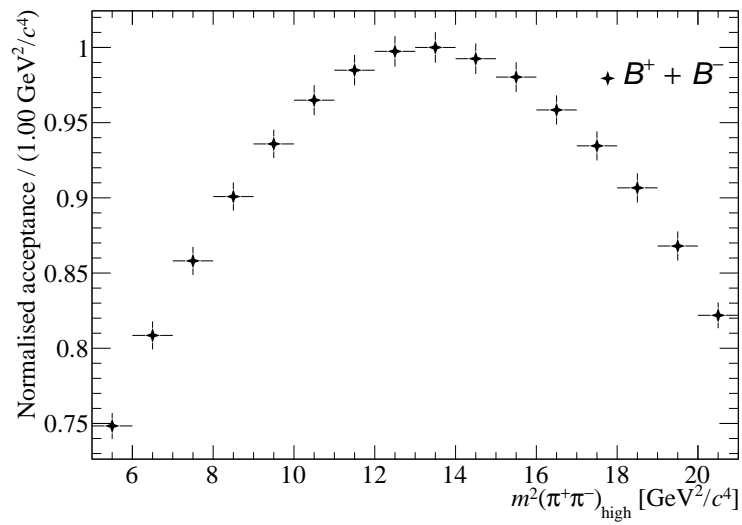


FIGURE A.8: Additional invariant-mass fit plots for  $B^\pm \rightarrow \pi^\pm K^+ K^-$ : (top) MC sample in logarithmic scale, with pull; (middle) data sample in logarithmic scale, with pull; (bottom) data sample plot.

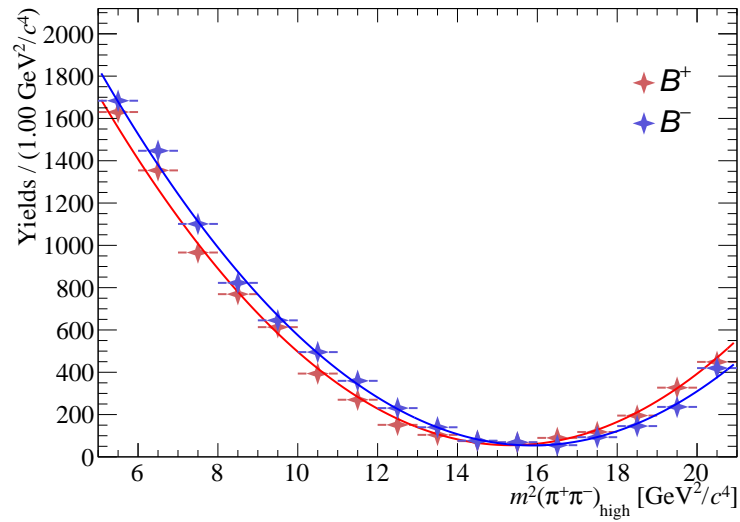
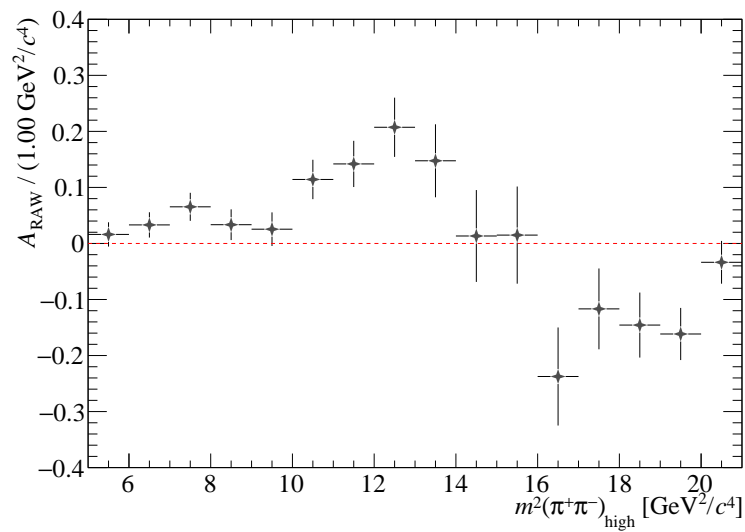
## Appendix B

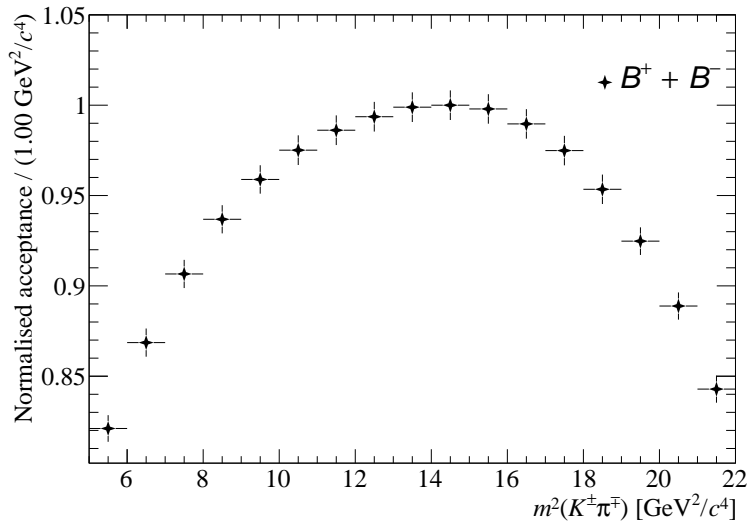
# Complementary $B \rightarrow PV$ Plots

This appendix serves as a complement to Section 5.3, which presents  $CP$ -asymmetry measurements in  $B \rightarrow PV$  decays via an model-independent method. For each vector resonance, Figures B.1–B.5 display the scaled acceptance distributions used to account for non-uniform signal efficiencies in the phase space, and the acceptance-corrected  $B^+$  and  $B^-$  projected distributions in  $s_{\perp}$  and subsequent  $A_{\text{RAW}}$  distribution.

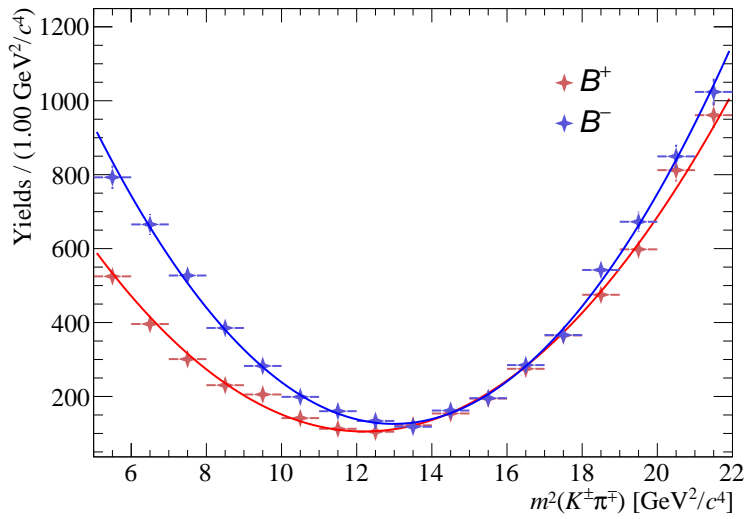
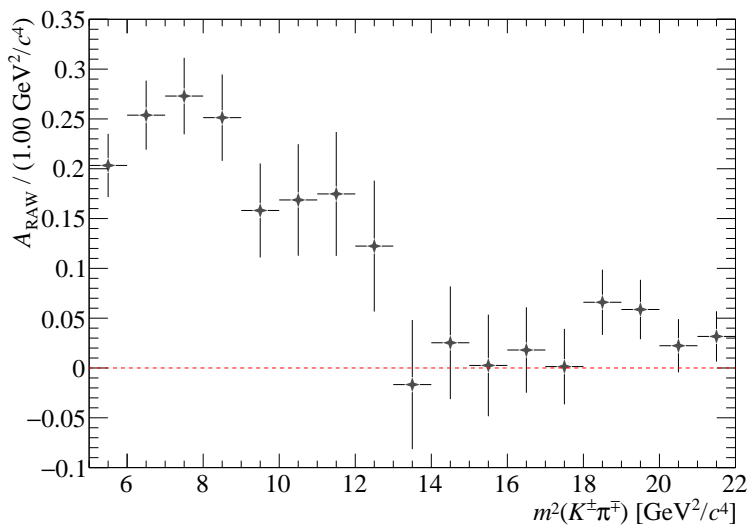


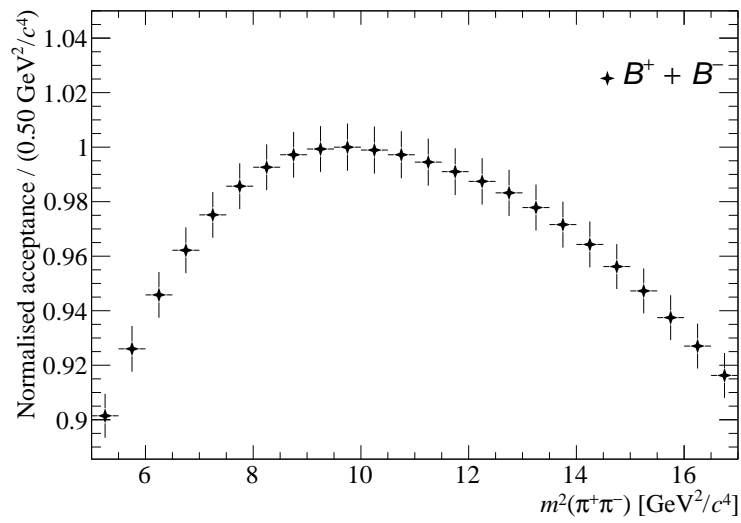
(a) Scaled acceptance distribution.

(b) Acceptance-corrected  $B^+$  and  $B^-$  yield distributions over  $s_{\perp}$ .(c) Acceptance-corrected  $A_{\text{RAW}}$  distribution.FIGURE B.1: Complementary plots for  $\rho(770)^0$  in  $B^{\pm} \rightarrow \pi^{\pm}\pi^+\pi^-$ .

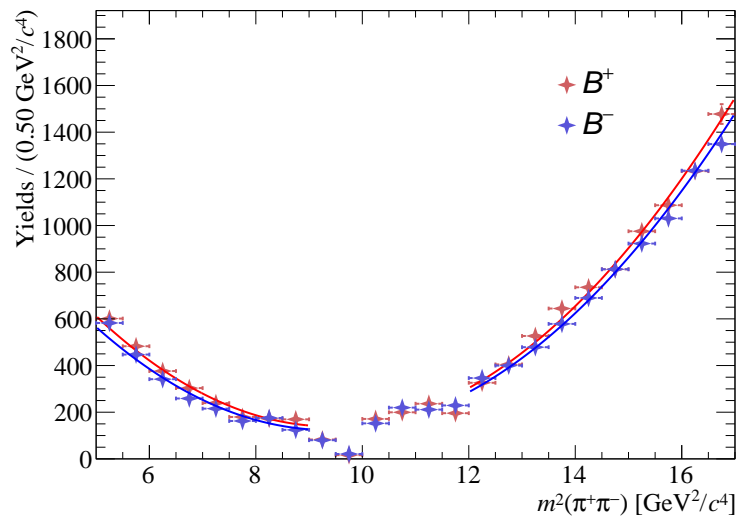
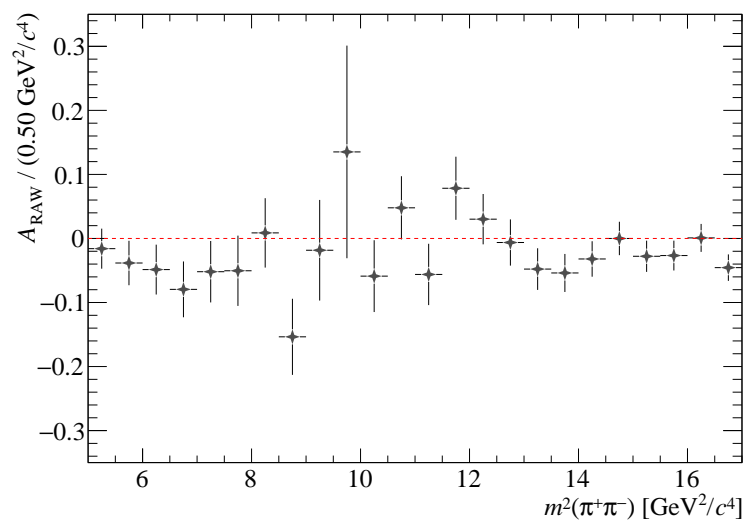


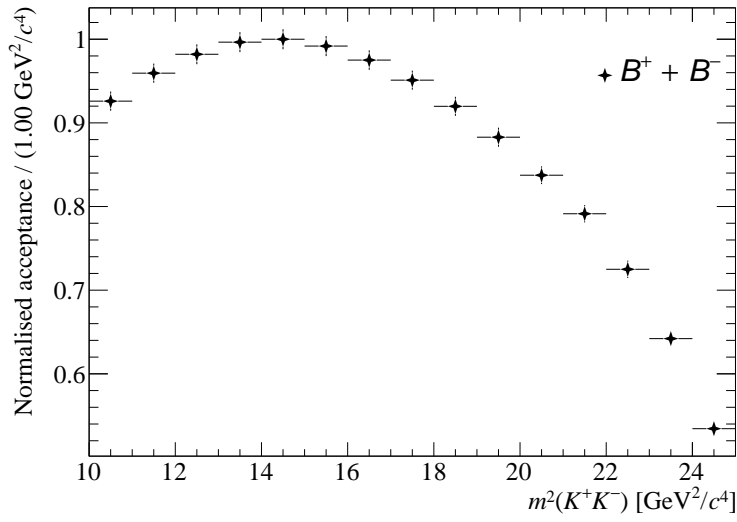
(a) Scaled acceptance distribution.

(b) Acceptance-corrected  $B^+$  and  $B^-$  yield distributions over  $s_{\perp}$ .(c) Acceptance-corrected  $A_{\text{RAW}}$  distribution.FIGURE B.2: Complementary plots for  $\rho(770)^0$  in  $B^{\pm} \rightarrow K^{\pm}\pi^+\pi^{-}$ .

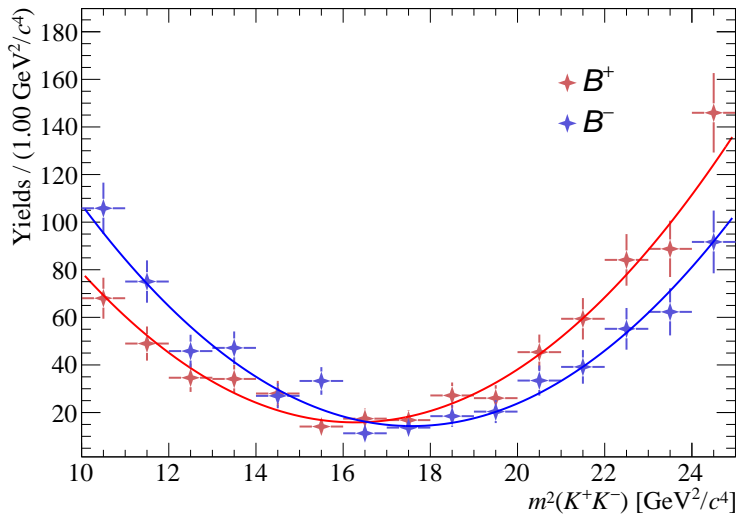
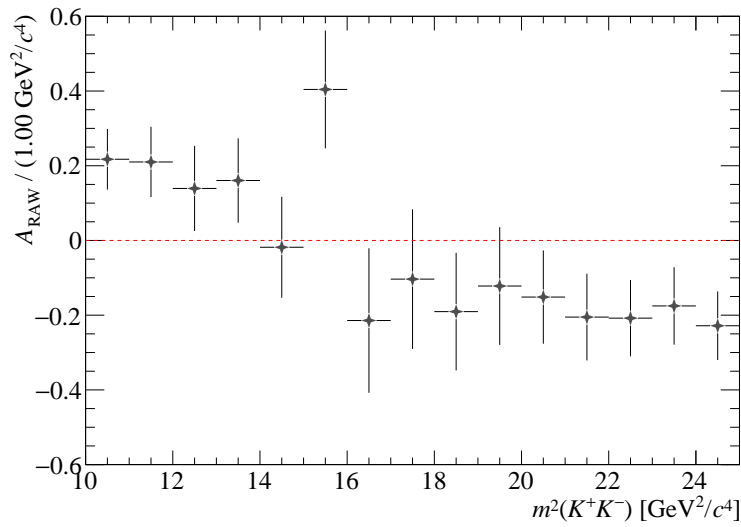


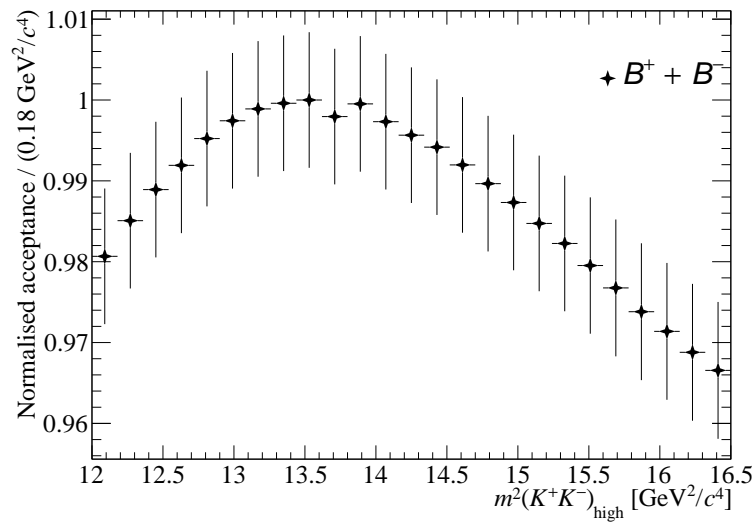
(a) Scaled acceptance distribution.

(b) Acceptance-corrected  $B^+$  and  $B^-$  yield distributions over  $s_{\perp}$ .(c) Acceptance-corrected  $A_{\text{RAW}}$  distribution.FIGURE B.3: Complementary plots for  $K^*(892)^0$  in  $B^{\pm} \rightarrow K^{\pm}\pi^+\pi^-$ .

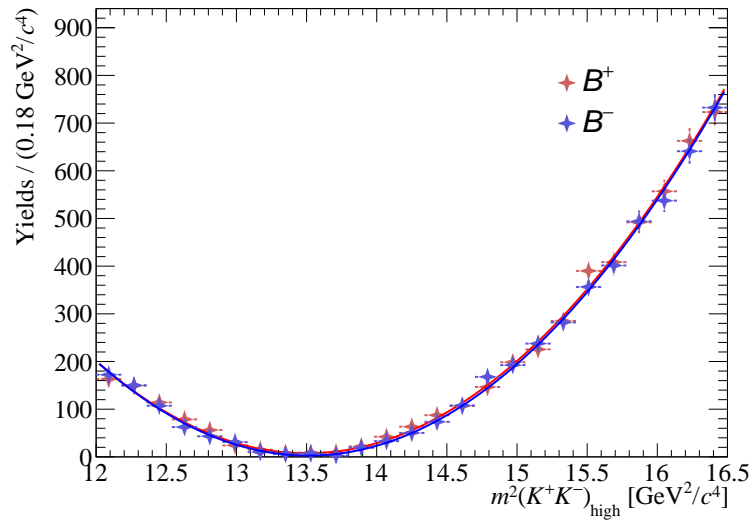
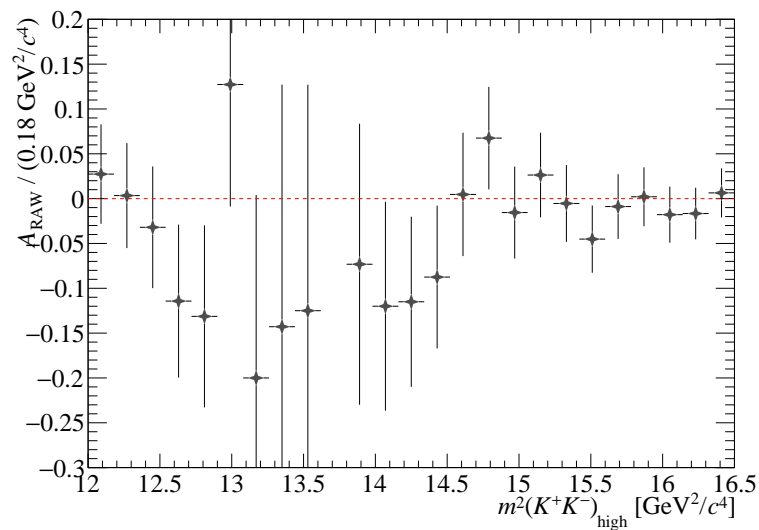


(a) Scaled acceptance distribution.

(b) Acceptance-corrected  $B^+$  and  $B^-$  yield distributions over  $s_{\perp}$ .(c) Acceptance-corrected  $A_{\text{RAW}}$  distribution.FIGURE B.4: Complementary plots for  $K^*(892)^0$  in  $B^{\pm} \rightarrow \pi^{\pm}K^+K^-$ .



(a) Scaled acceptance distribution.

(b) Acceptance-corrected  $B^+$  and  $B^-$  yield distributions over  $s_{\perp}$ .(c) Acceptance-corrected  $A_{\text{RAW}}$  distribution.FIGURE B.5: Complementary plots for  $\phi(1020)$  in  $B^{\pm} \rightarrow K^{\pm}K^+K^-$ .

# Bibliography

- [1] C. Sagan; *The Varieties of Scientific Experience: A Personal View of the Search for God*, (Penguin Books, 2007); ISBN 0143112627, 9780143112624.
- [2] A. G. van Melsen; “Atomism”; in *Encyclopaedia Britannica* (2016); (accessed: 2020-07-24); URL <https://www.britannica.com/topic/atomism>.
- [3] A. Chalmers; “Atomism from the 17th to the 20th Century”; in *The Stanford Encyclopedia of Philosophy* (edited by E. N. Zalta), (Metaphysics Research Lab, Stanford University, 2019); (accessed: 2020-07-24); URL <https://plato.stanford.edu/archives/spr2019/entries/atomism-modern/>.
- [4] J. J. Thomson; “Cathode Rays”; *The London, Edinburgh, and Dublin Philosophical Magazine and Journal of Science* **44** (1897), no. 269 pp. 293; doi:[10.1080/14786449708621070](https://doi.org/10.1080/14786449708621070).
- [5] E. Rutherford; “LXXIX. The scattering of  $\alpha$  and  $\beta$  particles by matter and the structure of the atom”; *The London, Edinburgh, and Dublin Philosophical Magazine and Journal of Science* **21** (1911), no. 125 pp. 669; doi:[10.1080/14786440508637080](https://doi.org/10.1080/14786440508637080).
- [6] A. Einstein; “Über die von der molekularkinetischen Theorie der Wärme geforderte Bewegung von in ruhenden Flüssigkeiten suspendierten Teilchen”; *Annalen der Physik* **322** (1905), no. 8 pp. 549; doi:[10.1002/andp.19053220806](https://doi.org/10.1002/andp.19053220806).
- [7] J. Perrin; “Mouvement brownien et réalité moléculaire”; *Ann. de Chimie et de Physique* **18** (1909) p. 5.
- [8] C. D. Anderson; “The Positive Electron”; *Phys. Rev.* **43** (1933) pp. 491; doi:[10.1103/PhysRev.43.491](https://doi.org/10.1103/PhysRev.43.491).
- [9] J. Chadwick; “Possible Existence of a Neutron”; *Nature* **129** (1932), no. 3252 p. 312; doi:[10.1038/129312a0](https://doi.org/10.1038/129312a0).
- [10] M. Gell-Mann; “A schematic model of baryons and mesons”; *Physics Letters* **8** (1964), no. 3 pp. 214 ; doi:[https://doi.org/10.1016/S0031-9163\(64\)92001-3](https://doi.org/10.1016/S0031-9163(64)92001-3).
- [11] G. Zweig; “An SU<sub>3</sub> model for strong interaction symmetry and its breaking”; *CERN Report* **8419** (1964).
- [12] E. D. Bloom *et al.*; “High-Energy Inelastic  $e - p$  Scattering at 6° and 10°”; *Phys. Rev. Lett.* **23** (1969) pp. 930; doi:[10.1103/PhysRevLett.23.930](https://doi.org/10.1103/PhysRevLett.23.930).
- [13] M. Breidenbach *et al.*; “Observed Behavior of Highly Inelastic Electron-Proton Scattering”; *Phys. Rev. Lett.* **23** (1969), no. 16 pp. 935; doi:[10.1103/PhysRevLett.23.935](https://doi.org/10.1103/PhysRevLett.23.935).
- [14] D. Hanneke, S. Fogwell and G. Gabrielse; “New Measurement of the Electron Magnetic Moment and the Fine Structure Constant”; *Phys. Rev. Lett.* **100** (2008) p. 120801; doi:[10.1103/PhysRevLett.100.120801](https://doi.org/10.1103/PhysRevLett.100.120801).

- [15] T. Aoyama, M. Hayakawa, T. Kinoshita and M. Nio; “Tenth-order electron anomalous magnetic moment: Contribution of diagrams without closed lepton loops”; *Phys. Rev. D* **91** (2015); doi:[10.1103/PhysRevD.91.033006](https://doi.org/10.1103/PhysRevD.91.033006).
- [16] G. Aad *et al.* (ATLAS collaboration); “Observation of a new particle in the search for the Standard Model Higgs boson with the ATLAS detector at the LHC”; *Physics Letters B* **716** (2012), no. 1 p. 1–29; doi:[10.1016/j.physletb.2012.08.020](https://doi.org/10.1016/j.physletb.2012.08.020); [1207.7214](https://arxiv.org/abs/1207.7214).
- [17] S. Chatrchyan *et al.* (CMS collaboration); “Observation of a new boson at a mass of 125 GeV with the CMS experiment at the LHC”; *Physics Letters B* **716** (2012), no. 1 p. 30–61; doi:[10.1016/j.physletb.2012.08.021](https://doi.org/10.1016/j.physletb.2012.08.021).
- [18] Planck collaboration; “Planck 2018 results. VI. Cosmological parameters”; (2018); URL <https://arxiv.org/abs/1807.06209>.
- [19] A. D. Sakharov; “Violation CP invariance, C asymmetry, and baryon asymmetry of the universe”; *Soviet Physics Uspekhi* **34** (1991), no. 5 pp. 392; doi:[10.1070/pu1991v034n05abeh002497](https://doi.org/10.1070/pu1991v034n05abeh002497).
- [20] L. Canetti, M. Drewes and M. Shaposhnikov; “Matter and antimatter in the universe”; *New Journal of Physics* **14** (2012), no. 9 p. 095012; doi:[10.1088/1367-2630/14/9/095012](https://doi.org/10.1088/1367-2630/14/9/095012).
- [21] R. Aaij *et al.* (LHCb collaboration); “Measurements of CP violation in the three-body phase space of charmless B decays”; *Phys. Rev. D* **90** (2014) p. 112004; doi:[10.1103/PhysRevD.90.112004](https://doi.org/10.1103/PhysRevD.90.112004).
- [22] R. Aaij *et al.* (LHCb collaboration); “Amplitude Analysis of  $B^\pm \rightarrow \pi^\pm K^+ K^-$  Decays”; *Phys. Rev. Lett.* **123** (2019) p. 231802; doi:[10.1103/PhysRevLett.123.231802](https://doi.org/10.1103/PhysRevLett.123.231802).
- [23] R. Aaij *et al.* (LHCb collaboration); “Amplitude analysis of the  $B^+ \rightarrow \pi^+ \pi^+ \pi^-$  decay”; *Phys. Rev. D* **101** (2020) p. 012006; doi:[10.1103/PhysRevD.101.012006](https://doi.org/10.1103/PhysRevD.101.012006).
- [24] I. Bediaga and C. Göbel; “Direct CP violation in beauty and charm hadron decays”; *Progress in Particle and Nuclear Physics* **114** (2020) p. 103808; doi:<https://doi.org/10.1016/j.pnpnp.2020.103808>.
- [25] D. Galbraith and C. Burgard; “Diagram of the Standard Model of particle physics”; URL <https://texample.net/tikz/examples/model-physics/>.
- [26] R. Aaij *et al.* (LHCb Collaboration); “Observation of the Resonant Character of the  $Z(4430)^-$  State”; *Phys. Rev. Lett.* **112** (2014) p. 222002; doi:[10.1103/PhysRevLett.112.222002](https://doi.org/10.1103/PhysRevLett.112.222002).
- [27] R. Aaij *et al.* (LHCb Collaboration); “Observation of  $J/\psi p$  Resonances Consistent with Pentaquark States in  $\Lambda_b^0 \rightarrow J/\psi K^- p$  Decays”; *Phys. Rev. Lett.* **115** (2015) p. 072001; doi:[10.1103/PhysRevLett.115.072001](https://doi.org/10.1103/PhysRevLett.115.072001).
- [28] S. L. Glashow; “Partial-symmetries of weak interactions”; *Nuclear Physics* **22** (1961), no. 4 pp. 579 ; doi:[https://doi.org/10.1016/0029-5582\(61\)90469-2](https://doi.org/10.1016/0029-5582(61)90469-2).
- [29] S. Weinberg; “A Model of Leptons”; *Phys. Rev. Lett.* **19** (1967) pp. 1264; doi:[10.1103/PhysRevLett.19.1264](https://doi.org/10.1103/PhysRevLett.19.1264).

- [30] A. Salam; “Weak and Electromagnetic Interactions”; *Conf. Proc. C* **680519** (1968) pp. 367; doi:[10.1142/9789812795915\\_0034](https://doi.org/10.1142/9789812795915_0034).
- [31] F. Englert and R. Brout; “Broken Symmetry and the Mass of Gauge Vector Mesons”; *Phys. Rev. Lett.* **13** (1964) pp. 321; doi:[10.1103/PhysRevLett.13.321](https://doi.org/10.1103/PhysRevLett.13.321).
- [32] P. W. Higgs; “Broken Symmetries and the Masses of Gauge Bosons”; *Phys. Rev. Lett.* **13** (1964) pp. 508; doi:[10.1103/PhysRevLett.13.508](https://doi.org/10.1103/PhysRevLett.13.508).
- [33] G. S. Guralnik, C. R. Hagen and T. W. B. Kibble; “Global Conservation Laws and Massless Particles”; *Phys. Rev. Lett.* **13** (1964) pp. 585; doi:[10.1103/PhysRevLett.13.585](https://doi.org/10.1103/PhysRevLett.13.585).
- [34] E. Noether; “Invariante Variationsprobleme”; *Nachrichten von der Gesellschaft der Wissenschaften zu Göttingen, Mathematisch-Physikalische Klasse* **1918** (1918) pp. 235; URL <http://eudml.org/doc/59024>.
- [35] T. D. Lee and C. N. Yang; “Question of Parity Conservation in Weak Interactions”; *Phys. Rev.* **104** (1956) pp. 254; doi:[10.1103/PhysRev.104.254](https://doi.org/10.1103/PhysRev.104.254).
- [36] C. S. Wu, E. Ambler, R. W. Hayward, D. D. Hoppes and R. P. Hudson; “Experimental Test of Parity Conservation in Beta Decay”; *Phys. Rev.* **105** (1957) pp. 1413; doi:[10.1103/PhysRev.105.1413](https://doi.org/10.1103/PhysRev.105.1413).
- [37] J. H. Christenson, J. W. Cronin, V. L. Fitch and R. Turlay; “Evidence for the  $2\pi$  Decay of the  $K_2^0$  Meson”; *Phys. Rev. Lett.* **13** (1964) pp. 138; doi:[10.1103/PhysRevLett.13.138](https://doi.org/10.1103/PhysRevLett.13.138).
- [38] B. Aubert *et al.* (BaBar Collaboration); “Observation of  $CP$  Violation in the  $B^0$  Meson System”; *Phys. Rev. Lett.* **87** (2001) p. 091801; doi:[10.1103/PhysRevLett.87.091801](https://doi.org/10.1103/PhysRevLett.87.091801).
- [39] K. Abe *et al.* (Belle Collaboration); “Observation of Large  $CP$  Violation in the Neutral  $B$  Meson System”; *Phys. Rev. Lett.* **87** (2001) p. 091802; doi:[10.1103/PhysRevLett.87.091802](https://doi.org/10.1103/PhysRevLett.87.091802).
- [40] M. Tanabashi *et al.* (Particle Data Group); “Review of Particle Physics”; *Phys. Rev. D* **98** (2018) p. 030001; doi:[10.1103/PhysRevD.98.030001](https://doi.org/10.1103/PhysRevD.98.030001).
- [41] Y. Amhis *et al.*; “Averages of  $b$ -hadron,  $c$ -hadron, and  $\tau$ -lepton properties as of summer 2016”; *The European Physical Journal C* **77** (2017), no. 12; doi:[10.1140/epjc/s10052-017-5058-4](https://doi.org/10.1140/epjc/s10052-017-5058-4).
- [42] G. Durieux and Y. Grossman; “ $CP$  violation: Another piece of the puzzle”; *Nature Physics* **13** (2017), no. 4 p. 322; doi:[10.1038/nphys4068](https://doi.org/10.1038/nphys4068).
- [43] R. Aaij *et al.* (LHCb Collaboration); “Observation of  $CP$  Violation in Charm Decays”; *Phys. Rev. Lett.* **122** (2019) p. 211803; doi:[10.1103/PhysRevLett.122.211803](https://doi.org/10.1103/PhysRevLett.122.211803).
- [44] M. Kobayashi and T. Maskawa; “ $CP$ -Violation in the Renormalizable Theory of Weak Interaction”; *Progress of Theoretical Physics* **49** (1973), no. 2 pp. 652; doi:[10.1143/PTP.49.652](https://doi.org/10.1143/PTP.49.652).
- [45] N. Cabibbo; “Unitary Symmetry and Leptonic Decays”; *Phys. Rev. Lett.* **10** (1963) pp. 531; doi:[10.1103/PhysRevLett.10.531](https://doi.org/10.1103/PhysRevLett.10.531).

- [46] L. Wolfenstein; "Parametrization of the Kobayashi-Maskawa Matrix"; *Phys. Rev. Lett.* **51** (1983) pp. 1945; doi:[10.1103/PhysRevLett.51.1945](https://doi.org/10.1103/PhysRevLett.51.1945).
- [47] H. B. Dijkstra; "CP violation prospects at the LHC"; *Brazilian Journal of Physics* **34** (2004) pp. 1295; doi:[10.1590/S0103-97332004000700004](https://doi.org/10.1590/S0103-97332004000700004).
- [48] R. Dalitz; "CXII. On the analysis of  $\tau$ -meson data and the nature of the  $\tau$ -meson"; *The London, Edinburgh, and Dublin Philosophical Magazine and Journal of Science* **44** (1953), no. 357 pp. 1068; doi:[10.1080/14786441008520365](https://doi.org/10.1080/14786441008520365).
- [49] J. Back *et al.*; "LAURA<sup>++</sup>: A Dalitz plot fitter"; *Computer Physics Communications* **231** (2018) p. 198–242; doi:[10.1016/j.cpc.2018.04.017](https://doi.org/10.1016/j.cpc.2018.04.017).
- [50] A. B. R. Cavalcante; *CP violation studies in three-body charmless  $B^\pm$  decays and contribution to the LHCb SciFi Tracker*; Ph.D. thesis; CBPF; Rio de Janeiro, Brazil (2017).
- [51] M. Bander, D. Silverman and A. Soni; "CP Noninvariance in the Decays of Heavy Charged Quark Systems"; *Phys. Rev. Lett.* **43** (1979) pp. 242; doi:[10.1103/PhysRevLett.43.242](https://doi.org/10.1103/PhysRevLett.43.242).
- [52] M. Wirbel, B. Stech and M. Bauer; "Exclusive Semileptonic Decays of Heavy Mesons"; *Z. Phys. C* **29** (1985) p. 637; doi:[10.1007/BF01560299](https://doi.org/10.1007/BF01560299).
- [53] G. P. Lepage and S. J. Brodsky; "Exclusive processes in perturbative quantum chromodynamics"; *Phys. Rev. D* **22** (1980) pp. 2157; doi:[10.1103/PhysRevD.22.2157](https://doi.org/10.1103/PhysRevD.22.2157).
- [54] M. Beneke, G. Buchalla, M. Neubert and C. T. Sachrajda; "QCD Factorization for  $B \rightarrow \pi\pi$  Decays: Strong Phases and CP Violation in the Heavy-Quark Limit"; *Physical Review Letters* **83** (1999), no. 10 p. 1914–1917; doi:[10.1103/physrevlett.83.1914](https://doi.org/10.1103/physrevlett.83.1914).
- [55] Y.-Y. Keum, H.-n. Li and A. I. Sanda; "Penguin enhancement and  $B \rightarrow K\pi$  decays in perturbative QCD"; *Phys. Rev. D* **63** (2001) p. 054008; doi:[10.1103/PhysRevD.63.054008](https://doi.org/10.1103/PhysRevD.63.054008).
- [56] C. W. Bauer, S. Fleming and M. Luke; "Summing Sudakov logarithms in  $B \rightarrow X_s \gamma$  in effective field theory"; *Phys. Rev. D* **63** (2000) p. 014006; doi:[10.1103/PhysRevD.63.014006](https://doi.org/10.1103/PhysRevD.63.014006).
- [57] I. I. Bigi; "'Could charm (&  $\tau$ ) transitions be the "poor princess" providing a deeper understanding of fundamental dynamics?" or: "Finding novel forces""; *Frontiers of Physics* **10** (2015), no. 3 101203 (pages 0); doi:[10.1007/s11467-015-0476-y](https://doi.org/10.1007/s11467-015-0476-y).
- [58] I. Bediaga, T. Frederico and O. Lourenço; "CP violation and CPT invariance in  $B^\pm$  decays with final state interactions"; *Phys. Rev. D* **89** (2014), no. 9 p. 094013; doi:[10.1103/PhysRevD.89.094013](https://doi.org/10.1103/PhysRevD.89.094013); [1307.8164](https://arxiv.org/abs/1307.8164).
- [59] J. A. Nogueira, I. Bediaga, A. Cavalcante, T. Frederico and O. Lourenço; "CP violation: Dalitz interference, CPT, and FSI"; *Physical Review D* **92** (2015), no. 5; doi:[10.1103/physrevd.92.054010](https://doi.org/10.1103/physrevd.92.054010).
- [60] H.-Y. Cheng, C.-W. Chiang and A.-L. Kuo; "Updating  $B \rightarrow PP, VP$  decays in the framework of flavor symmetry"; *Phys. Rev. D* **91** (2015), no. 1 p. 014011; doi:[10.1103/PhysRevD.91.014011](https://doi.org/10.1103/PhysRevD.91.014011); [1409.5026](https://arxiv.org/abs/1409.5026).

- [61] R. Aaij *et al.* (LHCb Collaboration); “Measurement of  $CP$  Violation in the Phase Space of  $B^\pm \rightarrow K^\pm \pi^+ \pi^-$  and  $B^\pm \rightarrow K^\pm K^+ K^-$  Decays”; *Phys. Rev. Lett.* **111** (2013) p. 101801; doi:[10.1103/PhysRevLett.111.101801](https://doi.org/10.1103/PhysRevLett.111.101801).
- [62] e. a. Aaij, R. (LHCb Collaboration); “Measurement of  $CP$  Violation in the Phase Space of  $B^\pm \rightarrow K^+ K^- \pi^\pm$  and  $B^\pm \rightarrow \pi^+ \pi^- \pi^\pm$  Decays”; *Phys. Rev. Lett.* **112** (2014) p. 011801; doi:[10.1103/PhysRevLett.112.011801](https://doi.org/10.1103/PhysRevLett.112.011801).
- [63] R. Fleischer; *B Physics and CP Violation*; pp. 42–77 (2004); doi:[10.1007/978-3-540-40975-5\\_2](https://doi.org/10.1007/978-3-540-40975-5_2).
- [64] I. Bediaga *et al.*; “Second Generation of ‘Miranda Procedure’ for  $CP$  Violation in Dalitz Studies of B (and D and  $\tau$ ) Decays”; *Phys. Rev. D* **86** (2012) p. 036005; doi:[10.1103/PhysRevD.86.036005](https://doi.org/10.1103/PhysRevD.86.036005).
- [65] L. Evans and P. Bryant; “LHC Machine”; *Journal of Instrumentation* **3** (2008), no. 08 pp. S08001; doi:[10.1088/1748-0221/3/08/s08001](https://doi.org/10.1088/1748-0221/3/08/s08001).
- [66] A. A. Alves *et al.* (LHCb Collaboration); “The LHCb Detector at the LHC”; *Journal of Instrumentation* **3** (2008), no. 08 pp. S08005; doi:[10.1088/1748-0221/3/08/s08005](https://doi.org/10.1088/1748-0221/3/08/s08005).
- [67] R. Aaij *et al.* (LHCb Collaboration); “LHCb detector performance”; *International Journal of Modern Physics A* **30** (2015), no. 07 p. 1530022; doi:[10.1142/s0217751x15300227](https://doi.org/10.1142/s0217751x15300227).
- [68] CERN; “Our history”; (accessed: 2020-06-30); URL <https://home.cern/about/who-we-are/our-history>.
- [69] CERN; “Convention for the Establishment of a European Organization for Nuclear Research”; (accessed: 2020-06-30); URL <https://council.web.cern.ch/en/convention>.
- [70] E. Mobs; “The CERN accelerator complex. Complexe des accélérateurs du CERN”; (2016); General Photo; URL <https://cds.cern.ch/record/2197559>.
- [71] X. C. Vidal and R. Cid; “Luminosity: Taking a closer look at LHC”; (accessed: 2020-08-06); URL [http://lhc-closer.es/taking\\_a\\_closer\\_look\\_at\\_lhc/0.luminosity](http://lhc-closer.es/taking_a_closer_look_at_lhc/0.luminosity).
- [72] I. Bediaga *et al.* (LHCb collaboration); “Framework TDR for the LHCb Upgrade: Technical Design Report”; Tech. Rep. CERN-LHCC-2012-007. LHCb-TDR-12 (2012); URL <https://cds.cern.ch/record/1443882>.
- [73] “LHCb - Large Hadron Collider beauty experiment”; (accessed: 2020-08-06); URL <http://lhcb-public.web.cern.ch/>.
- [74] B. Aubert *et al.* (BaBar); “The BaBar detector”; *Nucl. Instrum. Meth. A* **479** (2002) pp. 1; doi:[10.1016/S0168-9002\(01\)02012-5](https://doi.org/10.1016/S0168-9002(01)02012-5).
- [75] A. Abashian *et al.*; “The Belle Detector”; *Nucl. Instrum. Meth. A* **479** (2002) pp. 117; doi:[10.1016/S0168-9002\(01\)02013-7](https://doi.org/10.1016/S0168-9002(01)02013-7).
- [76] C. Elsässer (LHCb collaboration); “ $\bar{b}b$  production angle plots”; (accessed: 2020-08-05); URL [https://lhcb.web.cern.ch/lhcb/speakersbureau/html/bb\\_ProductionAngles.html](https://lhcb.web.cern.ch/lhcb/speakersbureau/html/bb_ProductionAngles.html).

- [77] C. A. Beteta *et al.* (LHCb collaboration); “Monitoring radiation damage in the LHCb Tracker Turicensis”; (2018); URL <https://arxiv.org/abs/1809.05063>.
- [78] R. Arink *et al.* (LHCb Collaboration); “Performance of the LHCb Outer Tracker”; *Journal of Instrumentation* **9** (2013); doi:10.1088/1748-0221/9/01/P01002.
- [79] A. Zangwill; *Modern electrodynamics*, (Cambridge University Press, 2013).
- [80] A. Papanestis and C. D’Ambrosio; “Performance of the LHCb RICH detectors during the LHC Run II”; *Nuclear Instruments and Methods in Physics Research Section A: Accelerators, Spectrometers, Detectors and Associated Equipment* **876** (2017) p. 221–224; doi:10.1016/j.nima.2017.03.009.
- [81] A. A. Alves *et al.*; “Performance of the LHCb muon system”; *Journal of Instrumentation* **8** (2013), no. 02 pp. P02022; doi:10.1088/1748-0221/8/02/p02022.
- [82] LHCb; “Trigger Schemes”; (accessed: 2020-08-07); URL <http://lhcb.web.cern.ch/lhcb/speakersbureau/html/TriggerScheme.html>.
- [83] A. Hoecker *et al.*; “TMVA - Toolkit for Multivariate Data Analysis”; (2007); URL <https://arxiv.org/abs/physics/0703039>.
- [84] R. Aaij *et al.* (LHCb collaboration); “Measurement of  $B^0$ ,  $B_s^0$ ,  $B^+$  and  $\Lambda_b^0$  production asymmetries in 7 and 8 TeV proton-proton collisions”; *Phys. Lett.* **B774** (2017) p. 139; doi:10.1016/j.physletb.2017.09.023; 1703.08464.
- [85] M. Vesterinen and D. Mueller; “Measurement of the Kaon Detection Asymmetry using Double-tagged Partially Reconstructed  $D^0$  Decays”; Tech. Rep. LHCb-INT-2013-054. CERN-LHCb-INT-2013-054; CERN; Geneva (2013); URL <https://cds.cern.ch/record/1620824>.
- [86] R. Aaij *et al.*; “Measurement of the  $D_s^+ - D_s^-$  production asymmetry in 7 TeV  $pp$  collisions”; *Physics Letters B* **713** (2012), no. 3 p. 186–195; doi:10.1016/j.physletb.2012.06.001.
- [87] W. Verkerke and D. Kirkby; “The RooFit toolkit for data modeling”; (2003); [physics/0306116](https://arxiv.org/abs/physics/0306116).
- [88] T. Skwarnicki; *A study of the radiative CASCADE transitions between the Upsilon-Prime and Upsilon resonances*; Ph.D. thesis; Cracow, INP (1986).
- [89] H. Albrecht *et al.* (ARGUS collaboration); “Search for hadronic  $b \rightarrow u$  decays”; *Physics Letters B* **241** (1990), no. 2 pp. 278 ; doi:[https://doi.org/10.1016/0370-2693\(90\)91293-K](https://doi.org/10.1016/0370-2693(90)91293-K).
- [90] L. Anderlini *et al.*; “The PIDCalib package”; Tech. Rep. LHCb-PUB-2016-021. CERN-LHCb-PUB-2016-021; CERN; Geneva (2016); URL <https://cds.cern.ch/record/2202412>.
- [91] A. Davis, L. Dufour, F. Ferrari, S. Stahl, M. A. Vesterinen and J. Van Tilburg; “Measurement of the  $K^- \pi^+$  two-track detection asymmetry in Run 2 using the Turbo stream”; Tech. Rep. LHCb-INT-2017-023. CERN-LHCb-INT-2017-023; CERN; Geneva (2017); URL <https://cds.cern.ch/record/2284097>.

- [92] A. Carbone, F. Ferrari, S. Perazzini and V. Vagnoni; “Measurement of  $B^0$ ,  $B_s^0$ ,  $B^+$  and  $\Lambda_b^0$  production asymmetries in 7 TeV and 8 TeV  $pp$  collisions”; (2016); URL <https://cds.cern.ch/record/2156564>.
- [93] D. C. Craik, T. Gershon, T. Latham and M. Whitehead; “Dalitz plot analysis of  $B_s^0 \rightarrow \bar{D}^0 K^- \pi^+$ ”; (2013); URL <https://cds.cern.ch/record/1508058>.
- [94] M. Pivk and F. Le Diberder; “sPlot: A statistical tool to unfold data distributions”; *Nuclear Instruments and Methods in Physics Research Section A: Accelerators, Spectrometers, Detectors and Associated Equipment* **555** (2005), no. 1-2 p. 356–369; doi:[10.1016/j.nima.2005.08.106](https://doi.org/10.1016/j.nima.2005.08.106).
- [95] J. H. Alvarenga Nogueira, I. Bediaga, T. Frederico, P. Magalhães and J. Molina Rodriguez; “Suppressed  $B \rightarrow PV$  CP asymmetry: CPT constraint”; *Phys. Rev. D* **94** (2016), no. 5 p. 054028; doi:[10.1103/PhysRevD.94.054028](https://doi.org/10.1103/PhysRevD.94.054028).
- [96] Byckling and Kajantie; *Particle Kinematics*, (John Wiley & Sons 1972); ISBN 0 471 128.
- [97] B. Aubert *et al.* (BaBar); “Dalitz Plot Analysis of  $B^\pm \rightarrow \pi^\pm \pi^+ \pi^-$  Decays”; *Phys. Rev. D* **79** (2009) p. 072006; doi:[10.1103/PhysRevD.79.072006](https://doi.org/10.1103/PhysRevD.79.072006); [0902.2051](https://arxiv.org/abs/0902.2051).
- [98] R. Aaij *et al.* (LHCb collaboration); “Observation of Several Sources of CP Violation in  $B^+ \rightarrow \pi^+ \pi^+ \pi^-$  Decays”; *Phys. Rev. Lett.* **124** (2020) p. 031801; doi:[10.1103/PhysRevLett.124.031801](https://doi.org/10.1103/PhysRevLett.124.031801).
- [99] B. Aubert *et al.*; “Evidence for direct CP violation from Dalitz-plot analysis of  $B^\pm \rightarrow K^\pm \pi^\mp \pi^\pm$ ”; *Physical Review D* **78** (2008), no. 1; doi:[10.1103/physrevd.78.012004](https://doi.org/10.1103/physrevd.78.012004).
- [100] J. P. Lees *et al.* (BaBar Collaboration); “Study of CP violation in Dalitz-plot analyses of  $B^0 \rightarrow K^+ K^- K_S^0$ ,  $B^+ \rightarrow K^+ K^- K^+$ , and  $B^+ \rightarrow K_S^0 K_S^0 K^+$ ”; *Phys. Rev. D* **85** (2012) p. 112010; doi:[10.1103/PhysRevD.85.112010](https://doi.org/10.1103/PhysRevD.85.112010).